THE UNIVERSITY OF MANITOBA

TRANSPORT MEASUREMENTS ON SOME DILUTE ALLOYS: PdCo AND RuMn

by

M. E. COLP

A THESIS

SUBMITTED TO THE FACULTY OF GRADUATE STUDIES

IN PARTIAL FULFILLMENT OF THE REQUIREMENTS OF THE DEGREE

OF MASTER OF SCIENCE

DEPARTMENT OF PHYSICS

WINNIPEG, MANITOBA

October 1972

ABSTRACT

An apparatus has been constructed to measure the electrical resistivity of metallic samples over a temperature range from 1.4K to 300K. The apparatus was used to measure the resistivity of a set of five PdCo alloys ranging in concentration between 2 to 7.5 at.% Co over temperatures in the interval 1.4-77K. Well below the ordering temperature, T_c, the incremental resistivity can be described by $\Delta\rho(T) = A + BT^2$ where A and B are concentration dependent parameters. Based on an "s-d" model, a theoretical expression for $\Delta\rho(T)$ of similar form was derived, allowing specific evaluation of the "potential" scattering integral $|V|$ for the alloy system to be made. Further, using estimates of the s electron-local moment exchange coupling $|J_{s\text{-}local}|$, the "giant-moment" spin S, and the Fermi wavevector k_F from the literature, values of the acoustic spin-wave stiffness D were determined. D was found to increase linearly with concentration for PdCo alloys in this concentration range. The electrical resistivity of two dilute RuMn alloys was also investigated, in the temperature range 1.45 - 130K. No temperature dependence was observed below about 30K. The small anomalous resistivity observed above 30K was explained on the basis of s electron-localized spin fluctuation scattering and has the form $\rho_{mag}(T) \propto cT^2$. Estimates were made of the lsf characteristic temperature, T_s.

ACKNOWLEDGEMENTS

The author is indebted to Dr. Gwyn Williams for his supervision of the research project and the thesis, and for numerous helpful discussions throughout the course of the work.

Mr. R. Gregory's technical advice during the construction of the apparatus is much appreciated, and thanks are due to Miss Sharon Drier for the excellent job she has done in typing the manuscript.

TABLE OF CONTENTS

CHAPTER ONE

INTRODUCTION

I.1 Historical Sketch

In the past ten or so years a great deal of attention has been directed at the dilute alloy problem. Many combinations of host and impurity atoms have been examined over various ranges of temperature, impurity concentration and applied magnetic field. Historically the subject gained significant momentum with the discovery of resistance minima in "pure" noble metals at low temperatures[1]. The minima were later attributed to very small concentrations of magnetic impurity atoms such as Fe and Mn. These atoms carry a magnetic moment and give a Curie-Weiss law contribution to susceptibility. They account, too, for an observed logarithmic increase in resistivity with decreasing temperature above the Kondo temperature[2,3].

Besides the experimental work, a great deal of theoretical research has been done on the subject of dilute alloys with the result that a number of useful models have been developed. Each model is applicable under a certain set of conditions and can be used to predict the behaviour of various systems of alloys. The models are often equally useful for "predicting" the magnetic character of a system when used in retrospect guided by experimental data.

In order to provide some background, it is constructive to contrast the situation found in an extrinsic semiconductor to that found in a dilute magnetic alloy. Both are examples of dilute alloys, but the characteristics of the two systems are very different. In extrinsic semiconductors, the host (for example Si) has a completely filled valence band, but has a conduction band containing no electrons. At non-zero temperatures some electrons may be thermally raised to the conduction band, but the band gap is wide and this contribution

to conductivity is very small. When impurities (such as As) are added to the host the excess charge resides generally in the band gap, as represented in Figure I-1(a), and usually close to the conduction band so that even a small applied field will partially populate this band. Analysis of this situation is essentially a semiclassical problem because of the large number of conduction states into which the electrons can move.

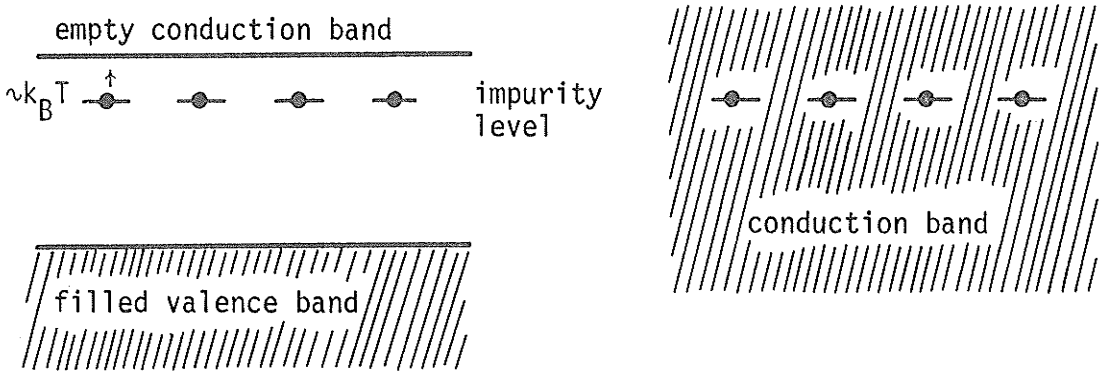

FIG. I-1 (a) Extrinsic (impurity) semiconductor e.g. As in Si. (b) Dilute alloy.

In the dilute alloy case, the one electron conduction band of the host metal is very broad, and the impurity level will most probably lie within this band. Refer to Figure I-1(b). Depending of course on the particular host and impurity used, properties like resistivity and magnetic susceptibility will behave in different ways with changes in temperature and impurity concentration. Dilute alloy models will be looked at in more detail in an attempt to predict the behaviour of some of these properties.

I.2 Screening[4]

Possibly the simplest alloy to consider is one formed by dissolving a single impurity atom into a noble metal host. Consider in particular an alloy with a 3-d transition impurity that contains only a single d electron. Assuming that the d electron lies in the conduction band of the host, it can now become itinerant leaving behind an excess positive charge at the impurity site. An internal electric field cannot exist in such a metallic environment, at least not over macroscopic distances, consequently a charge cloud must build up around the impurity to screen out this excess charge.

The screening charge cloud should be d-like in character. The initial electron that decayed into the conduction band was a d electron and would leave behind a d-like potential which would "attract" d-like electrons more strongly than say s conduction electrons. This situation can equally well be described as a resonance effect with the d-like electrons "resonating" in the d-like potential of the impurity. Apart from some long range oscillations the excess charge is screened out over a distance of the order of the atomic radius.

The screening charge can be treated mathematically in terms of partial waves and phase shifts.[4] The impurity potential, in first approximation, can be considered spherically symmetric allowing a partial wave analysis of the scattering of conduction electrons. The effect is to produce a phase shift η_ℓ in each wave of orbital quantum number ℓ; the screening condition in a conducting environment is the well known Friedel sum rule:[4]

$$Z = \frac{2}{\pi} \sum_{\ell} (2\ell + 1) n_{\ell}(\epsilon_F) \qquad \text{I.1}$$

where Z is the excess charge accumulated in the region of the impurity. In the present consideration where d-like components heavily dominate, $\ell = 2$ is regarded as the only contribution that is not vanishingly small, whence $Z = \frac{10}{\pi} n_2(\epsilon_F)$. A further consequence of the phase shifts is a long range oscillation in charge density with amplitude falling off as the inverse of the cube of the distance. Far from the impurity site the charge density has the form:

$$\delta n(r) = \frac{\alpha}{r^3} \cos(2k_F r + \phi) \qquad \text{I.2}$$

I.3 Virtual Bound State

Considering an isolated single d electron atom, the d electron is bound for all time by the potential of the atomic core. This is a true bound state. If the atom is now placed in a metallic host, the d electron decays into the conduction band and a charge density builds up around the ion to screen out the excess charge. No particular electron forms this charge cloud, but rather, a component of the total wave function $|\psi\rangle$ contributes, in a time average, a fixed amount of charge necessary for screening. This is called a "virtual bound state" (VBS). It results from the resonant scattering of $\ell = 2$ spherical wave components from the impurity potential. The VBS is characterized by a mean energy E, which Daniel and Friedel[4] show is shifted upward from the isolated atom energy eigenvalue E_d by an amount Γ which is proportional to the mixing probability between conduction states and d-states, and broadened by an energy width 2Δ.

$$E = E_d + \Gamma$$

where $$\Gamma = \text{p.p.} \int \frac{|\langle d|H_{Sd}|\underline{k}\rangle|^2}{\epsilon - E_{\underline{k}}} \, d^3\underline{k} \qquad \text{I.3}$$

$$\Delta = \pi\{|\langle d|H_{Sd}|\underline{k}\rangle|^2\}_{\text{ave.}} \, g(\epsilon)$$

Figure I-2 shows the effect of the virtual bound state on the density of states of the system.

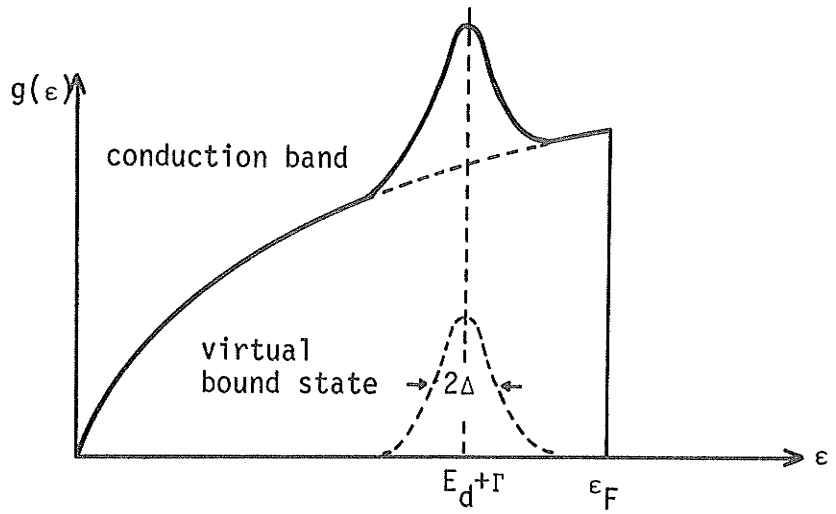

FIG. I-2. Effect of the virtual bound state on density of states verses energy.

The probability of finding an electron in the d-state is then,

$$|c|^2 = \frac{|\langle d|H_{Sd}|\underline{k}\rangle|^2}{(\epsilon - E_d - \Gamma)^2 + \Delta^2} \qquad \text{I.4}$$

Using the average value of the matrix element between states d and $\underline{k}$, and the expression for Δ (I.3), an expression for the density distribution $\rho_d(\epsilon)$, of the d-virtual-bound-state is:

$$\rho_d(\varepsilon) = |c|^2 \, g(\varepsilon) = \frac{1}{\pi} \frac{\Delta}{(\varepsilon - E)^2 + \Delta^2} \qquad \text{I.5}$$

where E and Δ are as defined above. This particular expression will be used in a later section to determine the effective spin at an impurity site.

I.4 Magnetic Localized States

Up to now it has been assumed that the virtual bound state has the same energy for both spin orientations. This, in general, is not true because of an exchange interaction between any two states on the same site. The d electrons in the virtual bound states are almost as well localized as they are in the isolated atoms, and might well be expected to obey a Hund's-like Rule. Exchange integral evaluations, in fact, show that the energy for parallel-spin and antiparallel-spin situations is different. This energy difference, often called the Coulomb repulsion energy, U, between opposite spins, may considerably modify the alloy picture. Depending upon the ratio of magnitudes of U and the VBS width 2Δ, considerably different models must be invoked. Figure I-3 illustrates three particular situations. Figure I-3 (a),

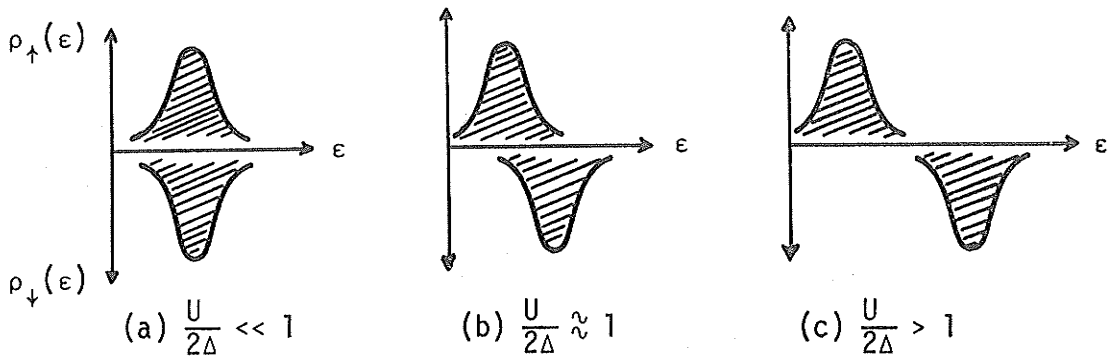

(a) $\frac{U}{2\Delta} << 1$ (b) $\frac{U}{2\Delta} \approx 1$ (c) $\frac{U}{2\Delta} > 1$

FIG. I-3

where U is nearly zero, depicts the situation that has been under discussion up until now. There is no spin preference, so the effect of spin may be largely ignored. Experimentally this is the situation observed in aluminum alloys containing first row transition metal impurities[5]. Figure I-3 (b) shows an intermediate situation, and Figure I-3 (c) illustrates a large splitting energy and exemplifies alloys with well-defined local moments.

So far no cognizance has been given to the fact that the d-band of a transition element is usually not completely filled to its capacity of five electrons in each spin sub-state. Indeed, in crossing the 3-d group from Sc to Zn there is a continual increase in the population of this band. What effect does this have? With U very large, the magnitude of the local moment increases from Sc to Mn (which have 5 d electrons) and then decreases toward Zn. This is illustrated in Figure I-4. The d-state threshold energy and the Fermi energy will adjust themselves in a self-consistent manner so that they lie at the same level. For U = 0, the sub-states will be equally populated so that no net magnetic moment will result, and the alloy will thus exhibit no magnetic character. The third case of $U/\Gamma \sim 1$ is some sort of compromise of characteristics; it will show a magnetic moment, but not one strongly localized. In any case, the d-state population effects many physical properties because it effects the density of states at the Fermi level. Examination of the "Golden Rule",

$$W(\underline{k},\underline{k}') = \frac{2\pi}{\hbar} |\langle \underline{k}' | H_i | \underline{k} \rangle|^2 \rho(\epsilon_F) \qquad \text{I.6}$$

where $W(\underline{k},\underline{k}')$ is the transition probability for scattering of a conduction electron from state $\underline{k}$ to $\underline{k}'$, shows, for example that the

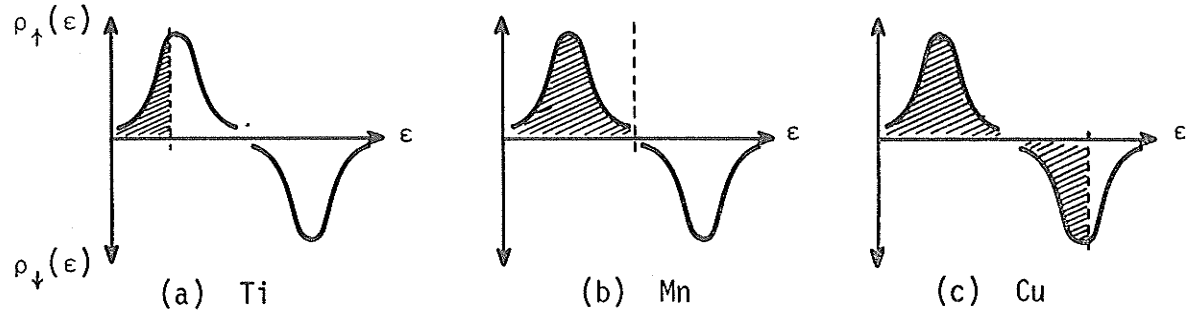

FIG. I-4

incremental resistivity, $\Delta\rho$, which is directly proportional to the scattering transition probability, is therefore directly proportional to the Fermi level density of states, $n(\varepsilon_F)$. Other properties such as magnetic susceptibility and specific heat are also strongly dependent upon $n(\varepsilon_F)$. The population of the 10-fold degenerate d-band and the exchange energy are thus important parameters in the present study of alloys.

I.5 The Anderson Model[6]

The Anderson Hamiltonian for alloys containing localized moments is

$$H = H_{of} + H_{od} + H_{corr} + H_{sd} \qquad \text{I.7}$$

Here, H_{of} is the unperturbed energy of the free-electron system. In second quantized notation it is:

$$H_{of} = \sum_{k,\sigma} \varepsilon_{\underline{k}}\, c^*_{\underline{k}\sigma}\, c_{\underline{k}\sigma} \qquad \text{I.8}$$

where $c^*_{\underline{k}\sigma}$ and $c_{\underline{k}\sigma}$ are the creation and annihilation operators for an electron with spin σ and wavevector $\underline{k}$. H_{od} is the unperturbed energy of the d-states on the impurity atom. A single non-degenerate d-level is used here to more easily express the ideas; the more correct many-levelled d-shell Anderson shows to be a relatively easy extension. In second quantized form:

$$H_{od} = E(n_{d\uparrow} + n_{d\downarrow}). \qquad \text{I.9}$$

The localized d-state eigenfunction ϕ_d is treated as a separate state here, and not as an impurity potential acting on the free electron gas. To some extent this is physically justifiable by visualizing ϕ_d as an inner shell level. Mathematically this allows ϕ_d to be orthogonal to the free-electron-band Wannier functions, and simplies the analysis.

The correlation energy, H_{corr}, is a repulsive energy among the d-functions of opposite spin.

$$H_{corr} = Un_{d\uparrow}n_{d\downarrow} \qquad \text{I.10}$$

where U is an exchange integral of the type

$$U = \int \phi_d^*(\underline{r}_1)\phi_d^*(\underline{r}_2)\frac{e^2}{|\underline{r}_1 - \underline{r}_2|}\phi_d(\underline{r}_1)\phi_d(\underline{r}_2)\, d\tau_1\, d\tau_2.$$

Correlation effects between electrons in the "free" states and between d and "free" electrons are ignored. Energy-level tables show them to be smaller, but the main argument to justify this is that the conduction electrons are very much spread out compared especially to the narrow d-band, and thus exchange interactions will be much smaller.

The final term in the Hamiltonian is the s-d interaction term. It is purely a one electron effect and represents the s $\rightarrow$ d or d $\rightarrow$ s

"hopping" possibility:

$$H_{sd} = \sum_{\underline{k},\sigma} V_{d\underline{k}}(c^*_{\underline{k}\sigma}c_{d\sigma} + c^*_{d\sigma}c_{\underline{k}\sigma}) \qquad \text{I.11}$$

$V_{d\underline{k}}$ is the transition potential and is taken to have equal magnitude for a "hop" in either direction.

This then describes the terms in the Anderson Hamiltonian. Written completely in second quantized form, it is

$$H = \sum_{\underline{k},\sigma} \varepsilon_{\underline{k}} C^*_{\underline{k}\sigma} C_{\underline{k}\sigma} + E(n_{d\uparrow}+n_{d\downarrow}) + Un_{d\uparrow}n_{d\downarrow} + \sum_{\underline{k},\sigma} V_{d\underline{k}}(C^*_{\underline{k}\sigma}C_{d\sigma} + C^*_{d\sigma}C_{\underline{k}\sigma}). \qquad \text{I.12}$$

Consider now the simple case depicted in Figure I-5(a). An up-spin d electron has a discrete energy $E_{d\uparrow} = E$ situated well below the

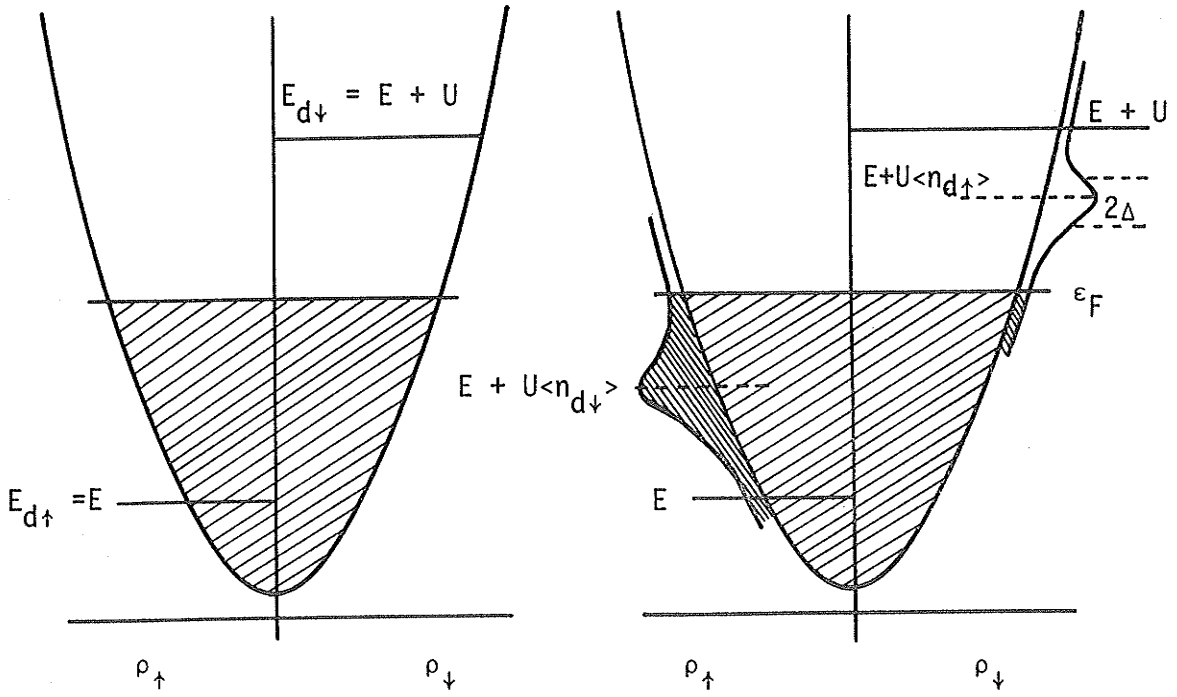

FIG. I-5. (a) Unperturbed energy levels in the absence of s-d admixture. (b) Density of states distribution in a magnetic case.

Fermi level. The spin-down energy is then $E_{d\downarrow} = E + U$, and is assumed to sit well above the Fermi level. If the system contains a single d electron it will fall into the up-spin state and the other state will remain empty. The d electron will thus have a net mean spin $s = \frac{1}{2}$, yielding a "magnetic" state. The orbital spin will be quenched by electrostatic "binding" in the crystal field.

In view of the virtual bound state treatment given earlier it is expected that the discrete energy levels just described will be modified into virtual states with energy shifted from E by an amount proportional to the s-d transition probability and so is broadened into a state whose width is proportional to the average transition probability. Figure I-5(b) illustrates this situation. The average occupation of the up-spin state is now less than one, and that of the down-spin state is greater than zero, but of course their sum is still unity; $\langle n_{d\uparrow} \rangle + \langle n_{d\downarrow} \rangle = 1$. Now both states may be occupied, leading in general to a mean spin less than one-half. The two spin states will be filled roughly to the Fermi level, so for each state $E + \langle n_{d\sigma} \rangle U = \varepsilon_F$.

In section I.3, an expression was derived for the density distribution of the d-state in the VBS analysis. This must now be slightly modified to account for the spin degeneracy of the density distribution. Thus:

$$\rho_{d\sigma}(\varepsilon) = \frac{1}{\pi} \frac{\Delta}{(\varepsilon - E_\sigma)^2 + \Delta^2} \qquad \text{I.13}$$

with $E_\sigma = E + U\langle n_{d\sigma} \rangle$. Since all states below the Fermi energy are full, the integral of the density function up to ε_F must equal the average d-state occupation.

$$\langle n_{d\sigma} \rangle = \frac{1}{\pi} \int_{-\infty}^{\epsilon_F} \frac{\Delta d\epsilon}{(\epsilon - E\sigma)^2 + \Delta^2} \qquad \text{I.14}$$

$$= \frac{1}{\pi} \cot^{-1}\left(\frac{E\sigma - \epsilon_F}{\Delta}\right)$$

This is really two equations, since there are two spin states, and a self-consistent treatment requires the simultaneous solution of the following pair of equations:

$$\langle n_{d\uparrow} \rangle = \frac{1}{\pi} \cot^{-1}\left(\frac{E - \epsilon_F + U\langle n_{d\downarrow} \rangle}{\Delta}\right) \qquad \text{I.15}$$

$$\langle n_{d\downarrow} \rangle = \frac{1}{\pi} \cot^{-1}\left(\frac{E - \epsilon_F + U\langle n_{d\uparrow} \rangle}{\Delta}\right)$$

Two possible solutions of these equations are presented in Figure I-6, where in both cases a value of $(\epsilon_F - E)/U = \frac{1}{2}$ is used for simplicity.

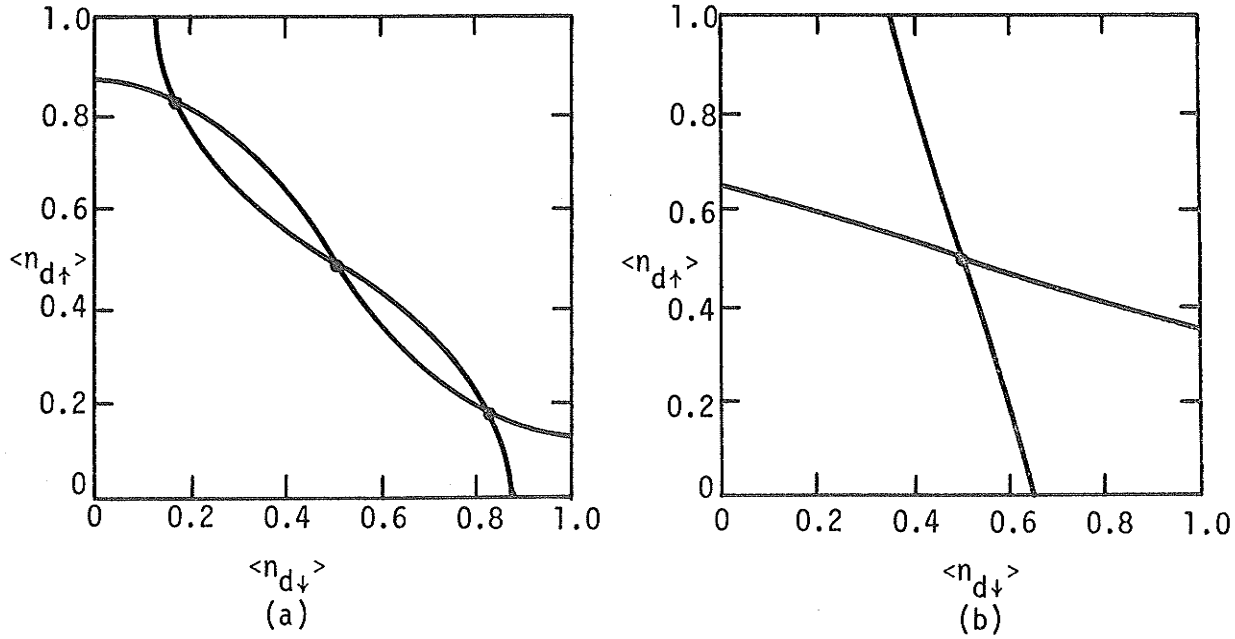

FIG. I-6. (a) Self-consistency plot of $\langle n_{d\uparrow} \rangle$ vs. $\langle n_{d\downarrow} \rangle$ for a typical magnetic case. $U/\Delta = 5$ and $(\epsilon_F - E)/U = 1/2$. Note three possible solutions. (b) A typical nonmagnetic case; $U/\Delta = 1$.

In Figure I-6(a), $U/\Delta = 5$ (where 2Δ is the half width of the VBS density spike) and three self-consistent solutions ensue. The center solution is for $\langle n_{d\uparrow} \rangle = \langle n_{d\downarrow} \rangle$ and, since the magnetic moment is proportional to the difference in spin densities ($m = \langle n_{d\uparrow} \rangle - \langle n_{d\downarrow} \rangle$), correspondends to a non-magnetic case. The other two points are magnetic solutions (for which $m = 0.644$). The magnetic solutions are favoured energetically: this can be seen by substituting the values for $\langle n_{d\uparrow} \rangle$ and $\langle n_{d\downarrow} \rangle$ into an expression for the mean value of the correlation energy $\epsilon_{corr} = U\langle n_{d\uparrow} \rangle \langle n_{d\downarrow} \rangle$. Figure I-6(b) shows that for $U/\Delta = 1$ there is only one solution for the system, corresponding to $m = 0$, a non-magnetic situation. It is thus clear that the magnetic nature of the alloy system depends upon the parameters $(\epsilon_F - E)/U$ and U/Δ. One can see that for a given value of the first parameter there is a critical value of the second one which gives one solution to equations I.15, and any larger value will produce three solutions. The set of critical values marks the transition from the non-magnetic to the magnetic state; this is illustrated in Figure I-7.

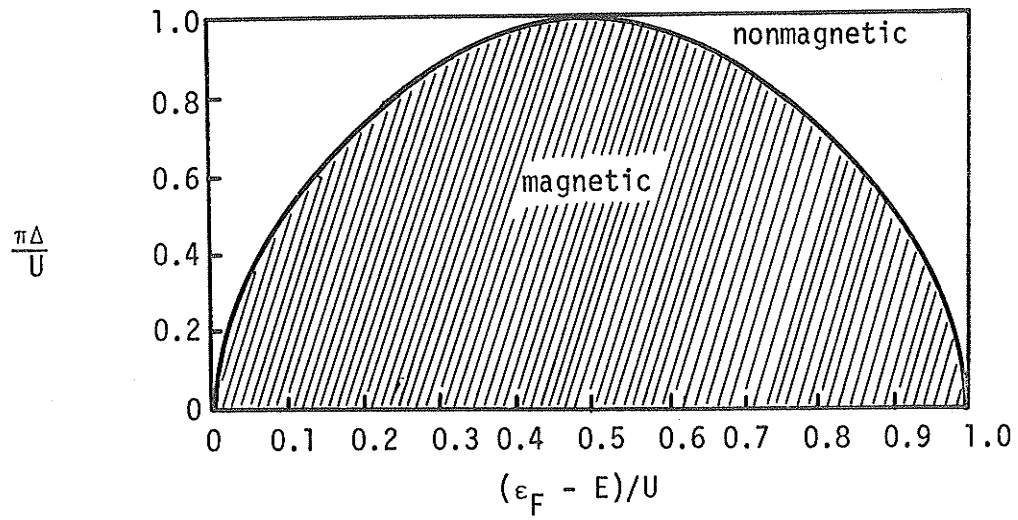

FIG. I-7. Regions of magnetic and nonmagnetic behaviour.

The Anderson model enjoys greatest success for alloys formed by dissolving transition elements (d- or f-types) into "simple" metals such as Au, Ag and Cu. It is as well, however, a rather fundamental model for dilute alloys, and physical concepts evolved by it are applicable to many alloy systems. Certain limiting cases can be investigated in more depth; the next section is one such case.

I.6 The "s-d" Model

The s-d model was first proposed by Zener[7] and by Fröhlich and Nabarro[8] on a phenomenological basis. These authors considered an exchange interaction between d electrons assumed localized at the atomic sites and s electrons itinerant over the range of the crystal. The coupling Hamiltonian is written:

$$H_{sd} = V - 2J\underline{S}\cdot\underline{s} \qquad \text{I.16}$$

where V in the alloy is the potential integral, a spin-independent deviation due to the excess charge associated with the impurity ion; J is the effective local moment exchange integral; and $\underline{S}$ and $\underline{s}$ are spin operators representing the local moment and the conduction electron respectively.

For the condition of a well defined local impurity spin, as considered in this model, Schrieffer and Wolff[9] have shown that the Anderson Hamiltonian transforms to this model Hamiltonian. The condition requires that $U/\Delta >> 1$, which at the same time requires that $V_{\underline{k}d}$ is very small. Under these conditions, it can be shown[2] that J is approximately constant and given by:

$$J = 2\left|V_{\underline{k}d}\right|^2 \frac{U}{E_d(E_d + U)} . \qquad \text{I.17}$$

I.7 RKKY Oscillations

In first order at least, the s-d model is very transparent. A 3-d impurity atom has a distinct spin at a distinct location. Itinerant conduction electrons also have distinct spins, but are free to move throughout the crystal. There is an interaction between the two "particles" composed of two basic parts. First, there is an ordinary Coulomb interaction between the conduction electron charge and the excess charge at the impurity site, and second, there is an exchange interaction due to spin coupling (assumed to be a Heisenberg form).

One can, however, envisage a second order electron-electron interaction between impurity moments. This arises from a conduction electron scattering from one impurity, propagating with that spin information to the second impurity, and scattering from it in a way dependent upon its local moment. A calculation based on such a physical picture was first carried out by Ruderman and Kittel[10], and later by Kasuya[11] and Yosida[12] on the s-d model which has lead to what is now known as the Ruderman-Kittel-Kasuya-Yosida (RKKY) oscillations. The oscillatory form of the charge density centered at an impurity site has been shown to have the following asymptotic form[2]:

$$\delta n(r) = \sum_{\sigma} \frac{\alpha_\sigma}{2\pi^2} \left| \frac{\cos(2k_F r + \phi_\sigma)}{r^3} \right| \qquad \text{I.18}$$

where σ denotes spin, α_σ is a spin dependent amplitude factor, ϕ_σ is a spin dependent phase shift, and k_F is a wave vector at the Fermi surface. Figure I-8 illustrates the electron density around an impurity ion. The central peak is the screening charge localized roughly within atomic dimensions (radius indicated by arrows) and this merges into the

RKKY density oscillations which oscillate with a period $(2k_F)^{-1}$ and which decay only as the inverse cube of the distance.

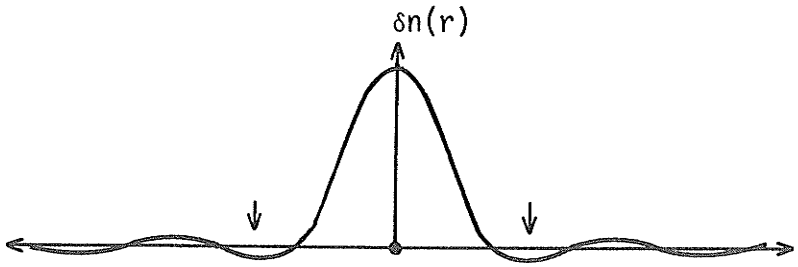

FIG. I-8. Electron distribution around an impurity.

I.8 Exchange Enhancement-Giant Moments

Exchange enhancement and the giant moment effect are direct consequences of the electron-electron interactions in the conduction band of the host metal. The d-type electrons often exist in a very narrow band. In such a case one would expect there to be large coupling interactions among these electrons. For a host like palladium which has a large d-component in the metallic wave function, a very strong interaction should exist.

When a d-transition impurity is present in a host where electron-electron correlation effects are important, the RKKY spin density oscillation will be subject to the effects of exchange enhancement. The susceptibility at and near the site will be dramatically increased, and the range of the spin polarization will be broadened.

A good deal of theoretical work has been done on this problem. Moriya[13,14], for example, has solved the electron-electron interaction for both the Anderson and Wolff-Clogston[15] (tight band) models. For

clarity, however, a different approach is considered here; first the effect of electron-electron interactions in the pure host is considered, and then the modifications resulting from the interactions on the spin polarization centered about the impurity site.

Wolff[16] has calculated the enhanced Pauli susceptibility of a pure system in which the electron-electron interactions are important to be:

$$\chi(q) = 2\mu_B{}^2 \frac{N(\epsilon_F)L(q/2k_Fr)}{1 - N(\epsilon_F)VL(q/2k_Fr)} \qquad \text{I.19}$$

where μ_B is the Bohr magneton, $N(\epsilon_F)$ is the density of states at the Fermi surface, V is the Fourier transform of the Coulomb interaction and is assumed to act only between electrons on the same site, and L(x) is the Lindhard function given by:

$$L(x) = \frac{1}{2}\left[1 + \frac{1-x^2}{2x} \ln\left|\frac{1+x}{1-x}\right|\right]$$

L(x) has a shape like that of the unenhanced curve in Figure I-9. The denominator is the so called enhancement factor; its effect on the susceptibility is illustrated in Figure I-9[2] for the case $N(\epsilon_F)V = 0.9$. Note that the enhanced susceptibility increases rapidly with decreasing q. For the case of $N(\epsilon_F)V = 1$, the susceptibility $\chi(0)$ becomes infinite, implying the existence of ferromagnetic order. Since $N(\epsilon_F)V = 0.86$ for palladium only a small amount of impurity is needed to send the system ferromagnetic.

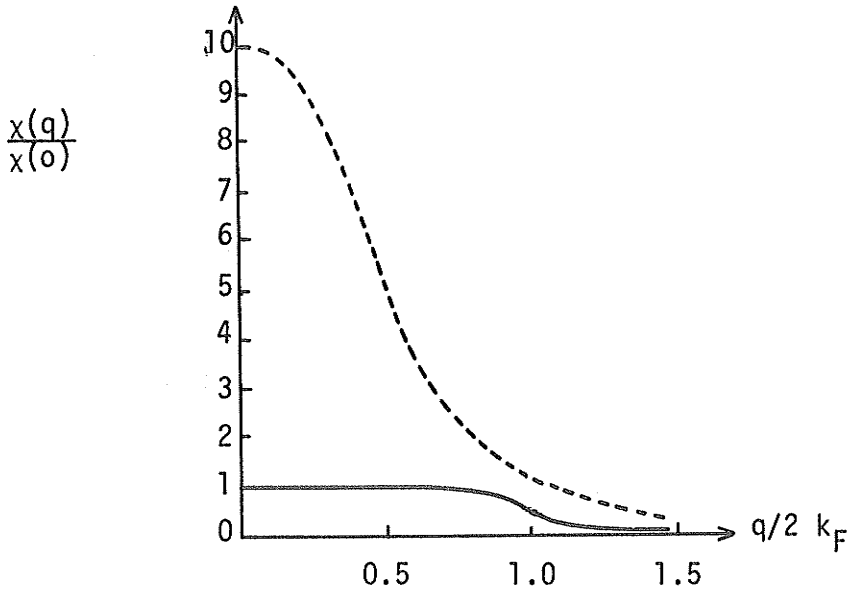

FIG. I-9. Enhancement of q-dependent susceptibility.

Consider now the introduction of a localized impurity moment into some host in which such enhancement effects are important. The spin polarization $\delta n(r)$ around an impurity is plotted in Figure I-10[17] for $N(\epsilon_F)V = 0$ and $N(\epsilon_F)V = 0.86$. The strength of the polarization is magnified greatly in the proximity of the impurity site, and the long range oscillations are pushed much further out. Since $J > 0$, the enhanced polarization will couple ferromagnetically (align parallel) to the local moment creating a magnified moment at the site. This is the <u>giant moment</u> (it is in effect the local impurity moment plus the exchange enhanced d-band polarization.) An expression for the spin distribution in this type of system is:

$$\delta n(\underline{r}) = \frac{J}{2} \langle S_z \rangle \sum_{\underline{q}} \chi(\underline{q}) e^{i\underline{q}\cdot\underline{r}} \qquad \text{I.20}$$

where J is the local moment-conduction electron coupling constant, and $\langle S_z \rangle$ is the expectation value of the axial spin operator for the local moment. The extended range of the polarization increases the possibility that moments at neighbouring sites will overlap. In palladium alloys, for example, where $N(\epsilon_F)V = 0.86$ the first zero in the spin polarization distribution is nearly 6 Å from the impurity site. Overlap will thus occur for alloys as dilute as about 0.2 atomic per cent. For temperatures below the Curie point, where thermal energy is smaller than the magnetic energy associated with the coupling of giant moments, ferromagnetic order should prevail.

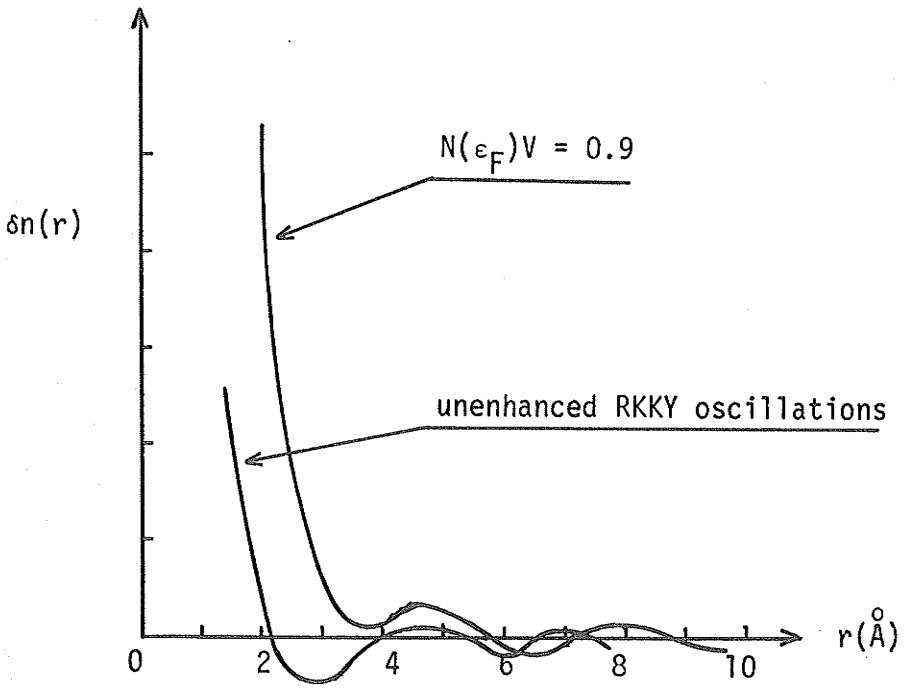

FIG. I-10. Long range spin polarization.

I.9 Ferromagnetic Giant Moment Coupling

The alloy model being discussed has evolved through a number of distinct sophistications. Here is a review: a 3-d transition impurity (such as Fe or Co) is added to a host metal which itself contains d-like electrons in the conduction band (e.g. Pd). The decay of impurity d electrons into the conduction band and the subsequent d-like screening charge that is created at the impurity site produces a "virtual bound state", and the spin polarization associated with it is further enhanced by interactions within the d-component of the conduction band. The enhancement is characterized by a broadening of the local charge distribution which results in an overlap of spin polarizations associated with impurities separated by as much as 10 Å, and a ferromagnetic coupling between impurity moments.

It is precisely this model that Doniach and Wohlfarth[18] treat theoretically using a Heisenberg ("s-d") Hamiltonian to describe the exchange coupling between localized impurity moments and the electrons moving in the narrow d-band. The narrowness of this band is an essential feature; it leads to a coupling of the type $-J\underline{S}_i \cdot \underline{S}_j$, $J > 0$, between impurities, which is the characteristic format for spin wave excitations[19]. Further, one expects two branches of the spin wave spectrum to exist since there are two inequivalent contributions to the total magnetization, one from local moments ($\underline{S}_{local}$) and one from d-band polarization ($\underline{S}_d$). Doniach and Wohlfarth in fact predict this on the basis of their model. One branch, the acoustic branch has low lying spin wave like excitations possessing zero energy in the long wavelength limit; a second or optical branch, which increases in energy in the long wavelength limit, has much higher energy and would be expected to be of little importance

in the low temperature regime. Refer to Figure I-11[18].

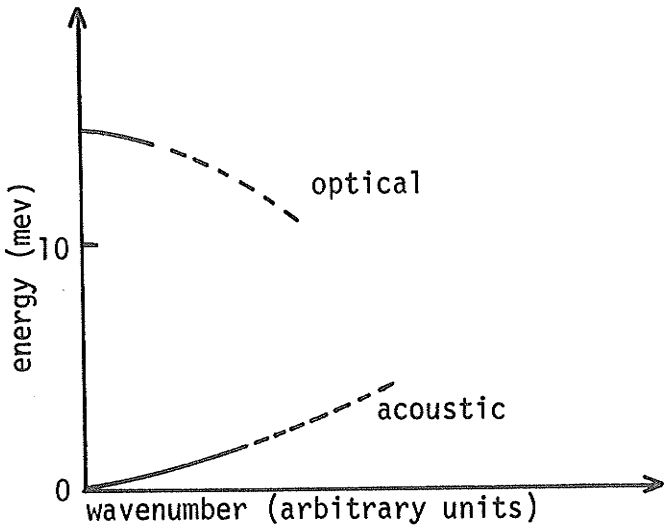

FIG. I-11. Sketch of predicted spin wave spectrum of a 1% PdFe alloy.

Particular consideration will now be given to relatively concentrated dilute alloys; that is, alloys with impurity concentrations on the order of 2 to 10 atomic per cent. This is the range where one might well expect ferromagnetic overlap of the giant moments. Shalski et. al.[20] investigated PdFe alloys in this concentration range and concluded that the dominant contribution to the incremental resistivity, $\Delta\rho(T)$, of the alloy was due to conduction s-electron-local moment exchange coupling, or, in short, electron-magnon scattering. The Hamiltonian describing this scattering denoted $H_{s\text{-}local}$, is written following Kasuya[11] and Yosida[12],

$$H_{s\text{-}local} = N^{-1} \sum_{\underline{k}} \sum_{\underline{k}'} \sum_{\underline{R}_i} e^{i(\underline{k}-\underline{k}')\cdot\underline{R}_i} \{[V(\underline{k},\underline{k}') - J(\underline{k},\underline{k}')]a^*_{\underline{k}'\uparrow} a_{\underline{k}\uparrow} S_i^z + [V(\underline{k},\underline{k}') + J(\underline{k},\underline{k}')]a^*_{\underline{k}'\downarrow} a_{\underline{k}\downarrow} S_i^z - J(\underline{k},\underline{k}')[a^*_{\underline{k}'\uparrow} a_{\underline{k}\downarrow} S_i^- + a^*_{\underline{k}'\downarrow} a_{\underline{k}\uparrow} S_i^+]\} \quad \text{I.21}$$

N is the number of lattice sites per unit volume; a* (a) is the creation (annihilation) operator for the appropriate conduction electron; $\underline{R}_i$ labels impurity sites and S_i^z, $S_i^{\pm}$ are the appropriate impurity spin operators. $V(\underline{k},\underline{k}')$ and $J(\underline{k},\underline{k}')$ are the potential and the exchange integrals. This is nothing more than an expansion of the phenomenological Hamiltonian considered in section I.6 (equation I.16) written in second quantized form, and using the more descriptive term $H_{s\text{-local}}$ instead of H_{sd}. The Golden Rule (I.6) is invoked to obtain the scattering probabilities, $P(\underline{k}\uparrow\downarrow,\underline{k}'\uparrow\downarrow)$, from conduction electron state $\underline{k}\uparrow\downarrow$ to state $\underline{k}'\uparrow\downarrow$. Spin orientations are parallel ($\uparrow$) or antiparallel ($\downarrow$) to the z-axis, and for $T << T_c$ where the dynamic behaviour of the impurity spin system is approximated by spin waves the local spin operators (S_i^z, $S_i^{\pm}$) are transformed to spin wave variables. The dominant scattering terms (neglecting three and four operator terms at low temperature) are[21]:

$$P(\underline{k}\uparrow\downarrow:\underline{k}'\uparrow\downarrow) = \frac{2\pi C}{\hbar N}\{|V(\underline{k},\underline{k}')|^2 \mp 2(S - \frac{1}{N}\sum_{\underline{q}} n_{\underline{q}})|V(\underline{k},\underline{k}')||J(\underline{k},\underline{k}')| +$$

$$(S^2 - \frac{2S}{N}\sum_{\underline{q}} n_{\underline{q}})|J(\underline{k},\underline{k}')|^2\}f(\underline{k})[1-f(\underline{k}')]\cdot\delta(\epsilon_{\underline{k}} - \epsilon_{\underline{k}'})\cdot\delta(\underline{k}-\underline{k}')$$

$$P(\underline{k}\downarrow;\underline{k}'\uparrow) = \frac{4\pi Sc}{\hbar N}|J(\underline{k},\underline{k}')|^2 n_{\underline{q}} f(\underline{k})[1-f(\underline{k}')] - \delta(\epsilon_{\underline{k}}-\epsilon_{\underline{q}}-\epsilon_{\underline{k}'})\cdot\delta(\underline{k}-\underline{q}-\underline{k}')$$

$$P(\underline{k}\uparrow;\underline{k}'\downarrow) = \frac{4\pi Sc}{\hbar N}|J(\underline{k},\underline{k}')|^2 (n_{\underline{q}}+1)f(\underline{k})\ [1-f(\underline{k}')]\cdot\delta(\epsilon_{\underline{k}}+\epsilon_{\underline{q}}-\epsilon_{\underline{k}'})\cdot\delta(\underline{k}+\underline{q}-\underline{k}') \qquad \text{I.22}$$

where $\epsilon_{\underline{q}}$ and $n_{\underline{q}}$ are the energy and number operator, respectively, for spin waves of wave vector $\underline{q}$; and the factor c, representing concentration, is a result of computing an ensemble average over all impurity spin positions. The f's are the Fermi factors.

Finally, then, solving the Boltzman equation with the above scattering probabilities in a manner outlined by Kasuya[22] and Mannari[23], one obtains for the incremental resistivity[21]:

$$\Delta\rho(T<<T_c) = \frac{3\pi m^* c}{2e^2\hbar N\epsilon_F}\left[|V|^2 + \frac{\pi^2|J_{s\text{-}local}|^2 S}{12}\left(\frac{k_B T}{Dk_F^2}\right)^2\right] \qquad \text{I.23}$$

Here, m* is the effective mass of s-band electrons; ϵ_F and k_F are the Fermi energy and wave number, respectively; k_B is Boltzman's constant and D is the acoustic spin wave stiffness (defined by $\epsilon_q = Dq^2$).

Equation I.23 thus predicts that the incremental resistivity of a relatively concentrated alloy system formed by dissolving a 3-d transition element into a host characterized by an exchange-enhanced susceptibility should be equal to some constant term, due to simple potential scattering, plus a term which varies as the square of the absolute temperature.

I.10 Local Spin Fluctuations

In the previous section consideration was given to enhanced systems containing well defined local magnetic moments, a condition equivalent to saying $U \to \infty$, where U is the Coulomb repulsion between up- and down-spin states. In the present discussion the restriction on U is relaxed, but specific consideration is given to dilute alloys with nearly magnetic impurities.

Dilute alloys which fall into the category of "nearly magnetic" include RhFe[24] and IrFe[25], and are characterized by an impurity resistivity component which changes gradually from a T^2 to a T temperature dependence, and at sufficiently high temperatures flattening out to something much less than a T dependence.

The mechanism that accounts for this resistivity component is believed to be due essentially to conduction electron-spin fluctuation scattering events. A host metal, which may or may not exhibit enhanced susceptibility, containing 3-d transition metal impurities will support localized moments (virtual bound states, as earlier discussed), but these may not be well defined; in fact, in a time average, there will be no observable moment due to the constant flipping of spin. The fluctuations in the localized spin will scatter conduction electrons provided the spin fluctuation lifetime, τ_{sf}, is greater than the thermal fluctuation lifetime, $\tau_{thermal}$. If τ_{sf} is less than $\tau_{thermal}$, the conduction electron does not "see" a magnetic moment and no magnetic scattering exists. The mathematical analysis of this conduction electron-spin fluctuation system is quite involved; the results to be discussed here are due to the theoretical analysis of Kaiser and Doniach[26]. In this paper the authors derive an expression for the resistivity of the dilute alloy with nearly magnetic impurities as a function of temperature. It is

$$\tilde{\rho} = \frac{1}{\tilde{T}} \int_0^\infty d\tilde{\omega} \; \frac{\tilde{\omega}^2}{[\exp(\tilde{\omega}/\tilde{T})-1][1-\exp(-\tilde{\omega}/\tilde{T})][1+\tilde{\omega}^2]} \qquad \text{I.24}$$

where $\tilde{\rho}$ is a dimensionless "reduced" resistivity, $\tilde{\omega}$ is an integration parameter such that $\tilde{\omega} = \frac{\omega}{k_B T_s}$ and $\omega = \varepsilon_{\underline{k}'} - \varepsilon_{\underline{k}}$, k_B is Boltzman's constant, and $\tilde{T} = \frac{T}{T_s}$, T_s being a characteristic temperature of the system. T_s is defined such that $k_B T_s$ is the energy of the peak of the localized spin fluctuation excitation spectrum, and is related to τ_{sf} by $\tau_{sf} = \frac{\hbar}{k_B T_s}$. The low and high temperature limits of equation I. 24 are:

$$\tilde{\rho}(T \to 0) = \frac{\pi^2}{3}\left(\frac{T}{T_s}\right)^2$$

$$\tilde{\rho}(T \to \infty) = \frac{\pi}{2}\,\frac{T}{T_s} \qquad \text{I.25}$$

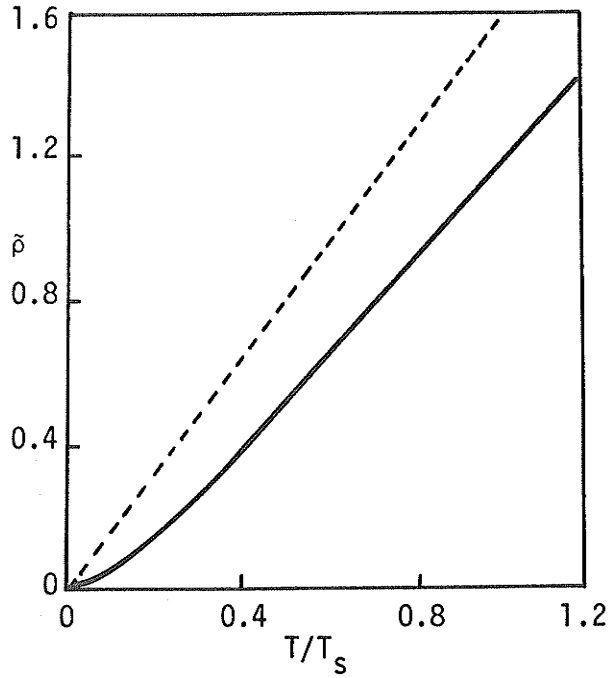

FIG. I-12. Universal curve for spin fluctuation resistivity calculated from (I.24). The dotted line is the high temperature limit.

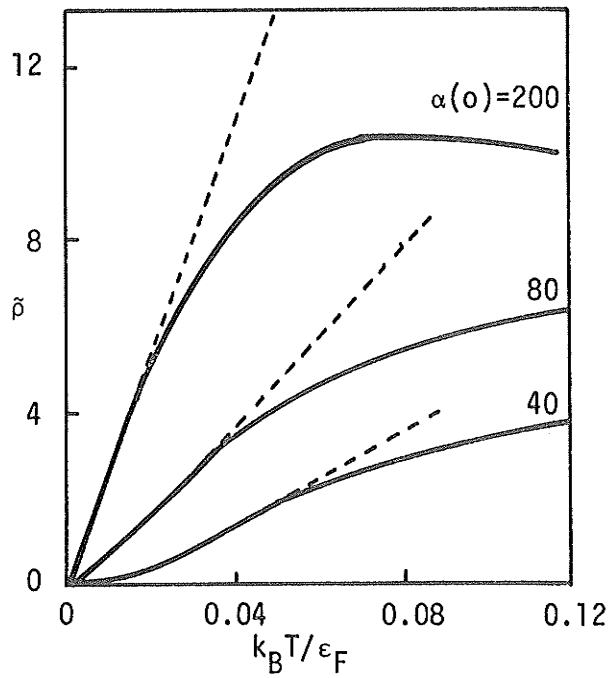

FIG. I-13. Effect on resistivity curves of the temperature dependence of $\alpha(T)$.

The universal curve for spin fluctuation resistivity as calculated from equation I.24 and illustrated in Figure I-12 exhibits a transition from T^2 to T dependence at approximately $\frac{1}{4}\,T_s$. When the temperature dependence of the enhancement factor $\alpha(T)$ is accounted for, the model predicts a resistivity that flattens off rapidly at high temperatures, (refer to Figure I-13) a result which, qualitatively at least, is in agreement with experiment[24,25].

The usual assumption is made, that scattering probabilities for different scattering mechanisms are independent, or in other words, that Mattheissen's Rule applies. Resistivity components are thus additive, so

$$\rho_{imp}(T) = \rho_{alloy}(T) - \rho_{host}(T) \qquad \text{I.26}$$

where $\rho_{imp}(T)$ is assumed to be composed of two components

$$\rho_{imp}(T) = \rho_{mag}(T) + \rho_{non\text{-}mag} \cdot \qquad \text{I.27}$$

In this equation, $\rho_{non\text{-}mag}$ is taken to be equal to $\rho_{imp}(0)$, and $\rho_{mag}(T)$ is the remaining spin fluctuation resistivity, which in the experimental analysis is the quantity of especial interest.

An expression for determining T_s from experimental data can be obtained by plotting the T^2 and T portions of the data separately. If the slope of $\rho(T)$ versus T^2 is S_2 and that of $\rho(T)$ versus T is S_1 then, using equations I.25 and assuming $\tilde{\rho} = \frac{\rho(T)}{\rho_o}$, the results of differentiation are:

$$S_2 = \frac{\pi^2}{3} \frac{\rho_o}{T_s^2} \qquad \text{I.28}$$

and $$S_1 = \frac{\pi}{2} \frac{\rho_o}{T_s}$$

It is assumed that ρ_o is temperature independent, at least from the upper end of the T^2 portion of the curve to the lower end of the T dependent portion. Finally, then, the solution of equations I.28 gives

$$T_s = \frac{2\pi}{3} \frac{S_1}{S_2} \qquad \text{I.29}$$

for the characteristic spin fluctuation temperature for dilute alloys with nearly magnetic impurities.

References

1. W. Meissner and G. Voigt, Ann. Physik 1, 761 (1930).

2. A. J. Heeger, Solid State Physics, Volume 23, edited by Frederick Seitz, David Turnbull and Henry Ehrenreich, Academic Press, New York, 1969, page 283.

3. J. Kondo, as in ref. 2, page 183.

4. E. Daniel and J. Friedel, Proceedings of the IXth International Conference on Low Temperature Physics (Columbus, 1964), Editors: J. G. Daunt, D. O. Edwards, F. J. Milford, and M. Yaqub (Plenum Press, New York, 1965), page 933.

5. A. D. Caplin and C. Rizzuto, Phys. Rev. Letters 21, 746 (1968).

6. P. A. Anderson, Phys. Rev. 124, 41 (1961).

7. C. Zener, Phys. Rev. 81, 440 (1951).

8. H. Fröhlich and F. R. N. Nabarro, Proc. Roy. Soc. A175, 382 (1940).

9. J. R. Schrieffer and P. A. Wolff, Phys. Rev. 149, 491 (1966).

10. M. A. Ruderman and C. Kittel, Phys. Rev. 96, 99 (1954).

11. T. Kasuya, Progr. Theor. Phys. (Kyoto) 16, 58 (1956)

12. K. Yosida, Phys. Rev. 106, 893 (1957).

13. T. Moriya, Proc. International School of Physics, Enrico Fermi Course XXXVII, edited by W. Marshall, Academic Press, 1967, page 206.

14. T. Moriya, Progr. Theor. Phys. (Kyoto) 34, 329 (1965).

15. P. A. Wolff, Phys. Rev. 124, 1030 (1961), A. M. Clogston, Phys. Rev. 125, 439 (1962).

16. P. A. Wolff, Phys. Rev. 120, 814 (1960).

17. B. Giovannini, M. Peter and J. R. Schrieffer, Phys. Rev. Letters 12, 736 (1964).

18. S. Doniach and E. P. Wohlfarth, Proc. Roy. Soc. A295, 442 (1967).

19. W. A. Harrison, "Solid State Theory", McGraw-Hill, New York, 1970.

20. S. Skalski, M. P. Kawatra, J. A. Mydosh and J. I. Budnick, Phys. Rev. B2, 3613 (1970).

21. M. E. Colp and Gwyn Williams, Phys. Rev. B5, 2599 (1972).

22. T. Kasuya, Progr. Theor. Phys., Japan, 22, 227 (1959).

23. I. Mannari, Progr. Theor. Phys., Japan, 22, 335 (1959).

24. B. R. Coles, Phys. Letters 8, 243 (1964).

25. M. P. Sarachik, Phys. Rev. 170, 679 (1968).

26. A. B. Kaiser and S. Doniach, Intern. J. Magnetism 1, 11 (1970).

CHAPTER TWO

APPARATUS

II.1 Introduction

The purpose of the introduction is to give an overview of the method and equipment used to obtain temperature dependent resistivities for the alloy systems.

Samples of alloys were prepared by melting together appropriate proportions of the pure elements in an argon arc furnace. Sets of up to six alloys (to be mounted in a 6-sample holder) of differing percentage composition were formed into long, thin specimens, typically about 9 cm. × 0.02 cm. × 0.2 cm. Small form factors (area to length ratios) were used to yield reasonably high resistance values ($\sim 10^{-3}$ ohms). Voltage and current measurements were made on the samples using a standard four probe technique[1]. Current through the samples was varied to balance a highly stable reference voltage using a Kiethley nano-voltmeter as a null detector.

Since resistivity as a function of temperature was being sought, a means of varying and controlling the temperature was necessary. Below 4.2 K, temperatures were obtained by pumping on a liquid helium bath, and stabilized with a manostat in the vapour line. Oil and mercury manometers were used to determine the precise temperatures. Above 4.2 K a heater in a feedback circuit obtained and regulated the temperatures, and the precise measurements were made with a nonlinear gas thermometer.

A more detailed discussion of the equipment now follows.

II.2 The Vacuum System

Figure II-1 shows a flow diagram of the vacuum system. The main pump, for refrigerating the helium bath and thus the samples, was an Edwards High Vacuum Ltd. Speedivac ES330 with a pumping capacity of about 330 liters per minute. A Speedivac vapour diffusion pump, backed

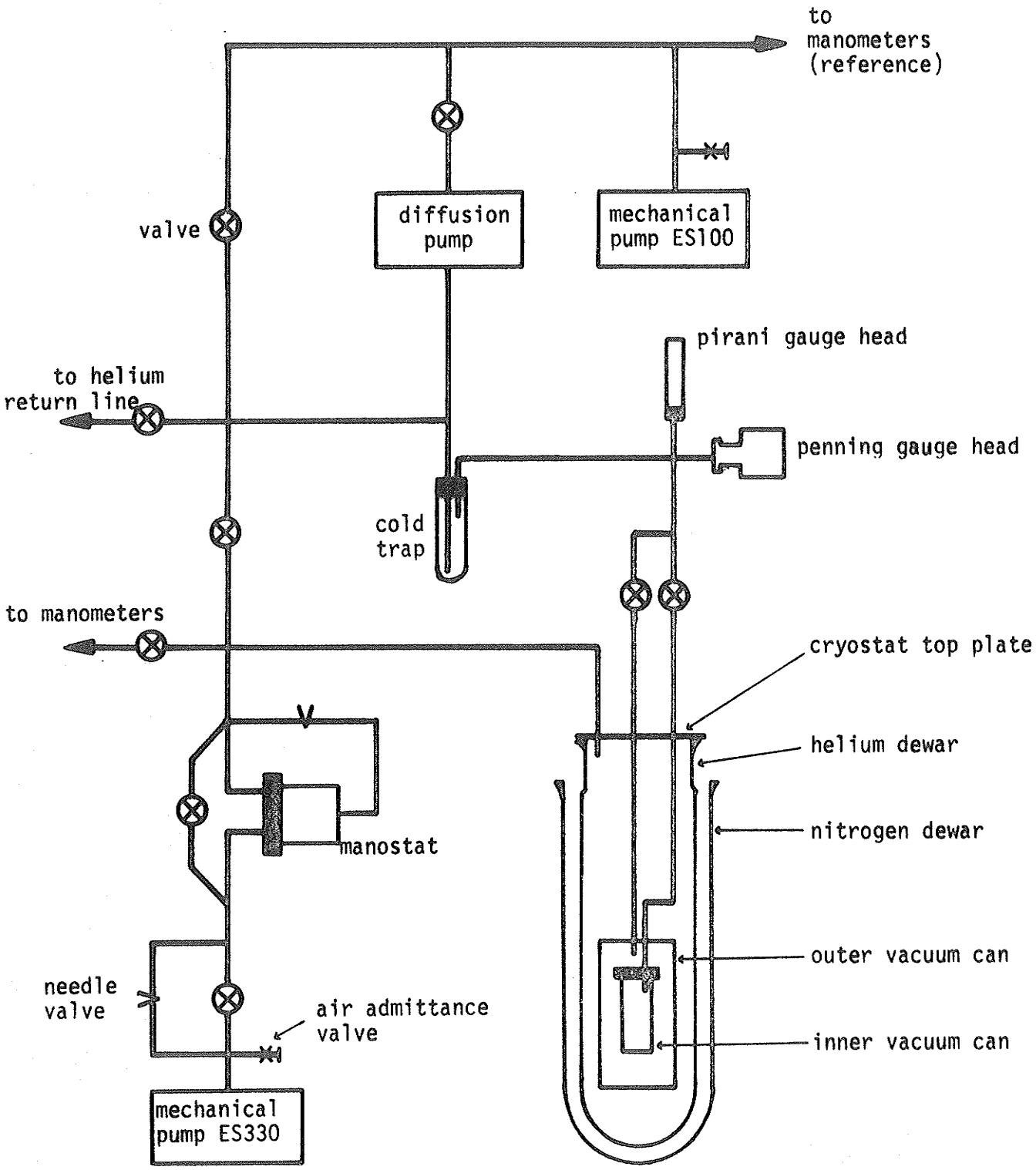

FIG. II-1. Block diagram of the vacuum system.

by a Speedivac ES100 mechanical pump, was used to control the pressure in the inner and outer vacuum cans, and to evacuate the reference side of the manometers. The pressure monitoring system was composed of a Pirani gauge for use in the range 760 down to 10^{-3} mm. Hg pressure, and a Penning gauge for pressure down to 10^{-7} mm. Hg.

The inner vacuum can (IVC) was machined from $2\frac{1}{2}$" diameter solid brass stock and was attached to the gas thermometer using 12 symmetrically located #2-32 bolts and an indium O-ring seal. Details of this construction are shown in Figure II-2. Two low thermal conductivity stainless steel tubes suspend the IVC from the top plate of the outer vacuum can (OVC). The OVC was soldered to the top plate with Wood's metal. Three stainless steel tubes, each about $2\frac{1}{2}$ feet long suspend this whole unit from the crystat top plate. One of these tubes serves as a guide for inserting the He^4 transfer tube when filling the dewar, one is a vacuum line to the OVC, and the third is a vacuum line to the IVC as well as a channel for the hook-up wires to the samples.

The hook-up wires consisted of twenty #29 enamelled copper wires bound in a Systoflex insulating sheath. These were connected to the various points on the mounting block (12 to voltage contacts, 2 current supply wires, 3 to the temperature sensing resistor, 2 for the heater coil, and 1 spare). The wires were routed through the stainless steel column to the cryostat top plate where connection was made to three pin-seals. Stycast epoxy cement provided a vacuum tight connection between the pin-seals and machined brass pin-seal mounts. More vivid detail of the top plate assembly is shown in Figure II-3.

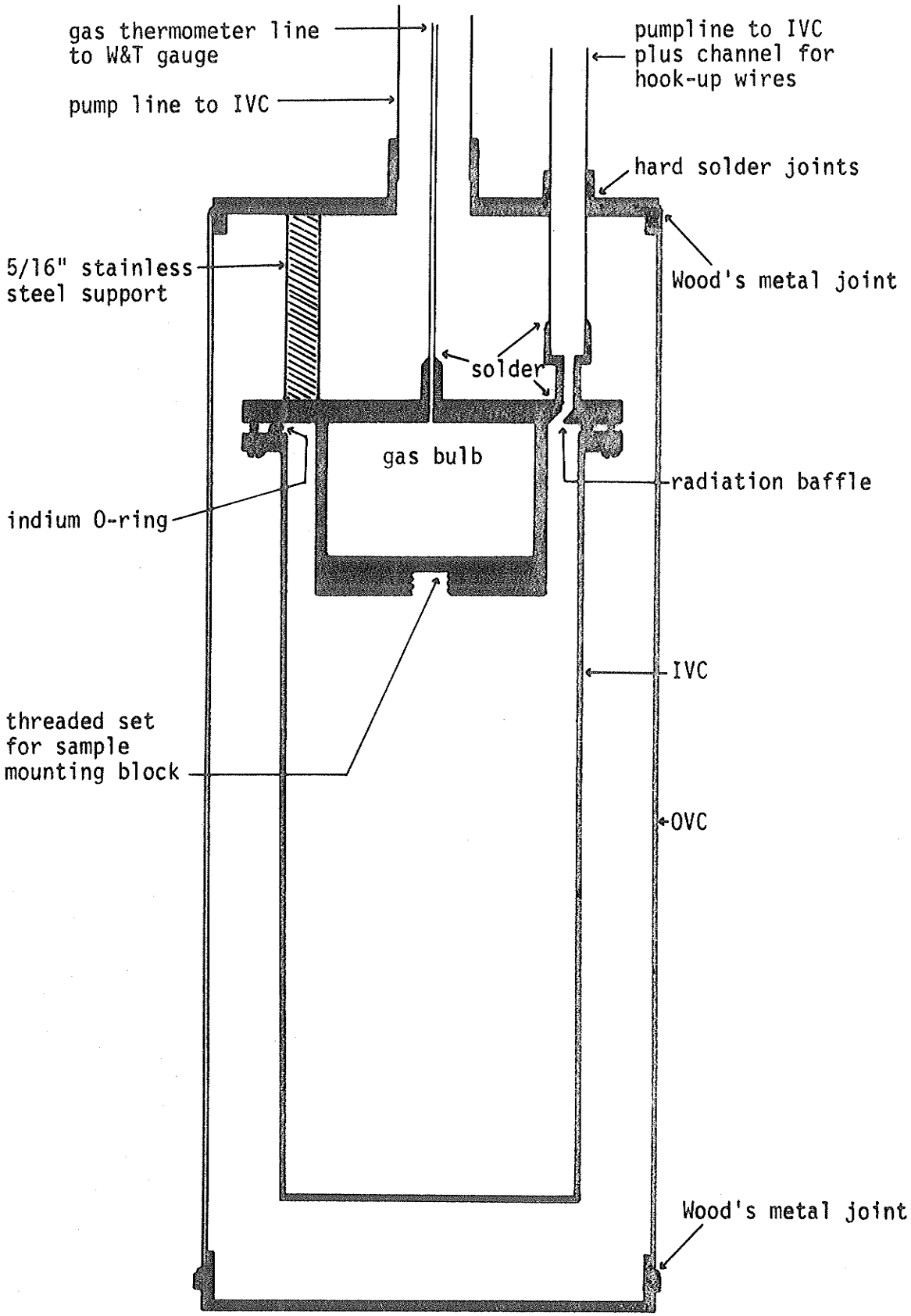

FIG. II-2. Details of the OVC, IVC and gas bulb.

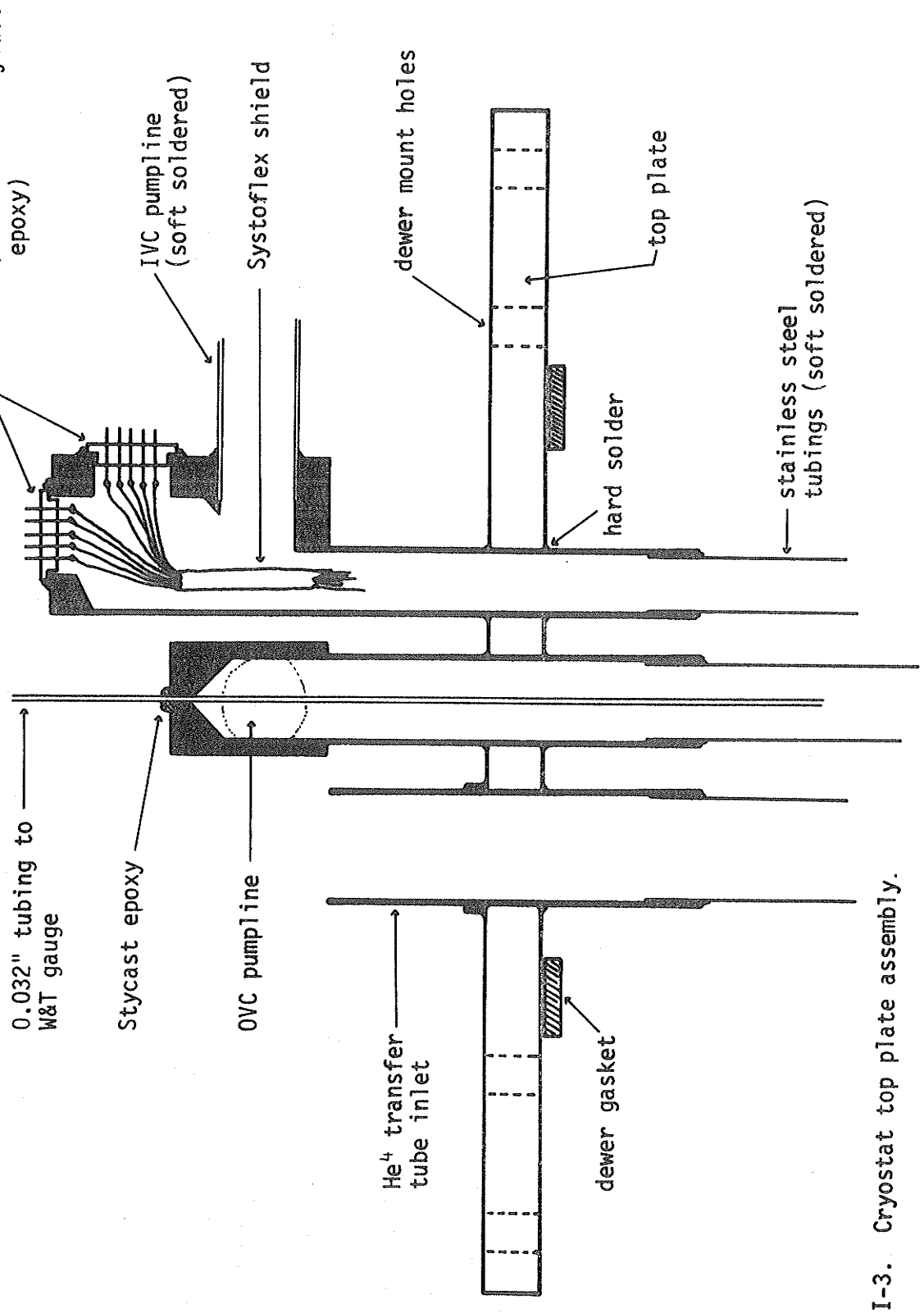

FIG. II-3. Cryostat top plate assembly.

II.3 The Sample Mount

The sample mounting block was machined from high thermal conductivity pure copper stock in approximately the proportions indicated in Figure II-4. The upper end of the block terminates in about a $\frac{1}{4}$" length of $\frac{1}{4}$" N.C. threads for fitting to the bottom of the gas thermometer bulb. Slots were machined in this block for the knife-edge sample supports and heaters, and a recessed groove was made in the center of one side for the temperature sensing resistor.

The block was designed to accept up to six samples, each of these to be mounted on a pair of knife-edge supports located near opposite ends of the block about 8 cm. apart. These supports were electrically insulated from the block with strips of condenser paper and generous amounts of General Electric (G.E.) No. 7031 varnish. The varnish contacts appear to be semiconducting, giving a room temperature resistance on the order of 10^4 ohms, but a significantly larger resistance ($>10^6$ ohms) below liquid nitrogen temperature. Reasonably good thermal contact is provided by the varnish.

Four #2-32 bolts, a Mylar insulating strip, and a thin brass yoke held the ends of the samples in good electrical and thermal contact with the knife-edge supports. Wires, soldered to the base of each knife-edge support, provided the voltage tap-off connections. The samples were series connected current-wise by soldering copper shunts between consecutive ends, and the end points of the series were connected to the current supply leads.

The second alloy system that was studied (RuMn) required an addition to the mount assembly. In this case, the production of samples long enough to span the existing supports proved very difficult owing to

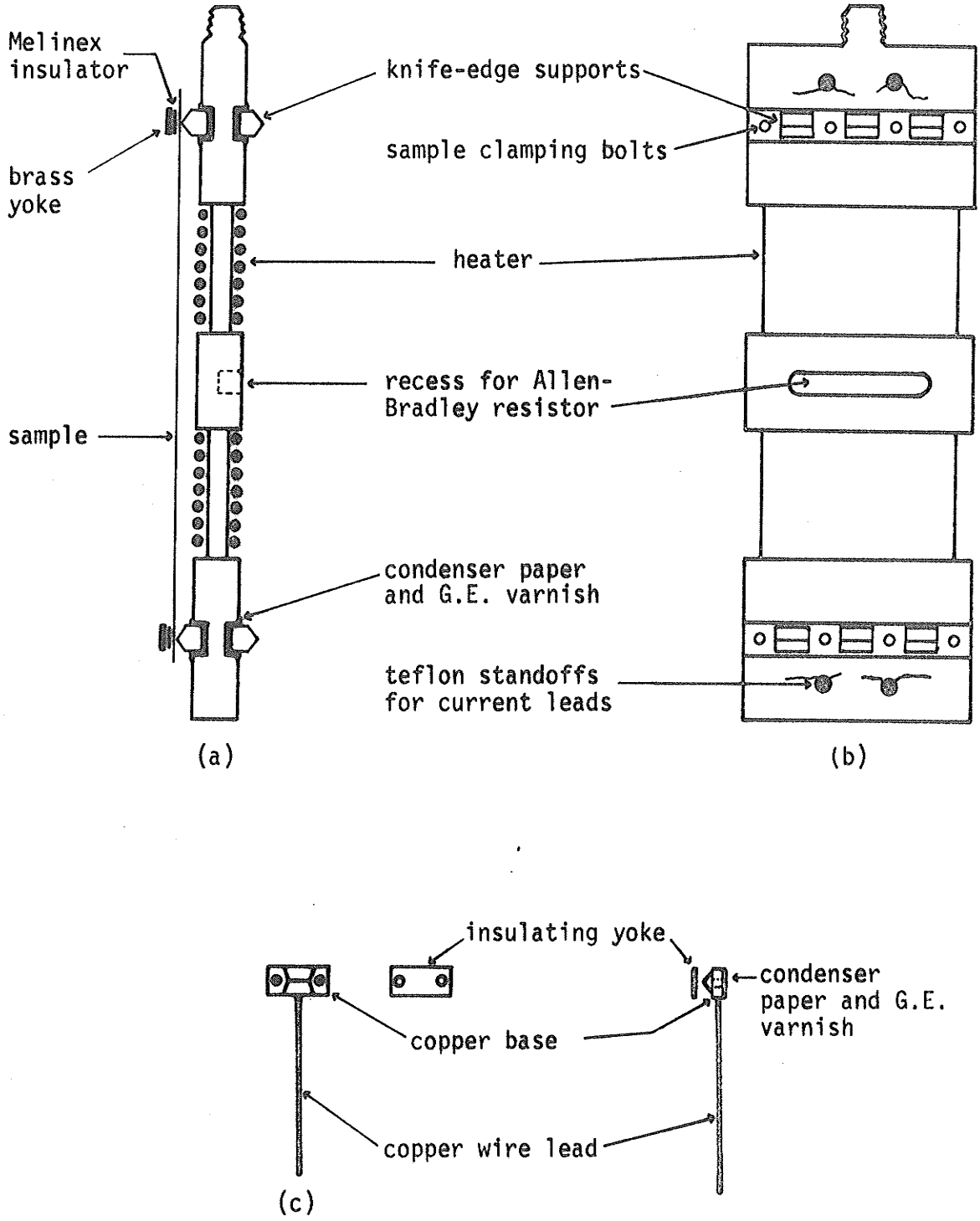

FIG. II-4. (a) Edge-view of mounting block.
(b) Face-view of mounting block.
(c) Face- and edge-views of "floating" knife-edge supports.

the brittle nature of the Ru alloys. To accommodate shorter samples without substantially altering the assembly, "floating" knife-edge supports were designed. These were very much like the original supports in shape, but each had its own insulating yoke held in place by two small bolts, and a heavy copper wire was soldered to the base of each one to effectively "extend" the length of the sample. (Refer to Figure II-4 for detail). When using these supports, one end of each sample was clamped in the regular manner on an upper support. A "floating" support was then attached to the lower end of the sample and the heavy copper wire routed over the fixed lower knife-edge where the wire was clamped in place allowing use of the existing voltage connections, and also providing good thermal contact to the block.

Two heater coils were wound around the copper specimen block, one for active use, the second as a standby. Each heater was formed from 20 feet of 0.036" diameter enamelled Cupron wire having a room temperature resistance of about 500 ohms. Since Cupron has a very low temperature coefficient of resistance this value changes little, even at low temperatures.

For temperature sensing an Allen-Bradley carbon resistor, 100 ohm nominal value, was fitted into the recessed groove in the center of the sample block. A tight fitting brass sleeve was used to assure good thermal contact. The temperature dependence of the resistance is roughly logarithmic, increasing with decreasing temperature, as observed in Figure II-5, and this calibration was used to select approximate temperature points. The actual temperatures were obtained more precisely by other means.

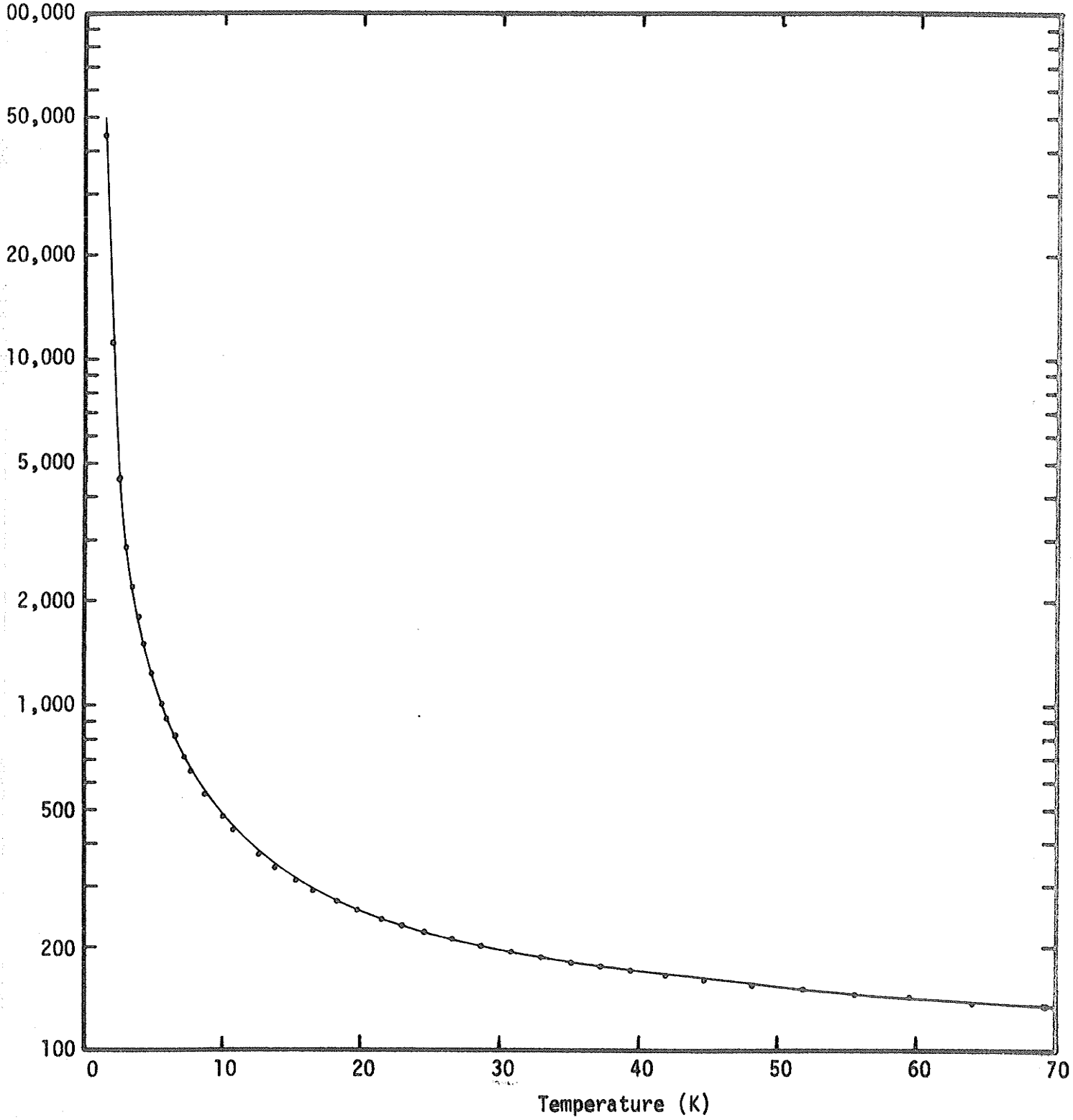

FIG. II-5. Resistance verses temperature characteristics of the Allen-Bradley Resistor.

II.4 Electronics

Two independent electronic systems were used with the apparatus, one system to provide a means of determining the resistance of the samples at a particular temperature, and the other to regulate the temperature.

Figure II-6 outlines in block diagram form the first of these systems. A current generator was used to supply a stable current to the series-connected samples. A Yew type 2745 low thermal (with gold plated

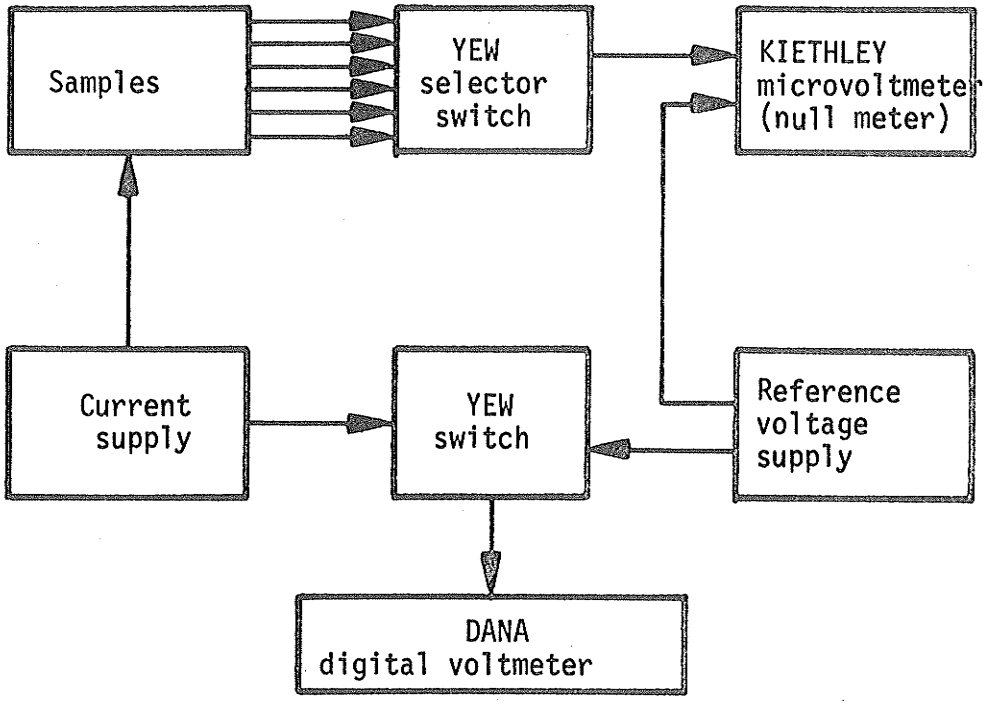

FIG. II-6. Block diagram of electronics.

contacts) 6-position selector switch applied the voltage drop from across a particular sample to a Kiethley 149 milli-microvoltmeter. The voltage drop was balanced with the output of a highly stable voltage generator using the Kiethley as a null detector. Balance could be obtained to about 2 parts in 10^9. In the balanced condition, voltage and current measurements were made on a $5\frac{1}{2}$ digit Dana model 5330 digital voltmeter

(DVM) with a resolution of about 1 part in 10^5. A second Yew switch selected the appropriate input to the DVM.

II.4.i Reference Voltage Supply

Mallory dry cells and a voltage divider network supplied an input potential to a Philbrick P85AU operational amplifier. The current drain from these cells was very low, about 70 μamps, assuring long life and stability. To eliminate the effect of thermal voltages a reversing switch (not shown) allowed selection of either input polarity.

The reference voltage was taken from a one ohm wire-wound standard resistor (Leeds and Northrup cannister type 29232, 0.01%). This voltage being very small (~0.01 to 1 millivolt), use was made of either a 1K or a 10K ohm Muirhead (± 0.02%) thermally stable standard resistor in series with the one ohm standard to generate a magnified voltage ($x10^3$ or $x10^4$, respectively) from which a voltage reading was taken. The actual sample voltage was then found by averaging the readings obtained from the DVM for the two input polarities, corrected by either 10^{-3} or 10^{-4}.

The operational amplifier, with highly stabilized gain obtained via strong negative feedback through the 1K (or 10K) resistor and a 5K Muirhead standard resistor, was the source of the reference voltage. The open loop gain of the operational amplifier being about 10^6 made the effective gain of the circuit just the feedback ratio, 0.2 (or 2), and since the ratio was determined by high-precision, high-stability resistors, the output was very stable. The breakdown diodes provided surge protection at the input to the operational amplifier.

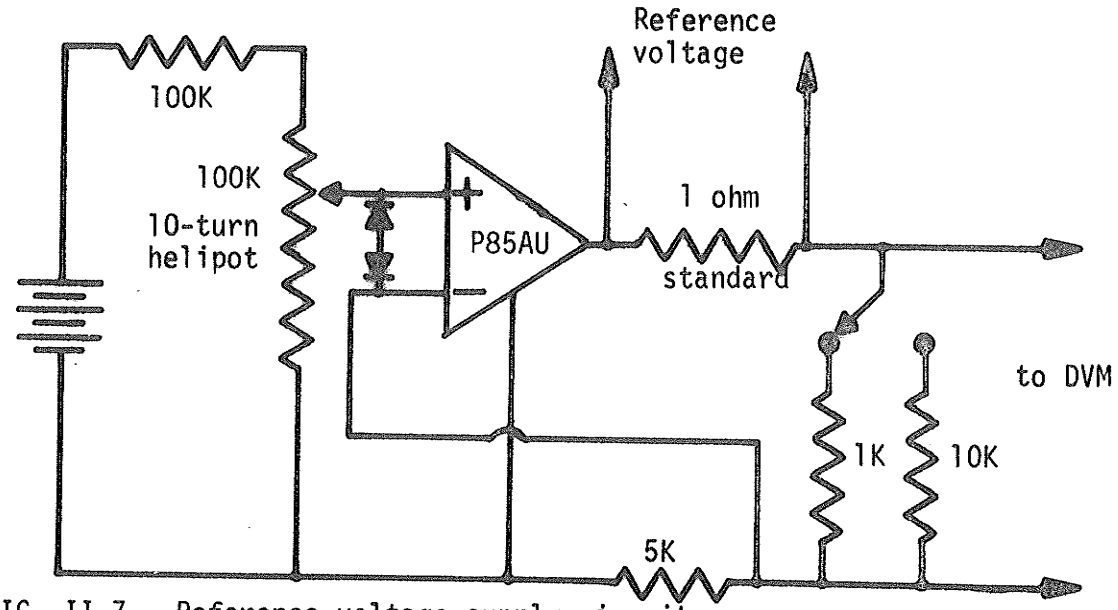

FIG. II-7. Reference voltage supply circuit.

II.4.ii Current Supply

A high stability sample current was maintained by regulating an OC36 transistor with a Philbrick P65AU operational amplifier. The gain of the operational amplifier circuit depends upon the feedback ratio. The transistor forms a link in the feedback loop so that any change in collector current was sensed by the operational amplifier. This signal, fed back with opposite polarity to the base of the OC36, restored the current level. The operating current was adjusted with the "adjust" resistor, which is detailed in Figure II-8.

Two automobile batteries connected in series formed the 24-volt current source. To determine the sample current, a 10 ohm Muirhead standard resistor was placed in series with the samples. The potential drop across the resistor was measured with the DVM and yielded 10xI, where I is the sample current. As with the voltages, the current through the samples could be reversed and an average value was used to cancel out the effect of any thermal voltages. The sample resistance readily followed from Ohm's Law and the voltage and current measurements. The V/I ratio for the specimens was found to be independent of current over the range used in the measurements.

II.4.iii Power Supply for Operational Amplifiers

Fifteen volt bipolar power supplies were required to operate the operational amplifiers. Separate zener regulated supplies were used for the reference voltage unit and the current supply unit to avoid grounding problems. A circuit diagram is given in Figure II-9. The power supply provided constant voltage output within ±1/3% with changes in load from 1K to 10K ohms, and within ±1/5% with line voltage variations of ±10%. It should be noted however that the operational amplifiers, due

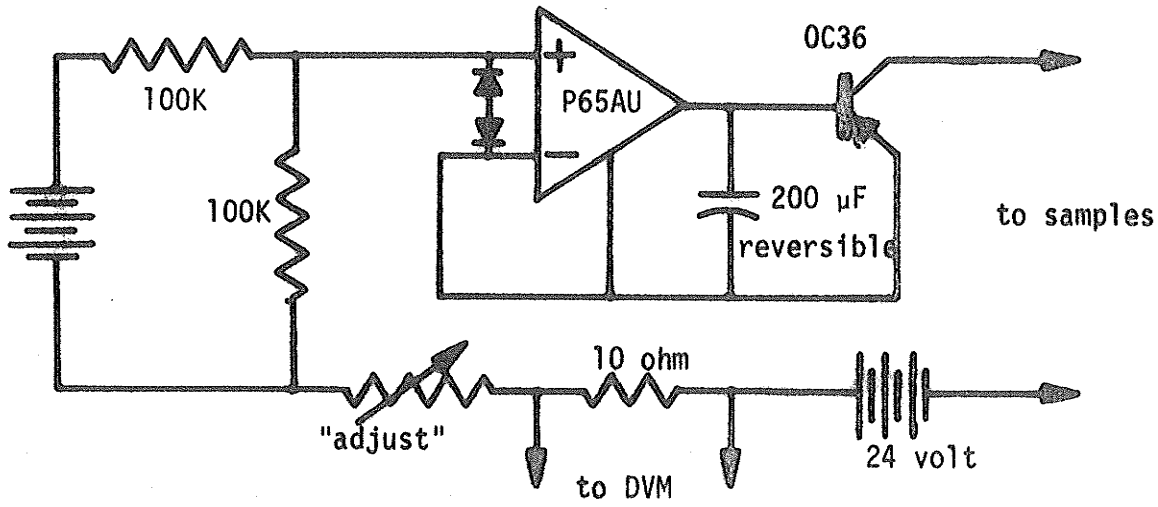

(a) Current supply circuit

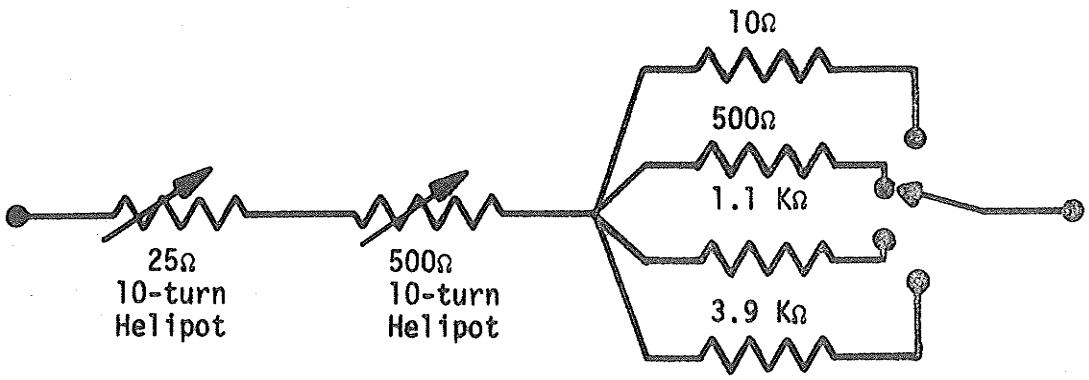

FIG. II-8. (b) Details of "adjust" resistor.

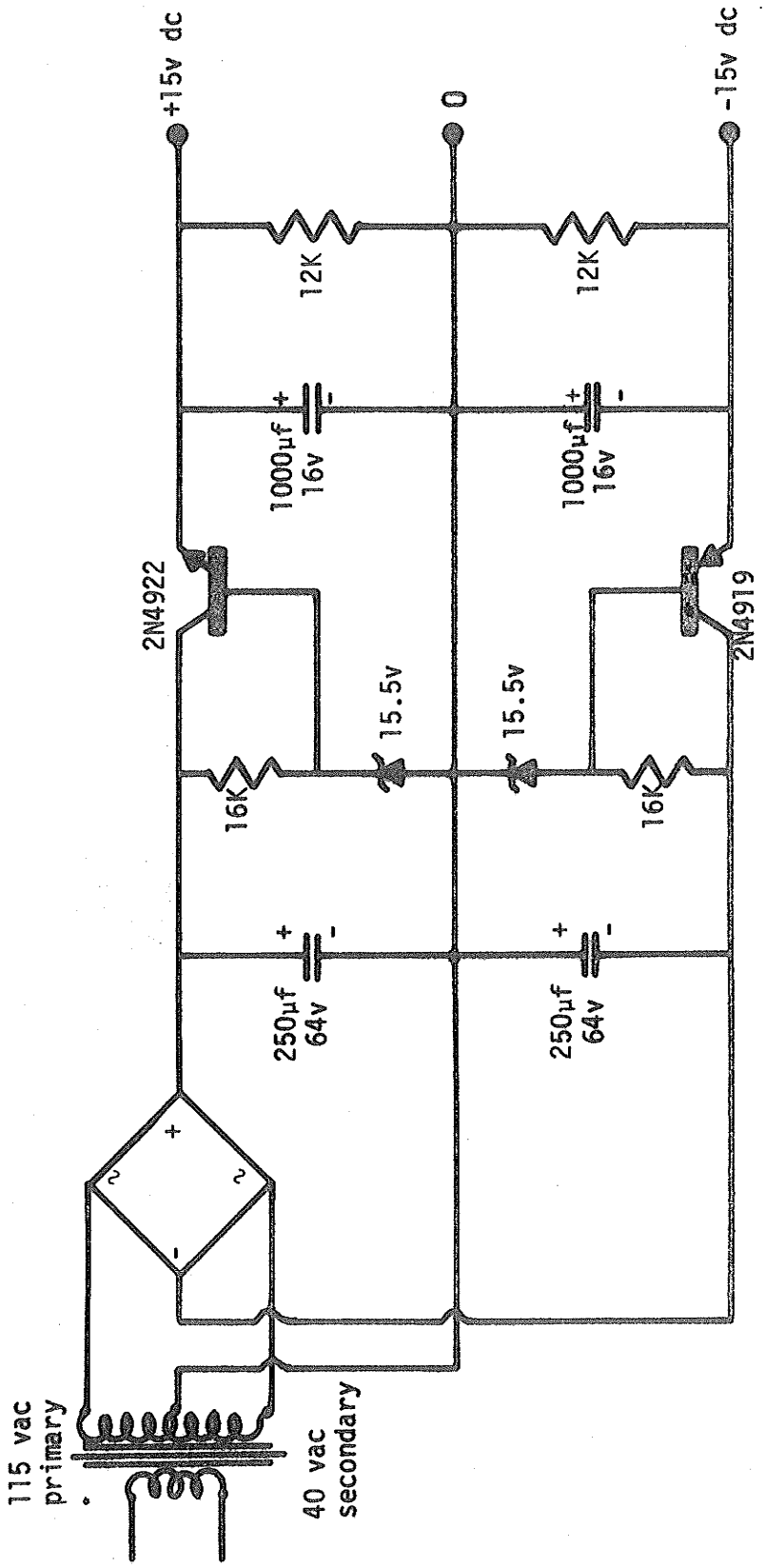

FIG. II-9. Circuit diagram of op amp power supply.

to their negative feedback arrangements were not affected by these changes to any detectible extent. In fact, the variation in the reference voltage supply output, for example, was less than 1 part in 10^5 with extreme line variations from 60 vac to 140 vac!

II.4.iv a-c Bridge Circuit

The second electronic system used was an a-c phase-sensitive Wheatstone Bridge for controlling the temperatures of the samples. The Allen-Bradley resistor in thermal contact with the mounting block formed one branch of the sensitive bridge circuit. A resistance box in another arm of the bridge (refer to Figure II-10) together with the temperature verses resistance curve (Figure II-5) for the Allen-Bradley

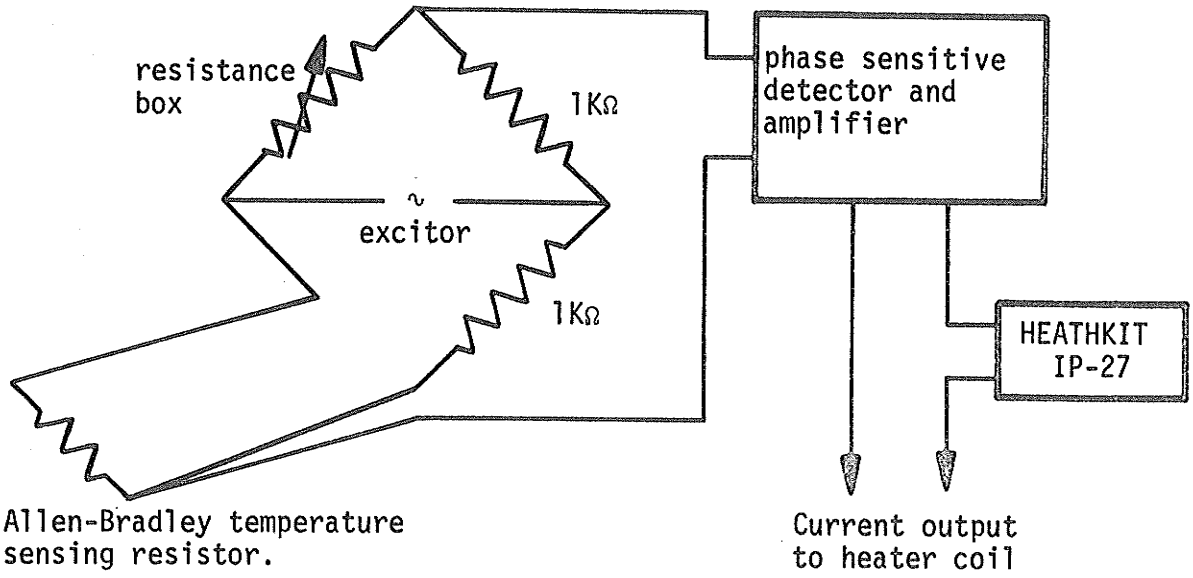

FIG. II-10. Bridge circuit. Note the three leads to the Allen-Bradley to balance the lead resistance.

resistor facilitated the "dialing" of an approximate temperature. A

phase sensitive detector supplied a d-c feedback current to the heater to achieve temperature regulation within 0.5%.

The feedback current from the bridge proved sufficient to obtain regulated temperatures to about 25K. Above this point a Heathkit IP-27 power supply was series-connected to the bridge output permitting temperatures beyond room temperature.

II.5 The Manostat

Figure II-11 illustrates the construction of the manostat which was a flexible membrane aneroid type[2]. It was used to achieve high temperature stability in the region below 4.2K by controlling the vapour pressure above the liquid helium bath. Pressure control was achieved via the motion of a latex rubber membrane responding to the differential between the bath pressure and the reference pressure in the reservoir. If the reference pressure exceeds that of the bath, the inlet is sealed and remains so until the differential is reversed at which time the membrane is forced back opening the inlet and allowing enough vapour to escape to restore the bath pressure to the reference level.

The reservoir was constructed from a machined brass cylinder which was hard-soldered to a solid disc at one end and to a perforated retaining plate at the other. This plate has 177 1/16" holes through it to permit fast response to small pressure differentials and protection against membrane rupture in case of large or sudden pressure changes. The inlet and outlet ports are similarly perforated to protect the membrane.

Other types of membrane material were tried without success. 1/16" gasket rubber proved insufficiently flexible, and Melinex, though

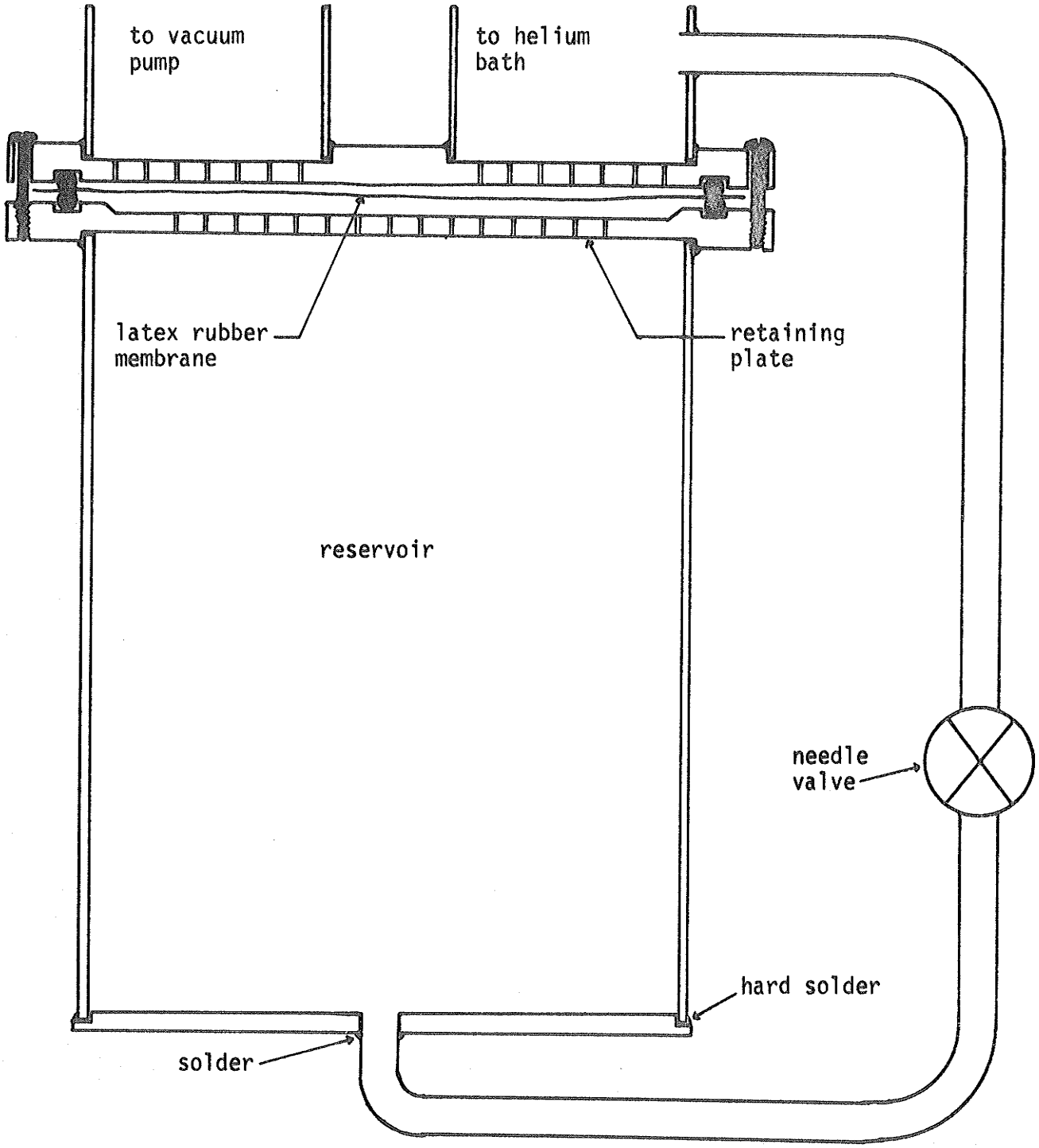

FIG. II-11. Manostat construction (drawn to sclae).

flexible, did not "seat" into the perforations well enough to prevent vapour flow. The thin (about 0.01") latex rubber sheet that was finally used proved excellent in both characteristics.

II.6 The Manometer System

Manometers connected to the helium bath (as illustrated in Figure II-12) were used to monitor the temperature of the samples below

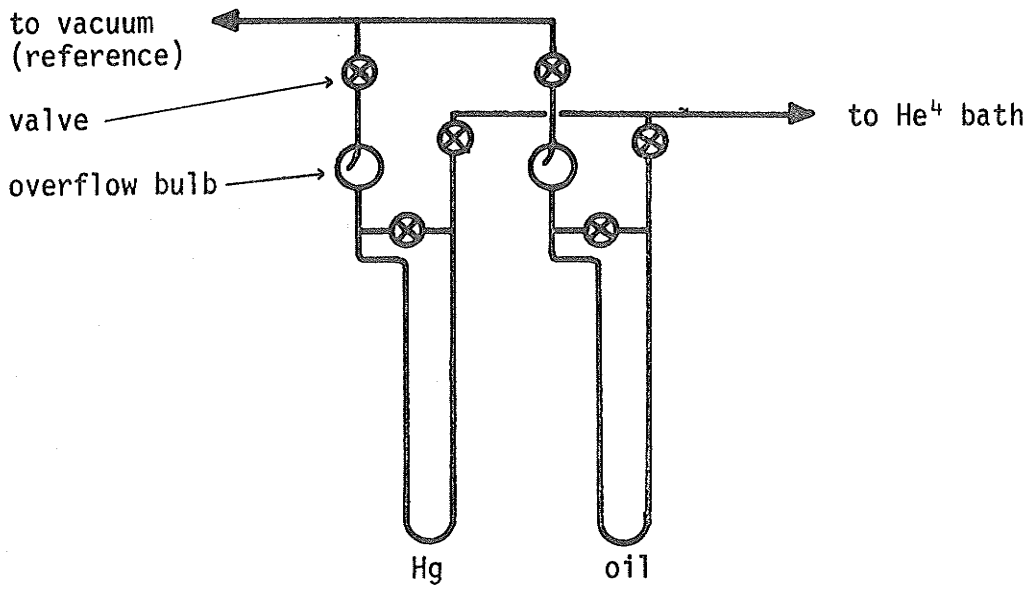

FIG. II-12. Manometer arrangement.

4.2K. The system, composed of two manometers, one with mercury for use in the range ≈ 3 to 85 cm. Hg pressure and one with oil for use below this range, measured temperatures to better than 5 millidegrees. Apiezon B low vapour pressure oil was used, and by comparison to mercury pressures in the 1 to 3 cm. Hg range, had a calculated density of 0.06350 times that of mercury. Temperatures corresponding to the measured pressures were determined from helium vapour pressure tables (Ref. 2, page 367).

II.7 The Gas Thermomemter

Temperatures above 4.2K were measured with a non-linear gas thermometer. This device is composed of a machined brass gas bulb, in thermal contact with the sample mounting block, connected to a series 1500 Wallace and Tiernan (W & T) pressure gauge via 0.032" O.D. stainless steel tubing. The tubing, of wall thickness 0.004", runs unbroken from the gas bulb to the W & T gauge, but is divided for discussions sake into two portions as shown in Figure II-13. L_1 (=28.7") is the length of tubing inside the cryostat, and L_2 (=109") is the portion outside which remains essentially at room temperature.

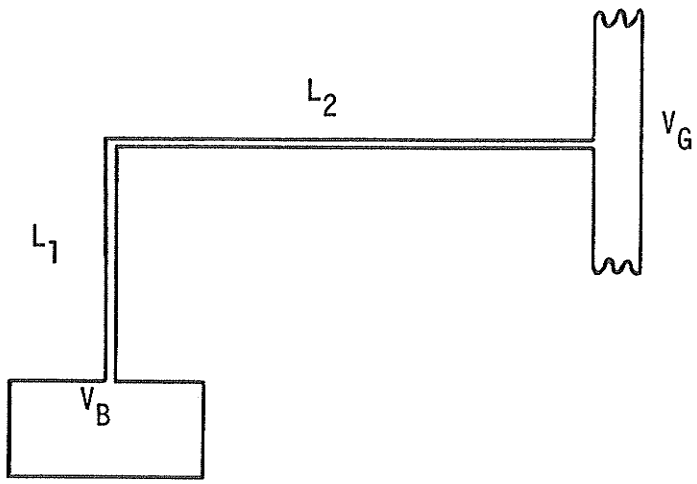

FIG. II-13. Schematic of gas thermometer.

The non-linearity of the gas thermometer is due mainly to the dead space volume comprised of the length L_2 of stainless steel tubing, gauge fittings, and the pressure-dependent internal volume of the gauge. Other contributions to non-linearity are the thermal gradient along L_1 between sample and room temperatures, thermal contraction of the gas bulb, and the non-ideality of the He^4 gas due mainly to Van der Waals type interatomic attractions.

The room temperature gas bulb volume, obtained from physical measurement of its dimensions, is 1.497 in.^{3}. Its volume at nitrogen temperature, computed using a table of thermal contractions (Ref. 2, page 377) would be 1.481 in.^{3} and at helium temperature 1.480 in.^{3}, illustrating that the thermal variance of the volume is essentially "frozen out" below 77K. The calculated volume of the cryostat tube, L_1, is V_{L1} = 0.0130 in.^{3} at room temperature, dropping only by 1% at 77K.

The internal dead space of the W & T gauge was assumed to vary linearily with pressure, thus giving for the total dead space volume of the gas thermometer, the expression,

$$V(P) = V_o + \alpha P \qquad \text{II.1}$$

where V_o is the pressure independent portion of the volume (actually $V_o = V_o(T)$, but room temperature variations were small and changes in V_o entirely negligible) and α is the gauge constant. V_o and α were computed by solving the gas law equation

$$\sum_i \frac{P_i \; V_i}{T_i} = \text{constant} \qquad \text{II.2}$$

for several sets of data obtained at the fixed points T_R (room temperature) and 77K. Averaged values from the above analysis gave V_o = 1.18 in.^{3} and α = 0.00115 in.^{3} per inch H_2O pressure.

Letting P be the measured pressure when the sample temperature is T, and assuming a linear temperature gradient from T to T_R along the cryostat tubing L_1, equation II.2 has the solution

$$P\left[\frac{V_B}{T} + \frac{V_{L1}}{T_R - T}\,\ell n\left(\frac{T_R}{T}\right) + \frac{V_o + \alpha P}{T_R}\right] = k. \qquad \text{II.3}$$

The constant k was evaluated by using the filling temperature and pressure, T_o (usually 4.2K) and P_o. The thermal contraction of the gas bulb was accounted for using this first estimate of T, then an improved temperature value was obtained by repeating the calculation. Further correction was made in light of the non-ideality of the helium gas using interpolations from a set of Virial Coefficients[3]. A computer was employed to do these rather tedious calculations.

Figure II-14 illustrates the variation from linearily for the case T_o = 4.2K and P_o = 4.2.

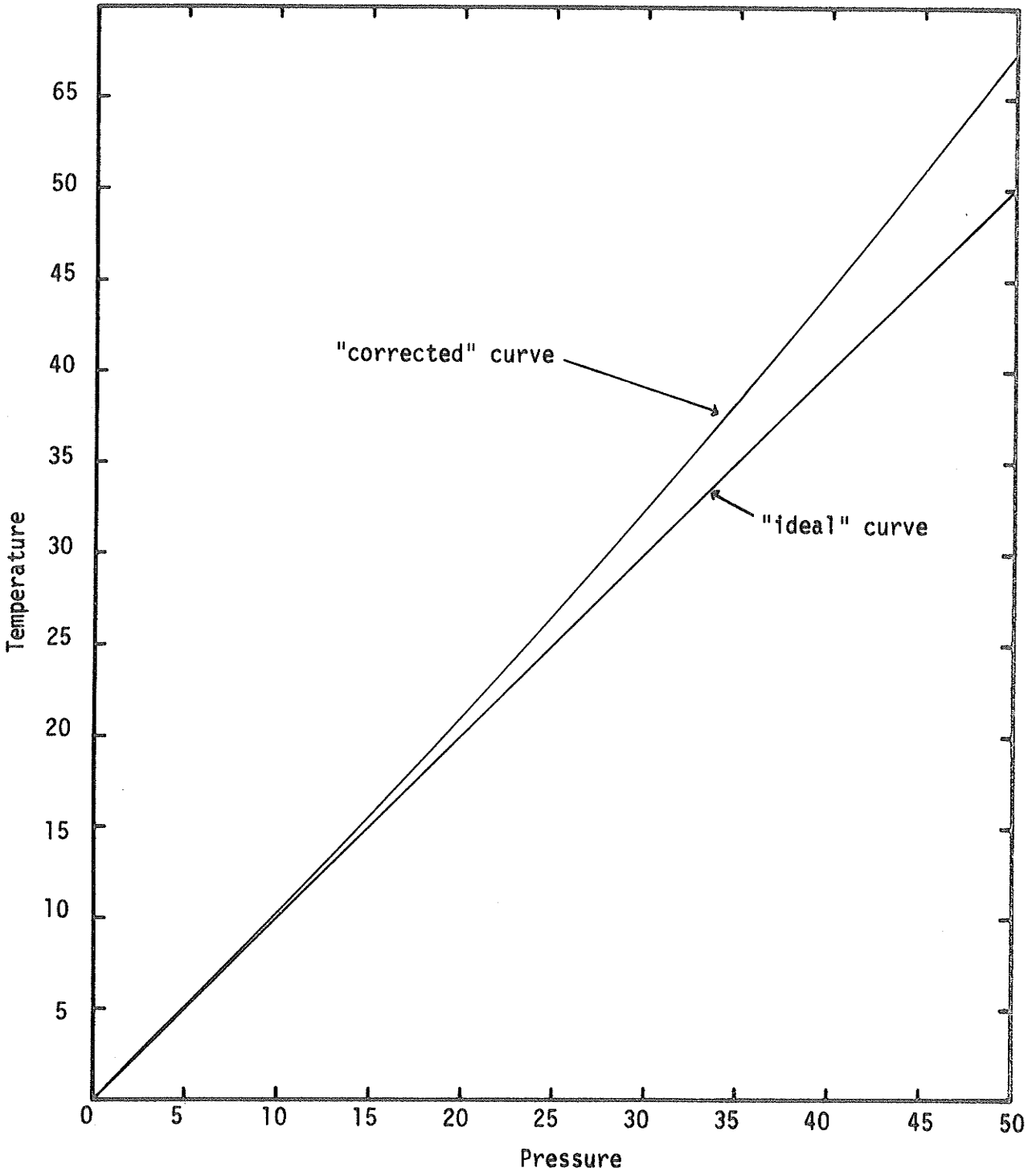

FIG. II-14. Illustration of the non-linearity of the gas thermometer for the case T_o = 4.2K, P_o = 4.2.

References

1. A.D.C. Grassie, G.A. Swallow, Gwyn Williams, and J.W. Loram, Phys. Rev. B3, 4154 (1971).

2. G.K. White, "Experimental Techniques in Low Temperature Physics", Second edition, Oxford Press, 1968, page 244.

3. W.H. Keesom, "Helium", Elsevier, Amsterdam, 1942.

CHAPTER THREE

PALLADIUM COBALT

III.1 Introduction

Considerable study has recently been made of the ferromagnetic phase of dilute transition-metal alloys, typified by the giant moment systems of PdFe and PdCo. Veal and Rayne[1] have shown for $T<<T_c$ that PdFe gives a $T^{3/2}$ contribution to specific heat and Wheeler[2] has shown that a similar behaviour exists for PdCo. The $T^{3/2}$ behaviour can be attributed to energetically low-lying spin-wave-like excitations, or magnons, from an ordered ground state. Magnetization measurements[3,4] also show a $T^{3/2}$ contribution to magnetism in the low temperature range.

Theoretically these results are explicable on the basis of an "s-d" model[5,6] which describes the exchange coupling between localized impurity moments and exchange enhanced d-band electrons of the host. Resistivity calculations were made by Long and Turner[7] on this ferromagnetic system, approximated at low temperatures by spin waves, using a model in which s electrons are scattered from these excitations. The impurity spins are assumed to be randomly distributed throughout the alloy and thus assuming the absence of translational invariance, or equivalently, the nonconservation of wave-vector, Long and Turner were led to a $T^{3/2}$ limiting behaviour for the incremental resistivity $\Delta\rho(T) = \rho_{alloy}(T) - \rho_{metal}(T)$. This prediction has been borne out by resistivity measurements on dilute PdFe[8] (<1 at. % Fe), PdCo[9] ($\leq$1 at. % Co) and PdMn[10,11] (<3 at. % Mn).

If wave-vector conservation is assumed to hold[12], the electron-magnon scattering theory then predicts a T^2 limiting form for $\Delta\rho(T)$, $T<<T_c$. Skalski et al.[13] observed this type of behaviour in PdFe ($\geq$2 at. % Fe) well below the Curie temperature, and a depen-

dence between $T^{3/2}$ and T^2 for Pd-1 at. % Fe.

In the present work, the temperature dependence of resistivity of relatively concentrated PdCo alloys (in the range from 2 to 7.5 at. % Co) was investigated over a temperature range from 1.4K to 77K. Schwaller and Wucher[14] had previously looked at PdCo for alloys with > 2 at. % Co, but confined their measurements to the fixed points 4.2K and 20.3K in the low temperature region, and were thus unable to establish the low temperature limiting form for incremental resistivity.

III.2 Sample Preparation

The samples were prepared from 99.999% pure Pd wire (obtained from Johnson Matthey, London) and 99.998% pure Co sheet (from Metals Research, Cambridge, U.K.). Samples of approximately 5 grams were made by melting together appropriate proportions of the pure elements on the water-cooled copper hearth of an argon arc furnace. Each alloy was inverted and remelted five times to ensure homogeneity. Melting losses were negligibly small. These samples were cold rolled to thicknesses of about 1.5×10^{-2} cm. between sheets of Melinex to prevent the transfer of impurities from the rollers to the alloys. Long, narrow specimens (about 10 cm. × 0.3 cm.) were cut from these sheets. Six specimens were prepared, one pure Pd, and 5 alloys with 2, 3, 4, 5 and 7.5 at. % Co, respectively, which were etched in dilute nitric acid containing a few drops of H_2O_2 for about 5 minutes, and then washed in distilled water. The samples were annealed *in vacuo* for about 30 hours.

The form factors (area to length ratios) were determined using a method described by Loram, Whall and Ford[15]. The knife-edge sample supports (potential contacts) leave impressions on the samples and the distance between these marks can be accurately measured with a travelling microscope. The density of each sample is determined from lattice spacing data, using the formula

$$\text{Density} = \frac{4}{Na^3}(A_1x_1 + A_2x_2) \qquad \text{III.1}$$

where N is Avogadro's number, A_1 and A_2 are the atomic weights of the elements used, x_1 and x_2 being their respective fractional atomic compositions, and the factor 4 indicates that there are four atoms per unit cell in the fcc palladium. The "a" is the concentration dependent lattice constant of the alloy. Bozorth et al.[16] show that in the concentration range under study that Vegard's Law[17] is applicable, so the lattice constants are obtained from the law in conjunction with the lattice spacings[17] of pure Pd (3.8907 Å) and pure Co (3.544 Å).

From the density and an accurate measurement of the weight, the volume of the sample is determined. The travelling microscope is again employed to find the total length of the specimen which, with the volume, readily yields the average cross-sectional area. Keeping the portions of the specimen which overhang the knife-edge as short as possible minimizes error in the mean area of the section between the knife-edges. The ratio of the cross-sectional area to the inter-knife-edge spacing yields the required form factor for the specimen.

Table III-1 lists the computed lattice constants and form factors for the PdCo system used.

TABLE III-1

Lattice Constants and Form Factors of the PdCo Alloy System

Co Concentration (at. %)	Lattice Constant ($\AA$)	Form Factor (10^{-4} cm.)
Pure Pd	3.8907	3.3078
2	3.8735	3.1554
3	3.8706	4.6741
4	3.8672	4.6464
5	3.8639	3.4110
7.5	3.8554	4.3877

III.3 Data Collection

A single data "point" required the recording of eighteen current and voltage values plus two or more temperature values.

An appropriate reference voltage was first selected. An appropriate value is one that allows all of the samples to be readily balanced against the reference voltage, and the values of this reference are recorded for both polarities. The current through a particular sample, the sample being selected with the Yew switch, was then adjusted so that the potential across the sample balanced the reference potential (observed as a null on the Kiethley milli-microvoltmeter). The value of the current was then deduced by measuring the voltage drop across a 10 ohm resistor in series with the sample; the current direction was reversed and the measurement repeated. Current values for all specimens were similarly obtained. The voltage reference measurements were repeated in the middle and at the end of set of the current measurements giving a set of six readings to be averaged.

For temperatures below 4.2K, the difference in Hg or oil levels (depending upon the He^4 vapour pressure range) in the monometer was measured with a cathetometer to within about ±0.005 cm. This difference measurement was repeated two or three times while the current and voltage measurements were being made to assure minimal drift. If the drift was significant (>0.1%), the point was repeated after allowing more time for temperature stabilization.

Above 4.2K, gas pressure readings were taken directly from the He^4 gas thermometer (read from W & T gauge), again with readings repeated a few times to assure minimal drift at each point.

Computor programmes were written to do the calculations. Appendix A contains samples of the programmes used.

III.4 Results and Discussion

The incremental resistivity is defined by

$$\Delta\rho(T) = \rho_{alloy}(T) - \rho_{metal}(T). \qquad \text{III.2}$$

Figures III-1 and III-2 show the incremental resistivities of the five alloys plotted against temperature in the range 1.4K to 77K. The nominal concentrations are also indicated in these figures. The data of Schwaller and Wucher[14] suggests that the Curie temperature for each alloy was above 77K, the highest temperature used in this investigation. A non-linear variation of $\Delta\rho(T)$ with temperature is clearly evident from Figures III-1 and III-2, and following Skalski et al., $\Delta\rho(T)$ is plotted against T^2. Figure III-3 illustrates that $\Delta\rho(T) \propto T$ holds for $T < 35K$, with the region of validity extending to higher temperatures as the concentration, and thus the Curie temperature, becomes larger. This figure allows estimates of $\Delta\rho(T = 0)$ and of the coefficient of the T^2

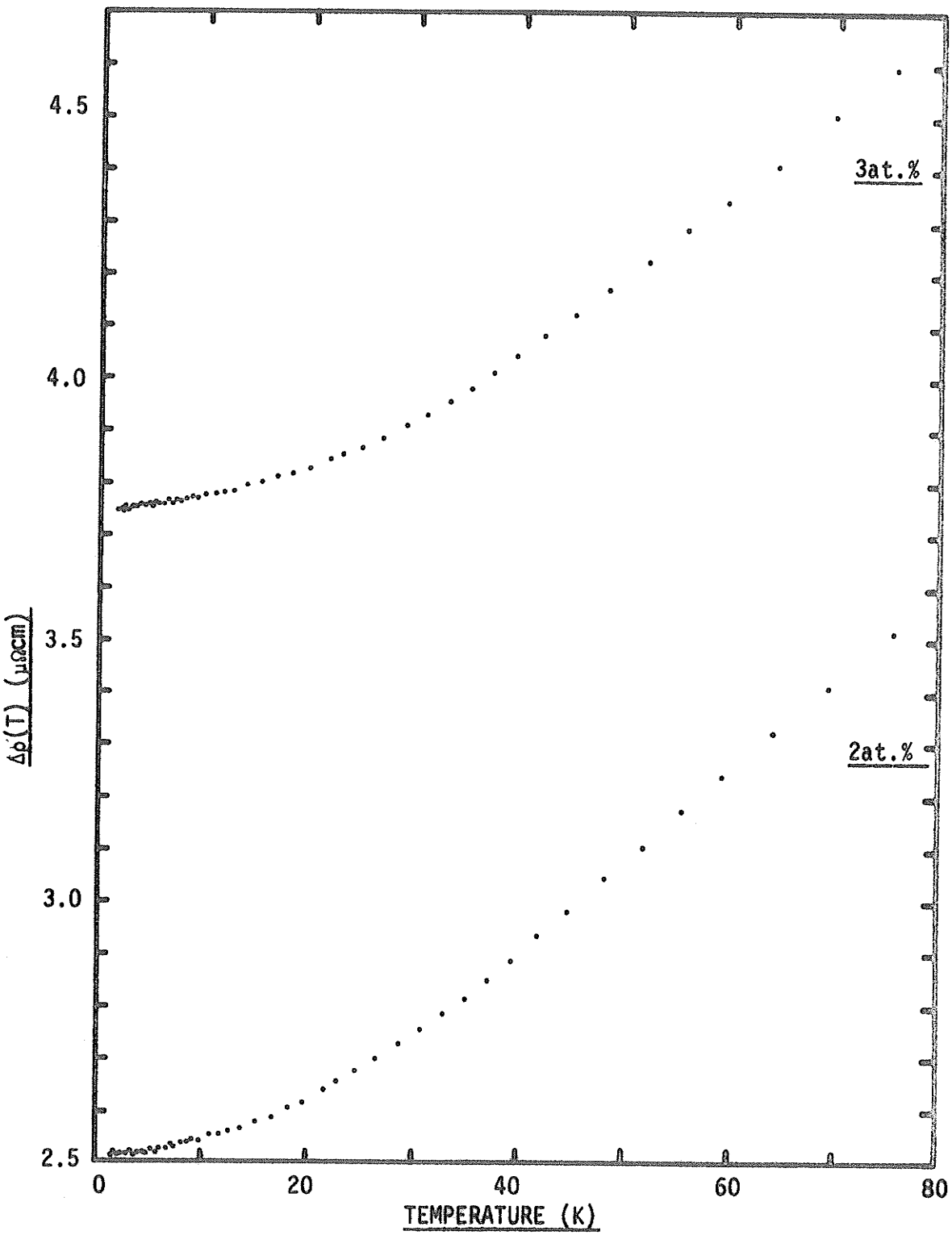

FIG. III-1. The incremental resistivity $\Delta\rho(T) = \rho_{alloy}(T) - \rho_{metal}(T)$ (in μΩcm) for the Pd-2at.% Co and Pd-3at.% Co alloys, plotted against temperature (in K).

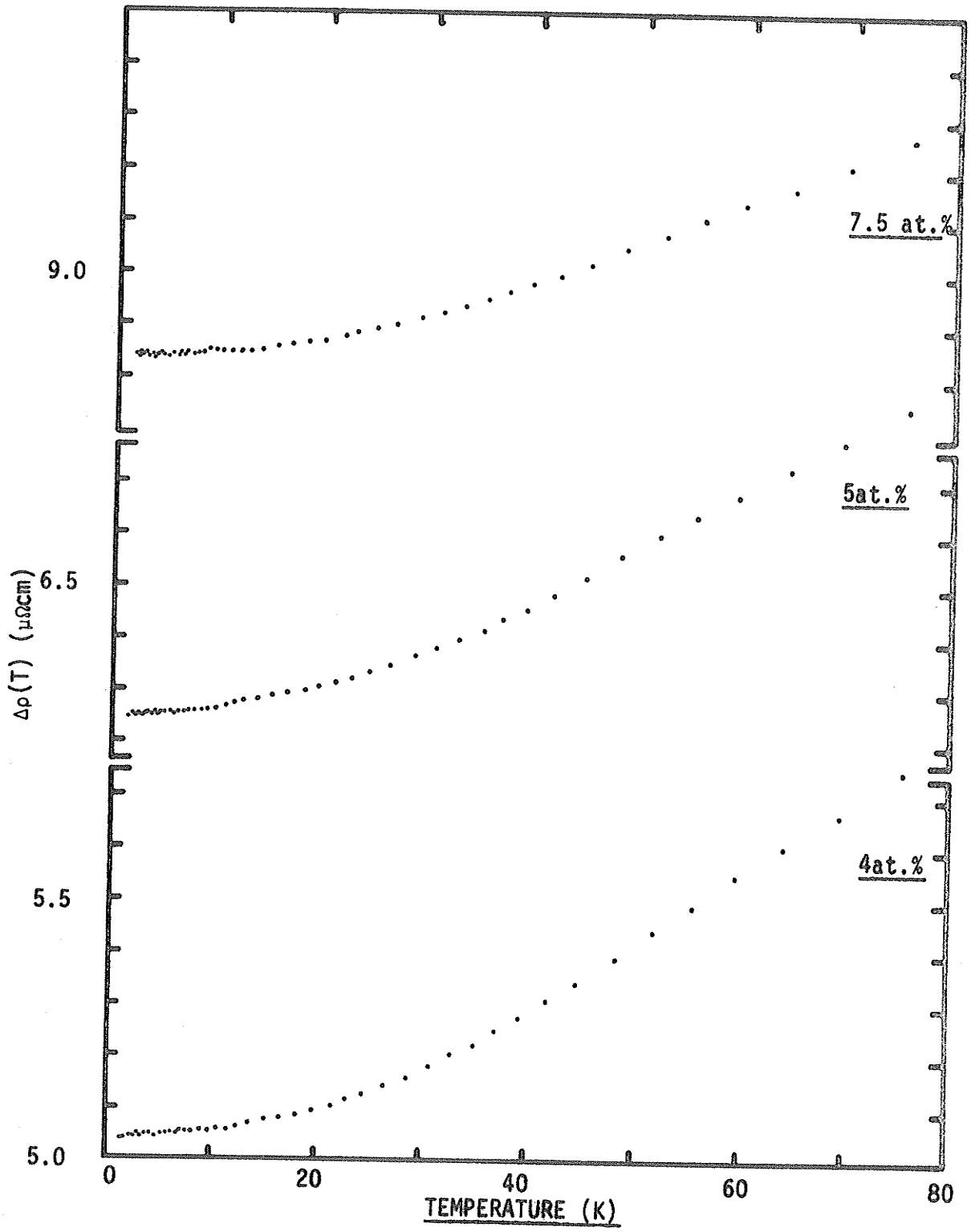

FIG. III-2. Incremental resistivity $\Delta\rho(T)$ (in $\mu\Omega$cm) for Pd-4at.% Co, Pd-5at.% Co and Pd-7.5at.% Co alloys, plotted against temperature (in K). Note the shift in scale.

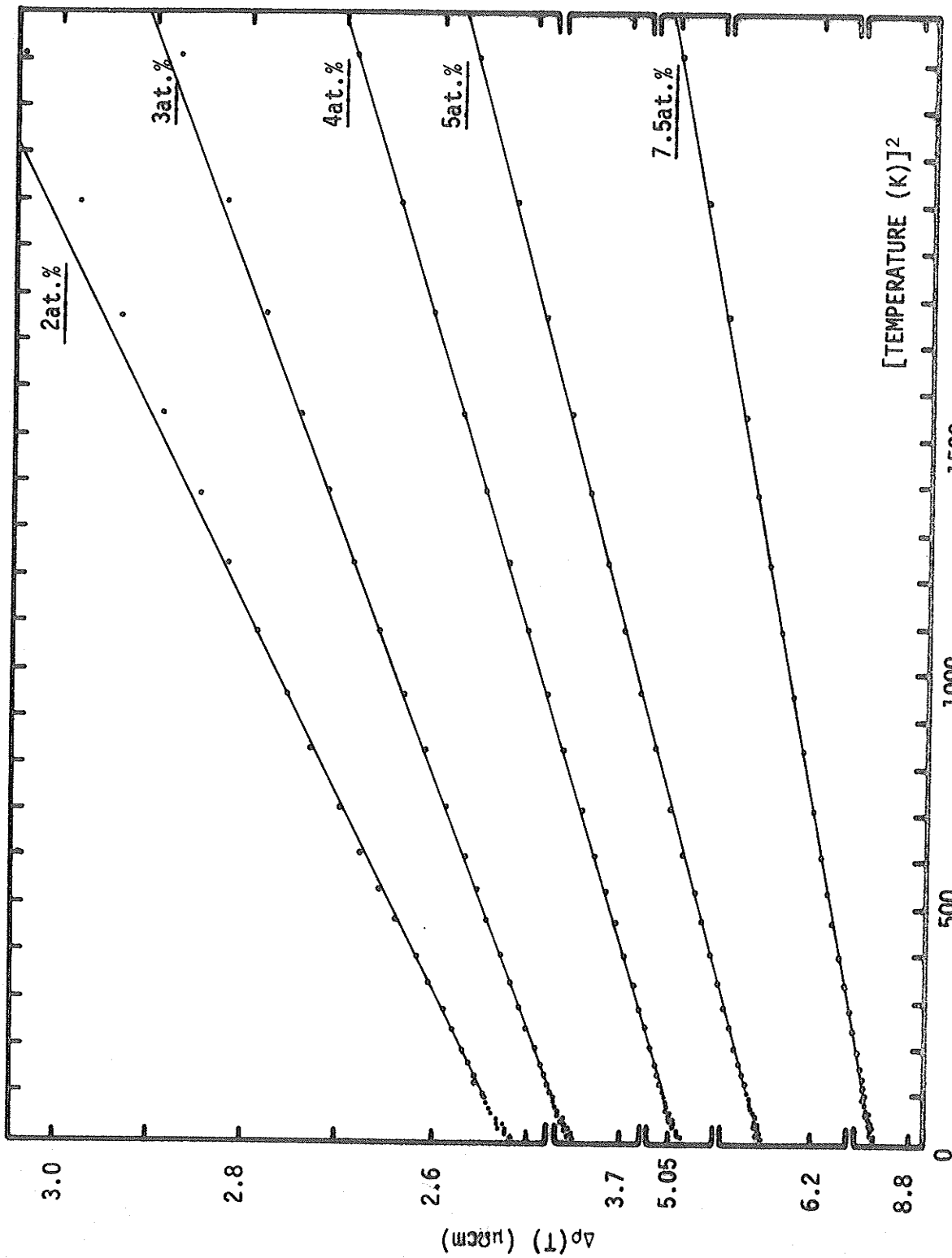

FIG. III-3. Incremental resistivity $\Delta\rho(T)$ (in $\mu\Omega$cm) plotted against the square of the temperature T(K) for the five alloys examined. The vertical scale for each alloy is the same, although the zero has been changed.

term to be made. These are given in Table III-2.

TABLE III-2

Summary of Estimates on PdCo Alloys

Co Concentration (at. %)	$\Delta\rho(T = 0)$ ($\mu\Omega$cm.)	Coefficient of T^2 term (10^{-4} $\mu\Omega$cm./K^2)
2	2.521 ± 0.003	2.46 ± 0.02
3	3.754 ± 0.003	1.89 ± 0.02
4	5.041 ± 0.003	1.51 ± 0.02
5	6.253 ± 0.003	1.35 ± 0.02
7.5	8.839 ± 0.003	0.93 ± 0.02

The value of $\Delta\rho(T = 0)$ increases with concentration. Figure III-4, which is a plot of $\Delta\rho(T = 0)$ verses concentration shows that $\Delta\rho(T = 0)$ has the form

$$\Delta\rho(T = 0) = Ac \qquad \text{III.3}$$

where A = 1.27 ± 0.03 $\mu\Omega$cm/at.% Co. This value of A is in excellent agreement with that obtained by Schwaller and Wucher[14] (A = 1.27) in the same concentration range and close to the value obtained by Williams[9] (A = 1.40 ± 0.04) for more dilute PdCo alloys. This agreement and the fact that melting losses were negligible leads to the direct use of the nominal concentrations in the subsequent analysis.

Figure III-3 suggests that the T^2-coefficient decreases with concentration of Co. A log-log plot of the numerical values of the T^2-coefficients (Table III-2) verses the concentration is made in Figure III-5 to determine the exact concentration dependence, and the result is reasonably well described by

$$T^2\text{-coefficient} \propto c^n \qquad \text{III.4}$$

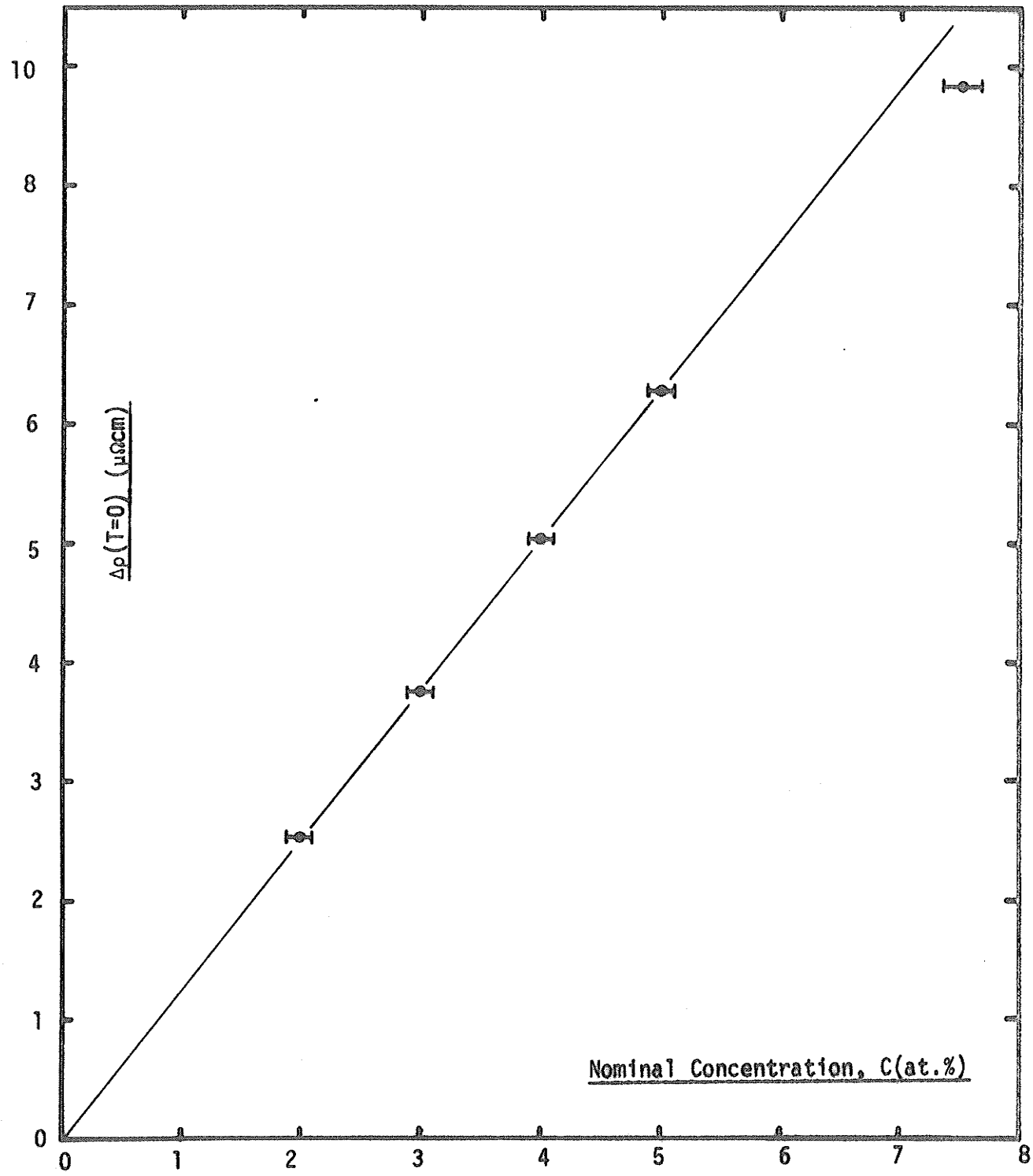

FIG. III-4. The incremental resistivity at zero temperature $\Delta\rho(T=0)$ (in $\mu\Omega$cm) estimated from Figure III-3, plotted against the nominal impurity concentration (in at.%). The line drawn has a slope of 1.27 $\mu\Omega$cm/at.% Co.

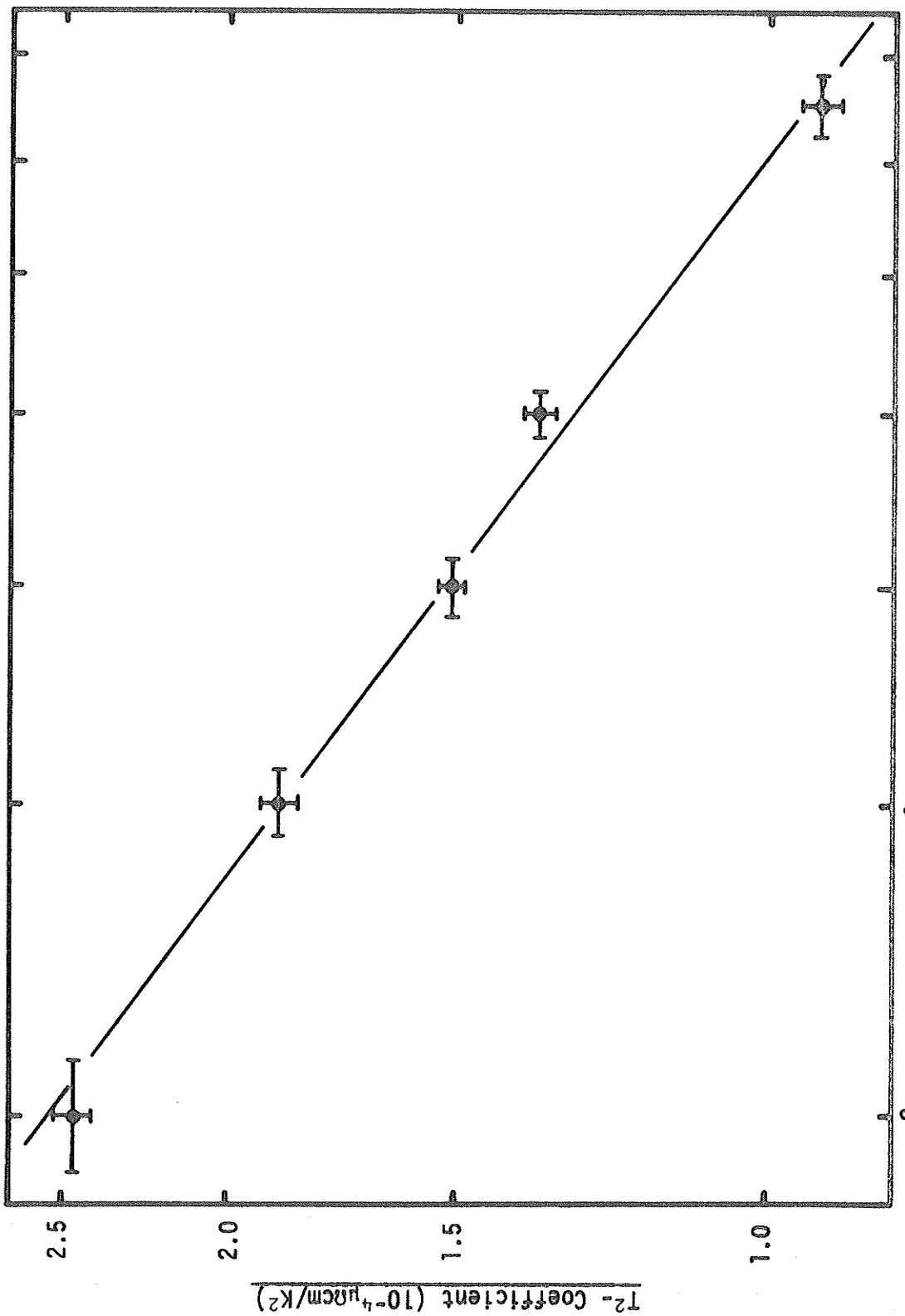

FIG. III-5. The coefficient of T^2 term (in $\mu\Omega cm/K^2$) obtained from Figure III-3, plotted against the impurity concentration (in at.%) on a logarithmic scale. The line drawn has a slope of -0.75.

where n = - 0.75 ± 0.05. This contrasts with PdFe[13] in the comparable concentration range where the coefficient increases with increasing concentration. In palladium alloys with concentrations less than 1 at. %, where a $T^{3/2}$ limiting form of incremental resistivity exists, the $T^{3/2}$-coefficient decreases with increasing concentration for both Co[9] and Fe[8], as it does for the T^2- coefficient in this study.

At the present time there seems to be no a priori means of predicing when wave-vector conservation holds; one can only resort to experiment. It seems that in both PdFe and PdCo systems this transistion from a $T^{3/2}$ (non-conservation) to a T^2 (conservation) dependence occurs for an impurity concentration of about 2 at. %. Skalski et al. note that a good deal of homogenity is shown for the d-band polarization for concentrations greater than 2 at. %. Having experimentally established the T^2 dependence of incremental resistivity well below the Curie temperature, the nonconservation (of wave-vector) analysis of Long and Turner[7] must be rejected, and reference is made to the conservation analysis which is discussed in section I.9.

III.4.i Calculation of |V|

A consideration of s electron scattering from collective excitations in the low temperature region led to Equation I.23 for incremental resistivity. The temperature independent term is

$$\frac{3\pi m^* c}{2e^2\hbar N\varepsilon_F}\,|V|^2 \qquad \text{III.5}$$

where m* is the effective mass of conduction electrons, c is the concentration factor, N the number of lattice sites per unit volume, ε_F the Fermi energy, and |V| is the "potential exchange integral".

ε_F is computed from an effective mass approximation[18] of the s-band in Pd. This assumes a free electron gas with a parabolic density of states (refer to Figure III-6).

$$n(\varepsilon) = \frac{V_a}{2\pi^2}\left(\frac{2m^*}{\hbar^2}\right)^{3/2}\varepsilon^{1/2} \qquad \text{III.6}$$

where V_a is the volume occupied per atom in Pd. Integrating up to ε_F gives the total electron population of the s-band

$$P(\varepsilon) = \frac{V_a}{3\pi^2}\left(\frac{2m^*}{\hbar^2}\right)^{3/2}\varepsilon_F^{3/2} \qquad \text{III.7}$$

Using $m^* = 2.3\ m_o$[19] and $P(\varepsilon) = 0.36$[20], the value of ε_F is 1.33 eV, and

$$\frac{3\pi m^* c}{2e^2\hbar N\varepsilon_F} = 6.49\ c'\ \frac{\mu\Omega cm}{(eV)^2\text{-at.\%Co}}$$

with c' being the nominal concentration of Co in at. %. Recalling the value of A (= 1.27 μΩcm./at.% Co) from Equation III.3, straight forward calculation yields the "potential integral",

$$|V| = 0.44 \pm 0.01\ eV$$

which agrees well with an estimate made[9] on more dilute PdCo alloys.

III.4.ii Spin-wave Stiffness, D

The T^2-coefficient from Equation I.23 is

$$\frac{3\pi m^* c}{2e^2\hbar N\varepsilon_F}\ \frac{\pi^2|J_{s\text{-local}}|^2 S}{12}\left(\frac{k_B}{Dk_F^2}\right)^2 \qquad \text{III.8}$$

The first factor has already been evaluated. The spin-wave stiffness constant D can be extracted from this if $|J_{s\text{-local}}|$, S, and k_F can be evaluated.

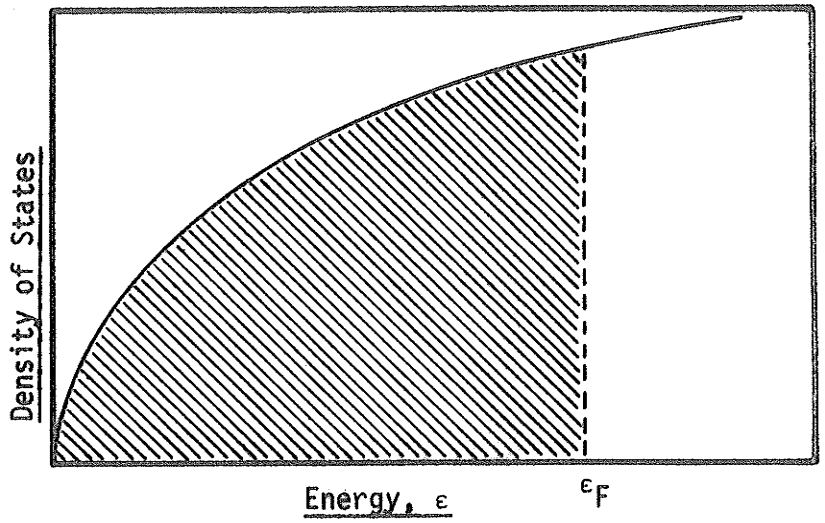

FIG. III-6. Density of single-particle states as a function of energy for a free electron gas in three dimensions. The shaded area represents the filled states at absolute zero.

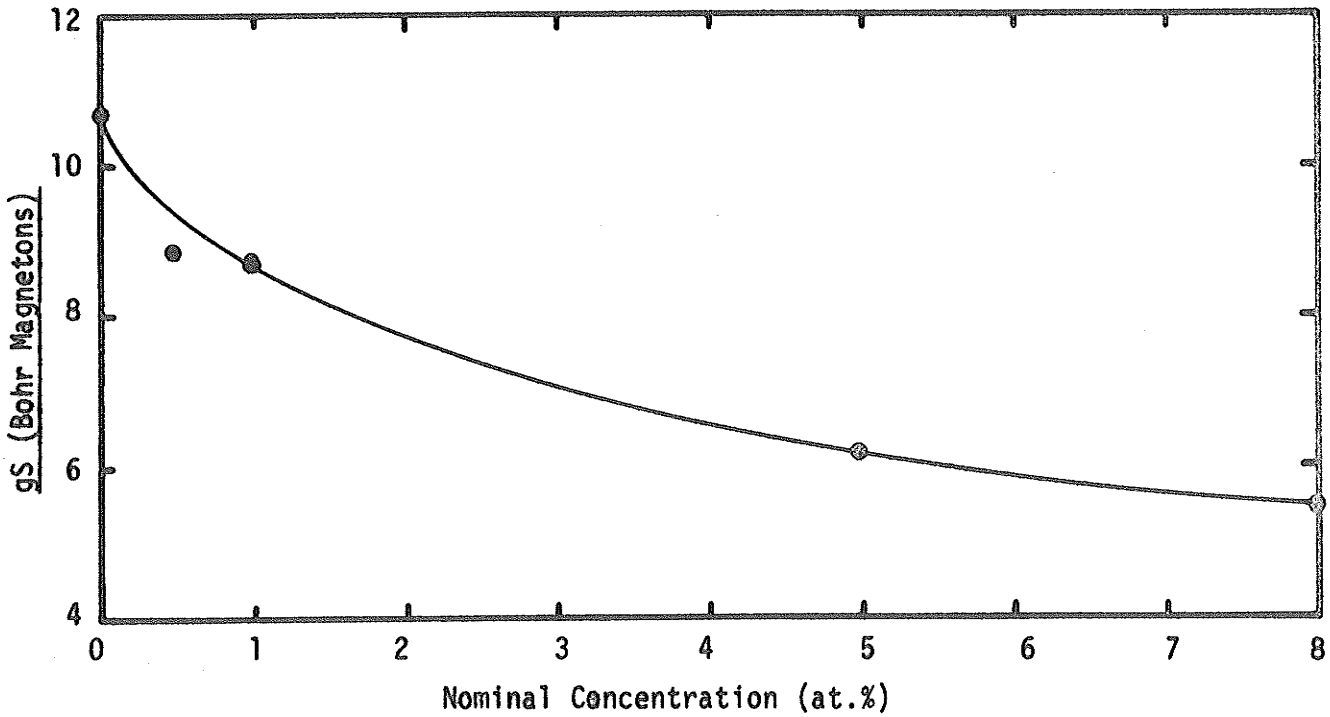

FIG. III-7. Moment associated with one cobalt atom for various Co concentrations. This data from Bozorth et al.[16].

III.4.iii Values of S

On the basis of the "s-d" model which has been adopted here, S is interpreted as the giant-moment-on-site-impurity spin plus the attendant host-d-band polariation. Saturation magnetization measurements[16] on PdCo in the concentration range 2 to 8 at. % Co provide values of gS (where g is the impurity splitting factor). Figure III-7 shows specifically the decrease in gS with concentration[16]. Using the value g = 2.4 obtained from ferromagnetic-resonance measurements[21] at 4.2K on PdCo of concentration comparable to those used in this study, values of S range from 3.3 to 2.3 for concentrations ranging from 2 to 8 at. % Co. Specific estimates are listed in Table III-3. This reduction in S for increased concentration is expected on the basis of increased giant-moment overlap and consequent reduction in d-band polarization per impurity.

III.4.iv Estimates of $|J_{s\text{-}local}|$

Estimates of $|J_{s\text{-}local}|$ are obtained by employing a molecular field model[22] modified for the case of ferromagnetic ordering[12]. Complete spin order is assumed to exist at T = 0, and complete disorder at $T = T_c$, then (modifying equation 19, reference 22)

$$|J_{s\text{-}local}|^2 = \frac{2(2S+1)\Delta\rho(T_c) - \Delta\rho(T=0) \pm [8S(2S+1)\Delta\rho(T_c)\Delta\rho(T=0) + \Delta\rho(T=0)^2]^{1/2}}{2 \times 6.49c'S(2S+1)^2} \qquad \text{III.9}$$

where $\Delta\rho(T = 0)$ and $\Delta\rho(T_c)$ are the incremental resistivities at zero and the Curie temperatures, respectively, and the origin of the factor 6.49c' has already been discussed. $|J_{s\text{-}local}|$ is, in fact, wave-vector (q) dependent[23,24], and the value obtained in the above equation is a properly weighted average. Since no realistic estimates of the q-dependence are currently extant, it seems reasonable to suppress it here and to equate $|J_{s\text{-}local}|$ in Equations III.8 and III.9.

Values of $\Delta\rho(T=0)$ are readily obtainable from the current data, but not for the $\Delta\rho(T_c)$. These are extracted from the data of Schwaller and Wucher[14], where T_c is taken as the temperature at which a marked change in slope appears. From Figure III-8 it is seen that $\Delta\rho(T_c)$ is nearly linear with concentration having a value $\approx$ 1.8 μΩcm./at.% Co. This value agrees well with PdCo alloys with <1 at.% Co[9]. Combining these estimates of $\Delta\rho(T_c)$ with previous estimates of S yield values for $\left|J_{s\text{-}local}\right|$. These are listed in Table III-3.

III.4.v Magnitude of k_F

Once again applying the effective mass treatment of the s-band, and recalling that in this approximation

$$\varepsilon_F = \frac{\hbar^2 k_F^2}{2m^*}$$

the value $k_F = 0.89\ \text{Å}^{-1}$ is readily deduced. This, together with the estimates obtained for S and $\left|J_{s\text{-}local}\right|$, and the T^2-coefficients (Table III-2) permit evaluation of the spin-wave stiffness constant D. Combining Equations III.8 and III.9 gives

$$T^2\text{-coef.} = \frac{\pi^2}{24}\left(\frac{k_B}{Dk_F^2}\right)^2 \frac{2(2S+1)\Delta\rho(T_c)-\Delta\rho(T=0)\pm[8S(2S+1)\Delta\rho(T_c)\Delta\rho(T=0)+\Delta\rho(T=0)^2]^{1/2}}{2S+1} \qquad \text{III.10}$$

Note here that D depends only upon k_F and S. The results of this and the previous calculations are summarized in Table III-3.

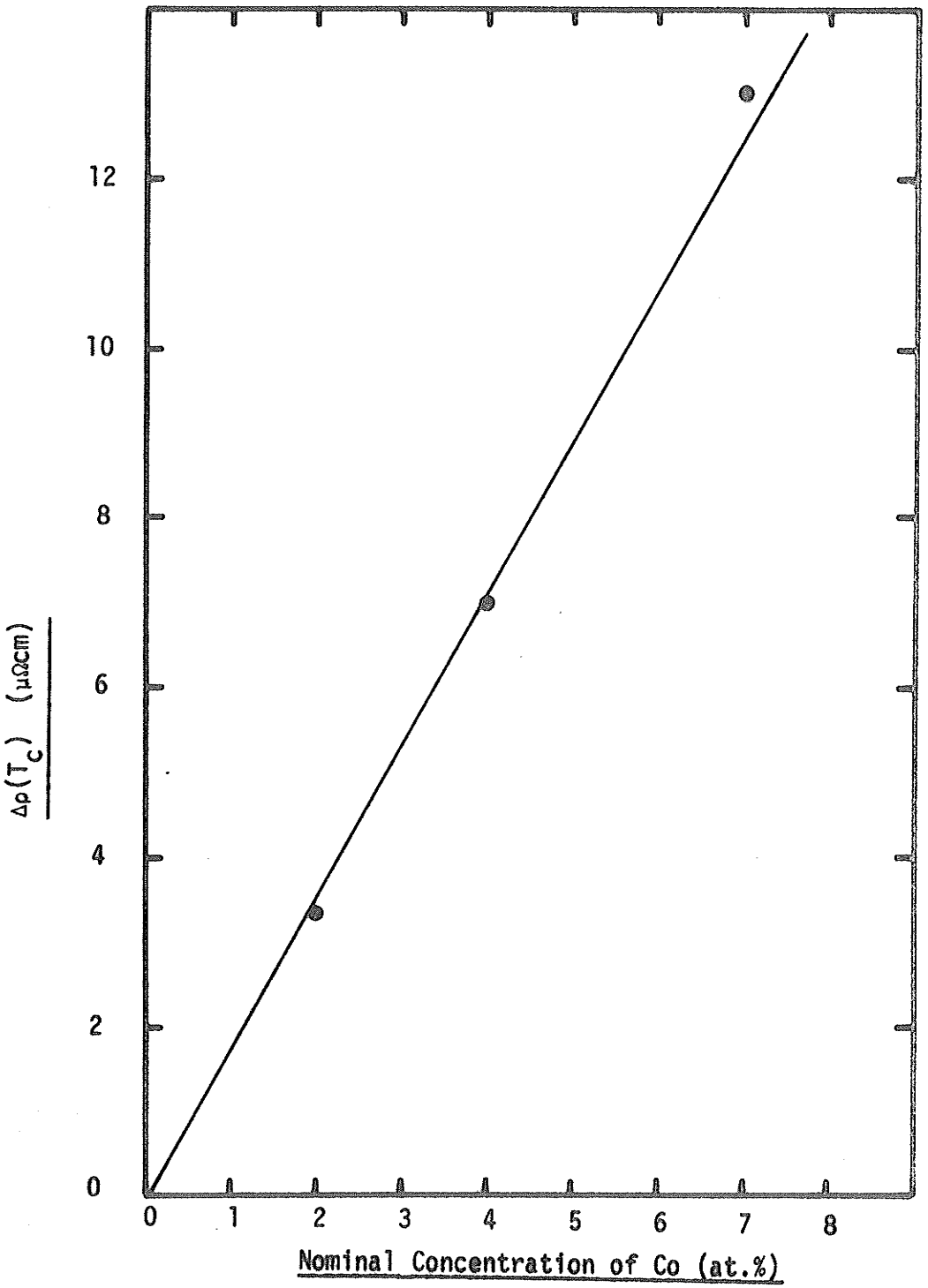

FIG. III-8. Graph of incremental resistivity (in μΩcm) at the Curie temperature plotted against the nominal concentration of Co impurity (in at.%). Data extracted from Reference 14. The line drawn has a slope of 1.8 μΩcm/at.% Co.

TABLE III-3

Estimates of S, $|J_{s\text{-}local}|$, and D

Co Concentration (at.%)	Values of S	$\|J_{s\text{-}local}\|$ (eV)	$\|J\|^2S(k_B/Dk_F^2)^2$ ($10^{-5}\mu\Omega cm/K^2eV^2$)	D ($K\AA^2$)
2	3.3	0.044	2.30±0.02	22.0±0.2
3	3.1	0.047	1.18±0.02	31.6±0.3
4	2.8	0.051	0.71±0.01	42.8±0.4
5	2.6	0.056	0.51±0.01	52.3±0.6
7.5	2.3	0.066	0.23±0.01	82.6±1.0

These values of D are in good agreement with those derived for the $T^{3/2}$-coefficient terms in $\Delta\rho(T)$ for more dilute PdCo alloys[25].

III.4.vi Concentration Dependence of D

In Figure III.9 the spin-wave stiffness constant D is plotted against nominal concentration (on a log-log scale) to determine the concentration dependence of D. It illustrates the functional form to be

$$D = D_o c^n$$

where n = 1.00±0.05 and D_o = 10.7±0.5 $K\AA^2$/at.% Co for 2 < c < 7.5 at.% Co. The variation in D is significantly less rapid than that observed for alloys with <1 at.% Co where n was about 3/2[25]. This trend seems entirely reasonable considering the strong overlap of the polarization clouds of several giant moments and an increasing degree of magnetic "homogeniety".

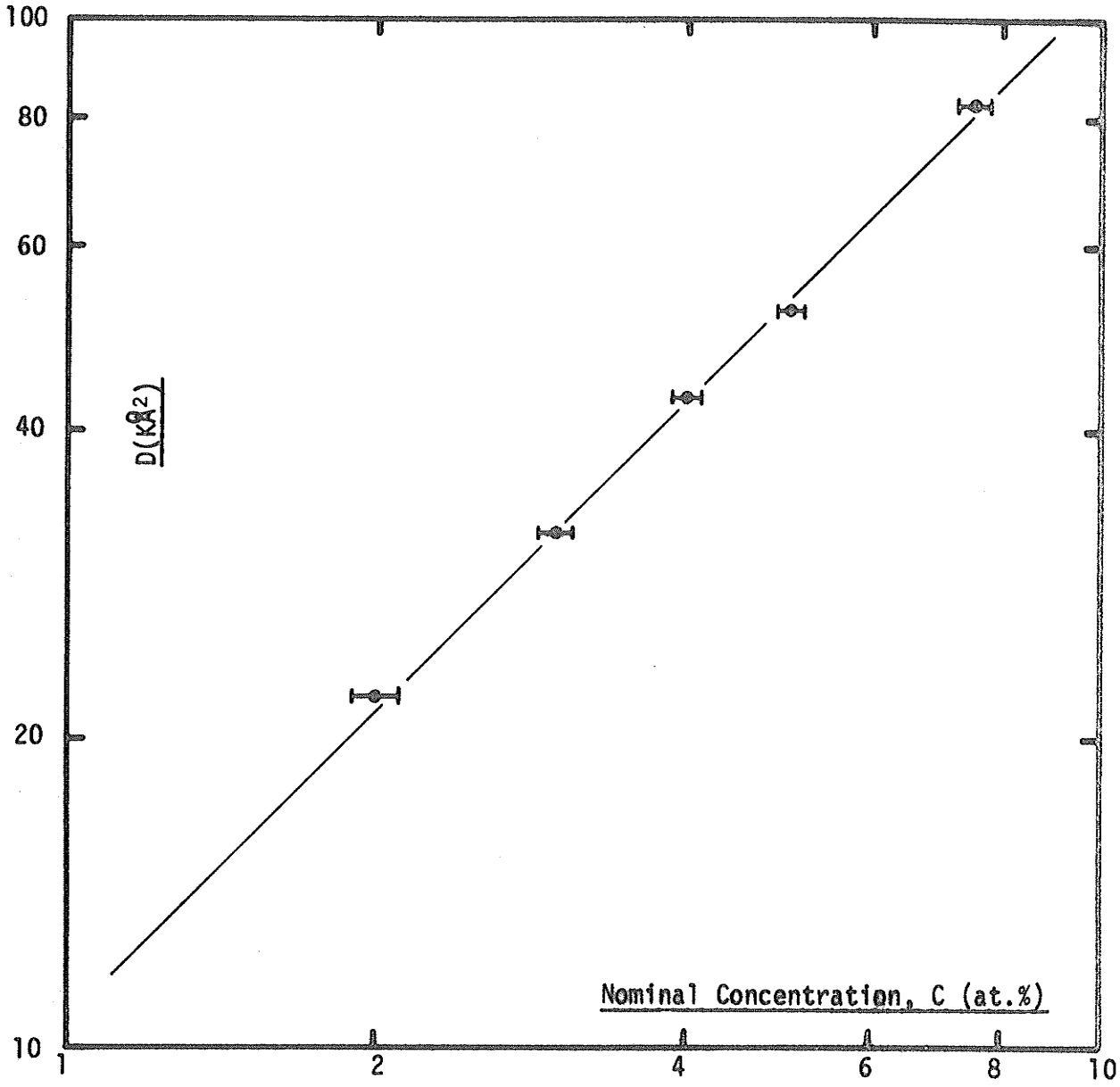

FIG. III-9. The acoustic spin-wave stiffness D (in KÅ²) listed in Table III-3, plotted against the nominal impurity concentration (in at.%), on a logarithmic scale. The line drawn has a slope of 1.00.

III.5 Summary

Electrical resistivity measurements made on PdCo alloys with impurity concentrations between 2 and 7.5 atomic percent Co indicate that for temperatures well below the Curie temperature, the incremental resistivity, $\Delta\rho(T) = \rho_{alloy}(T) - \rho_{metal}(T)$, can be closely described by the expression

$$\Delta\rho(T) = Ac + BT^2$$

where A = 1.27±0.03 μΩcm./at.% Co. The factor B is concentration dependent having the form

$$B = B_o c^n$$

with n = -0.75±0.05 and $B_o \approx 4.1 \times 10^{-4}$ μΩcm./K^2. Based on a wave-vector conserving "s-d" model, an expression for the incremental resistivity was derived. For $T \ll T_c$, the model predicts that the incremental resistivity will be the sum of a temperature independent term and a term varying as the square of the temperature, exactly what was experimentally observed. From the first term, the value obtained for the "potential scattering integral" was

$$|V| = 0.44 \pm 0.01 \text{ eV}.$$

The coefficient of the T^2 term, which depends upon S, $|J_{s\text{-}local}|$, and k_F, permitted computation of values for the spin-wave stiffness constant D. For the concentration range 2<c<7.5 at.% Co, D was found to obey

$$D = D_o c^n$$

where n = 1.00±0.05 and D_o = 10.7±0.5 $K\text{Å}^2$/at.%. This variation in D being considerably less rapid than that found for alloys with less than 1 at.% Co suggests the existence of increased magnetic homogeniety.

References

1. B. W. Veal and J. A. Rayne, Phys. Rev. 135, 442 (1964).

2. J. C. G. Wheeler, J. Phys. C2, 135 (1969).

3. T. F. Smith, W. E. Gardner, and H. Montgomery, J. Phys. C. Suppl. 3, S370 (1970).

4. T. F. Smith, W. E. Gardner, and J. I. Budnick, Phys. Letters 27A, 326 (1968).

5. S. Doniach and E. P. Wohlfarth, Proc. Roy. Soc. (London) 295A, 442 (1967).

6. H. S. D. Cole and R. E. Turner, J. Phys. C2, 124 (1969).

7. P. D. Long and R. E. Turner, J. Phys. C Suppl. 3, S127 (1970).

8. Gwyn Williams and J. W. Loram, J. Phys. Chem. Solids 30, 1827 (1969).

9. Gwyn Williams, J. Phys. Chem. Solids 31, 529 (1970).

10. Gwyn Williams and J. W. Loram, Solid State Commun. 7, 1261 (1969).

11. G. J. Nieuwenhuys and B. M. Boerstol, Phys. Letters 33A, 281 (1970).

12. M. E. Colp and Gwyn Williams, Phys. Rev. B5, 2599 (1972).

13. S. Skalski, M. P. Kawatra, J. A. Mydosh, and J. I. Budnick, Phys. Rev. B2, 3613 (1970).

14. R. Schwaller and J. Wucher, Compt. Rend. B264, 1007 (1967).

15. J. W. Loram, T. E. Whall, and P. J. Ford, Phys. Rev. B2, 857 (1970).

16. R. M. Bozorth, P. A. Wolff, D. D. Davis, V. B. Compton, and J. H. Wernick, Phys. Rev. 122, 1157 (1961).

17. W. B. Pearson, "Handbook of Lattice Spacings and Structures of Metals", Pergamon Press, New York (1958).

18. A. D. C. Grassie, G. A. Swallow, Gwyn Williams and J. W. Loram, Phys. Rev. B3, 4154 (1971).

19. J. J. Vuillemin, Phys. Rev. 144, 396 (1966).

20. J. J. Vuillemin and M. G. Priestley, Phys. Rev. Letters 14, 307 (1965).

21. D. N. S. Bagguley, W. A. Crossley and J. Liesegang, Proc. Roy. Soc. (London) 90, 1047 (1967).

22. K. Yosida, Phys. Rev. 107, 396 (1957).

23. R. E. Watson and A. J. Freeman, Phys. Rev. 152, 566 (1966).

24. M. Peter, J. Dupraz and H. Cottet, Helv. Phys. Acta 40, 301 (1967).

25. Gwyn Williams and J. W. Loram, J. Phys. F1, 434 (1971).

CHAPTER FOUR

RUTHENIUM MANGANESE

IV.1 Introduction

The present study examines the low temperature resistivity of some dilute RuMn alloys. Recently, Riblet and Jensen[1] studied the superconducting transition temperatures, T_c, for a number of ruthenium based alloys, and found that the rates of decrease of T_c with impurity concentration, dT_c/dc, for alloys of Ni, Rh, Pd, Ir and Pt were much less rapid than for the "magnetic" impurities Co and Fe[2]. Furthermore, these authors note that the rapid increase in superconducting transition temperature was explicable on the basis of d-level spin fluctuations localized within the impurity cell. The fact that Mn shows well-defined magnetic behaviour in PdMn[3] and AuMn[4], and localized-spin-fluctuation behaviour in RhMn[5] and AlMn[6], stimulated the present interest in dilute RuMn alloys.

Chromium, used as an impurity in dilute alloys, also shows well-defined magnetic behaviour in AuCr[7], and lsf effects in AlCr[6]. A study of several dilute RuCr alloys has been recently conducted by Kao and Williams[8] and has revealed a temperature independent incremental resistivity over the range 1.45 to 140K, apart from small deviations attributed to the breakdown of Matthiessen's Rule[11] due to the competing effects of phonon and potential scattering with presumably different anisotropies.

IV.2 Sample Preparation

Samples were prepared from 99.999% pure Ru sponge and 99.99% pure Mn flake, both obtained from Johnson Matthey and Co., London, U.K. The Ru sponge was pressed into metallic pellets using a $\frac{1}{4}$" I.D. hardened stainless steel die, and the pellets were melted together in an argon arc furnace. Since Ru forms an hcp structure with a low c/a ratio it is very

difficult to cold work. Severe fracturing occured when an attempt was made to cold roll it. As a result the Ru was cast into a long cylinder (∿5 cm. long, 15 grams) by melting the pellets in a cylindrical trough (about 7 mm diameter) which was milled into the water-cooled copper hearth of the arc furnace. A specimen of square cross-section with area about 2.5×10^{-3} cm^2 was cut from the cylinder with a diamond saw.

A 40 at.% Mn master alloy was prepared by melting together appropriate proportions of the pure elements. High weight losses were observed. Noting that the boiling point of Mn (2150K) is lower than the melting point of Ru (2500K), it seems reasonable to assume that the loss is due to evaporation of Mn, and additional pure Mn was added to the master. The final composition was confirmed by X-ray analysis.

An alloy of nominal value 0.2 at.% Mn was prepared from the Ru scraps left after cutting the pure Ru specimen and an appropriate amount of master alloy. The alloy was inverted and remelted several times to ensure homogeniety, and a specimen was cut from the cylindrical alloy with the diamond saw. By a similar procedure specimens of nominal concentrations 0.4 and 0.8 at.% Mn were prepared.

Even with argon pressures close to one atmosphere, weight losses were encountered during melting and homogenizing. Consequently, the samples were sent to D. Griffiths, London, U.K. for content analysis. The results of this analysis are presented in Table IV-1.

TABLE IV-1

Sample Analysis

Nominal Mn Concentration	Concentration Determined From Analysis
0.2 at.%	0.06 at.%
0.4 at.%	<10 ppm or "pure"
0.8 at.%	0.1 at.%

Owing to the hardness of ruthenium no impressions were left on the specimens by the knife-edge clamps, and consequently the procedure for determining the form factors (as discussed in Section III-3) had to be somewhat modified.

The average cross-sectional area of each sample was obtained from values of the length, weight and density. The length and weight were determined as described earlier, but in this case the density was computed using a buoyancy technique. Use of the "floating" knife-edge contacts required that the inter-knife-edge spacing be measured in situ on the sample mounting block. The travelling microscope was used for this measurement. The A/ℓ ratios were then calculated within an estimated error of ±1%.

IV.3 Data Collection

Data was collected in the manner outlined in Section III.3. In this case only four samples were used reducing the number of current measurements for each "point". Rather than revise the computor programmes (Appendix A), "dummy" current values were fed in for the two non-existent specimens.

IV.4 Results and Discussion

The difference $\{\rho(T) - \rho(1.45K)\}$ between the measured resistivity at temperature T and that at the lowest termperature attained, 1.45K, is plotted as a function of temperature up to 15K in Figure IV-1. Table IV-2, which lists the measured values of $\rho(1.45K)$ for all four specimens, illustrates a lack of systematic variation in $\rho(1.45K)$, and that Mn apparently contributes nothing to the residual resistivity of the alloy. Figure IV-1 (in which the resistivity difference is plotted because of the lack of systematic influence of Mn) shows that the resistivity exhibits no temperature dependence for either the pure Ru or for the alloys below 15K, even though a temperature dependent electron-electron scattering contribution is expected[9]. Using the estimates of Schriempf and MacInnis[10] an electron-electron contribution of about 8.5×10^{-4} μΩcm is expected over the temperature interval up to about 15K, which is below the limits of resolution for the present system and the existing form factors.

TABLE IV-2

Summary of Data on the RuMn Alloys

Alloy (at.% Mn)	$\rho(1.45K)$ (μΩcm)	$\rho(297K)$* (μΩcm)	Coefficient of T^2 Term (10^{-5} μΩcm/K^2)
Ru1	0.105±0.005	8.16±0.08	-
Ru2	0.065±0.005	7.99±0.08	-
0.06	0.115±0.005	8.40±0.08	0.70±0.1
0.1	0.095±0.005	8.50±0.08	0.95±0.1

*The errors in this column include the estimated ±1% error in the measured A/1 factor.

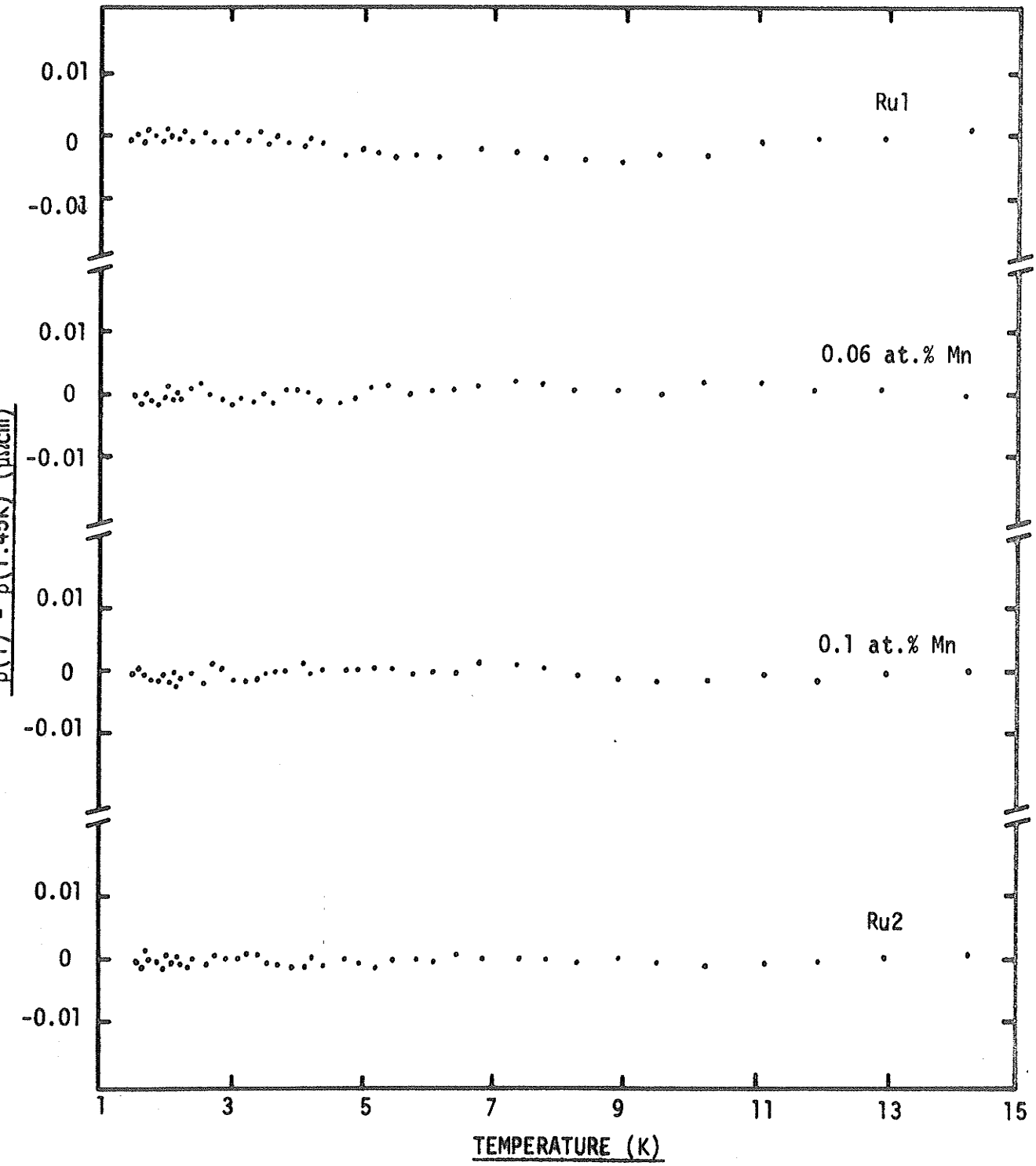

FIG. IV-1. The difference $\rho(T) - \rho(1.45K)$ plotted against temperature up to 15K for the four specimens.

The resistivity ratios, $\rho(297K)/\rho(1.45K)$, for the pure samples were 78 (Ru1) and 123(Ru2) which is about an order of magnitude smaller than that obtained for a Ru single crystal (1220) by Schriempf and MacInnis[10]. Since $\rho(297K)$ for the single crystal[10] is comparable to the values obtained in this study (Table IV-2), the low resistivity ratios observed are due to large values of $\rho(1.45K)$. These large values are not unreasonable considering the method of preparation of the samples (arc melting will not produce a single crystal), and the necessary lack of annealing.

In Figure IV-2 the difference $\rho(T) - \rho(1.45K)$ is again plotted against temperature, but this time in the range 30 to 130K. Close examination reveals that the difference increases more rapidly for the two RuMn alloys than it does for the two pure samples. The variations between the differences for the pure metal and the alloys are examined in greater detail in Figure IV-3. Recalling the theoretical discussion of Section I.10, and in particular Equations I.26 and I.27, $\rho_{imp}(T)$ was defined by $\rho_{alloy}(T) - \rho_{host}(T)$, with $\rho_{mag}(T) = \rho_{imp}(T) - \rho_{non\text{-}mag}$, and $\rho_{non\text{-}mag}$ is interpreted as the temperature independent residual resistivity, $\rho_{imp}(0)$. Due, however, to the considerably non-systematic variation in $\rho(1.45K)$, the analytical approach employed here was to first subtract the residual resistivity getting $\rho'(T) = \rho(T) - \rho(1.45K)$, and then to extract the anomolous resistivity

$$\rho_{mag}(T) = \rho'_{alloy}(T) - \rho'_{host}(T). \qquad \text{IV.1}$$

This $\rho_{mag}(T)$ is essentially the same as the theoretically deduced quantity, but with correction made for the experimentally observed inconsistency in residual resistivities. Figure IV-3 thus illustrates the temperature

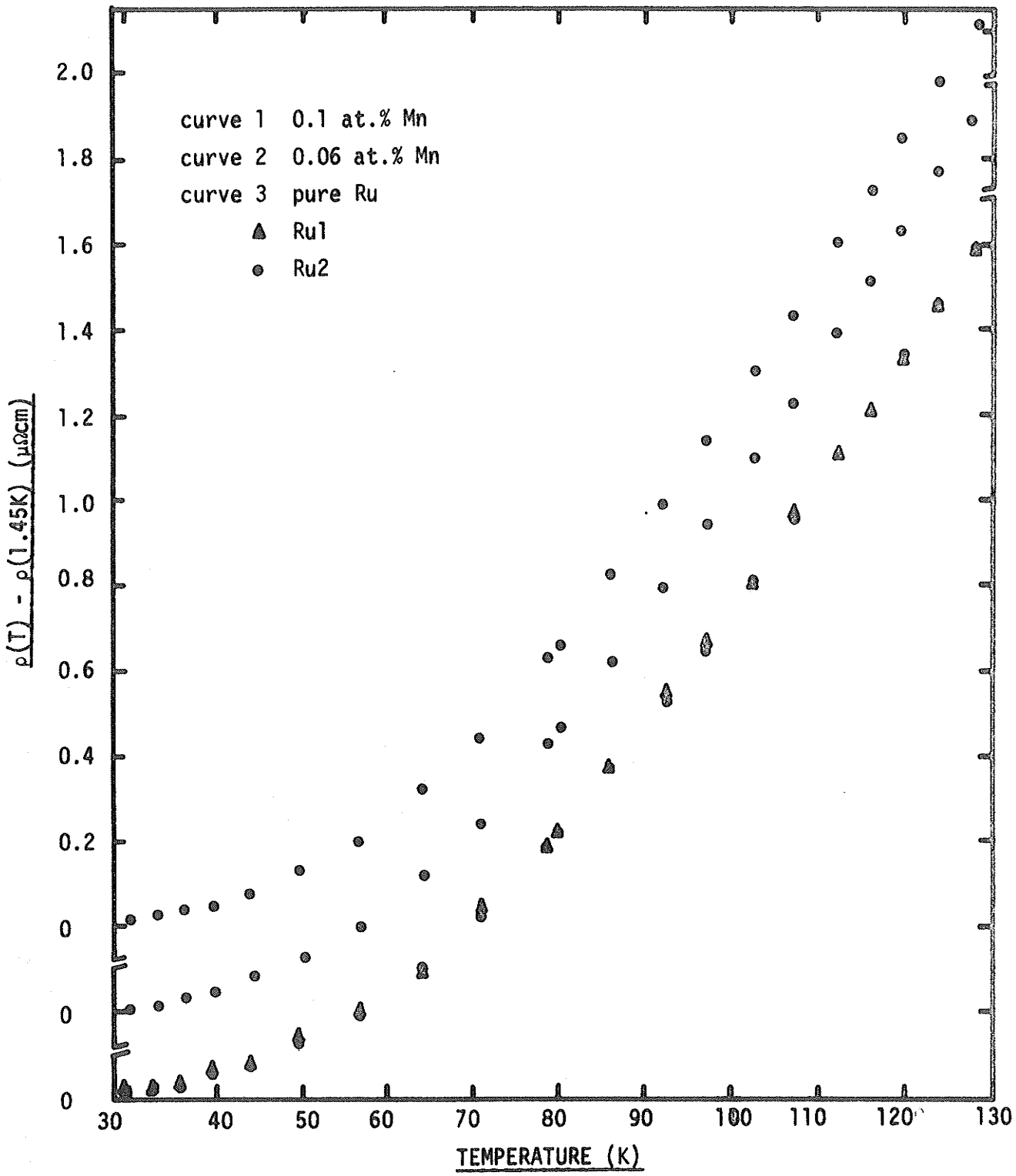

FIG. IV-2. The difference $\rho(T) - \rho(1.45K)$ plotted against temperature (in K) over the range 30 to 130K, for the four specimens. Note the change in zero.

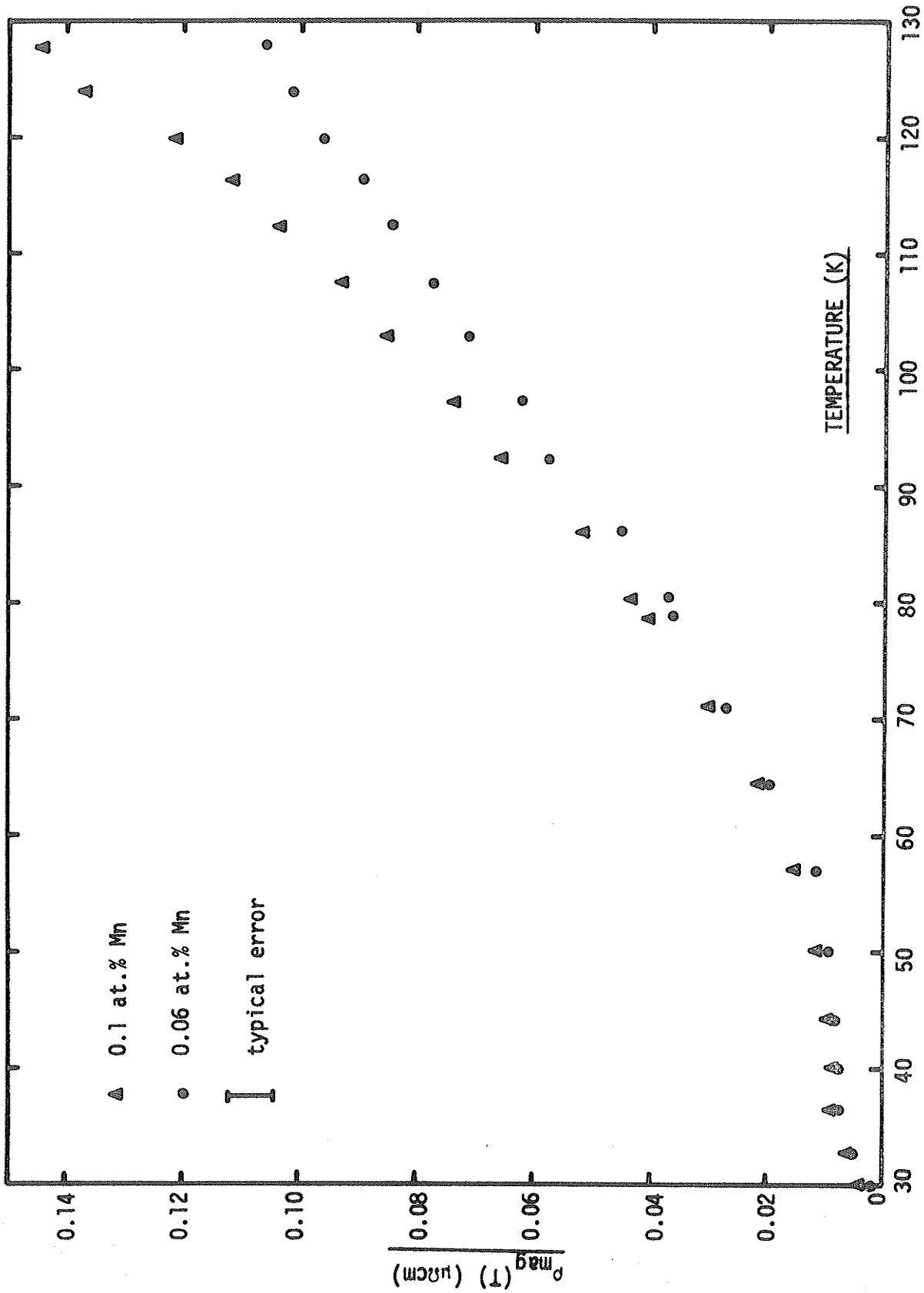

FIG. IV-3. $\rho_{mag}(T)$ (in μΩcm) plotted against temperature (in K) in the range 30 to 130K for Ru-0.06 at.% Mn and Ru-0.1 at.% Mn.

dependence of $\rho_{mag}(T)$ over the range 30 to 130K. The magnitude of $\rho_{mag}(T)$ is small $\{<0.05\ \rho'_{metal}(T)\}$, but it clearly rises faster than linear with T, and Figure IV-4 shows that the data can be represented by

$$\rho_{mag}(T) \propto T^2. \qquad \text{IV.2}$$

The uniqueness of 2 as the exponent in Equation IV.2 cannot be established due to the relative smallness of values of $\rho_{mag}(T)$. In fact, over the considered temperature range, it is found that,

$$\rho_{mag}(T) \propto T^n,\ 1.5 < n < 2.5. \qquad \text{IV.3}$$

The existence of a temperature dependent anomolous resistivity has been established, and attention is now given to finding a model which might explain the observed behaviour. The anomaly cannot be attributed to the breakdown of Matthiessen's Rule because of the continuous increase of $\rho_{mag}(T)$ with increasing temperature over the range where $\rho'_{metal}(T) < \rho(1.45K) << \rho'_{metal}(T)$. If breakdown did occur $\rho_{mag}(T)$ should become constant as suggested by Dugdale and Basinski[11] in the range of temperature where $\rho'_{metal}(T) < \rho_{mag}(T)$. An "s-d" model is rejected because of the weakness of the anomoly $\{\rho_{mag}(T) < 0.05\rho'(T)\}$. An explanation based on the non-conservation of crystal momentum is ruled out on the basis of the upper limit of the temperature exponent, $n<2.5$[12].

As suggested in the Introduction (Section IV.1) an explanation for the behaviour of $\rho_{mag}(T)$ might be sought on the basis of the lsf model. For s electron-lsf scattering, Kaiser and Doniach[13] predict a behaviour of the form

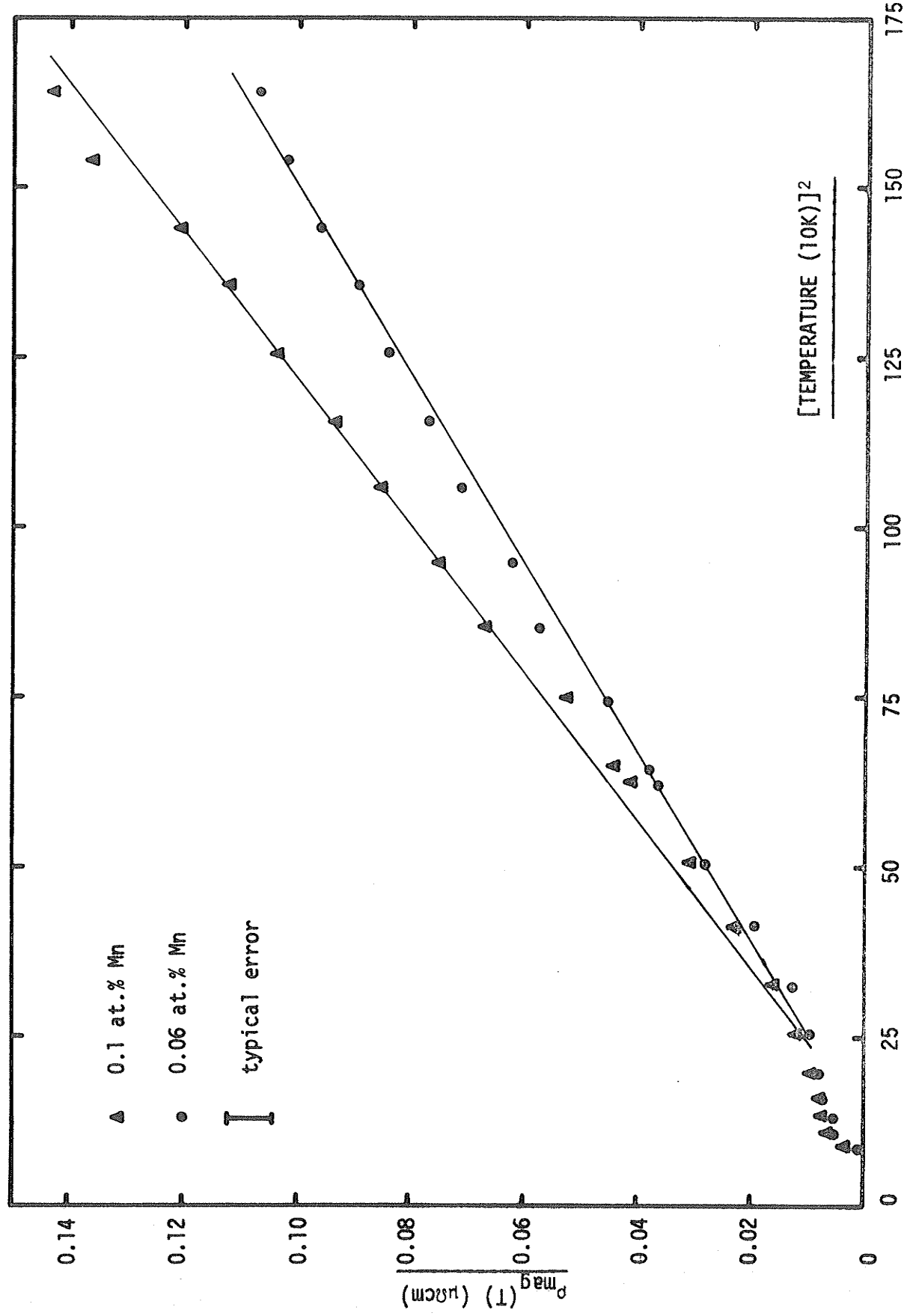

FIG. IV-4. $\rho_{mag}(T)$ in ($\mu\Omega$cm) plotted against the square of the temperature for Ru-0.06 at.% Mn and Ru-0.1 at.% Mn.

$$\rho_{mag}(T) \propto cT^2, \quad T < \frac{1}{4}T_s \qquad \text{IV.4}$$

where c is the concentration of the alloy. Within the experimental uncertainty, the T^2-coefficients are linear with concentration (refer to Figure IV-5), and the data is fairly well represented by a T^2 dependence in the temperature range up to 130K.

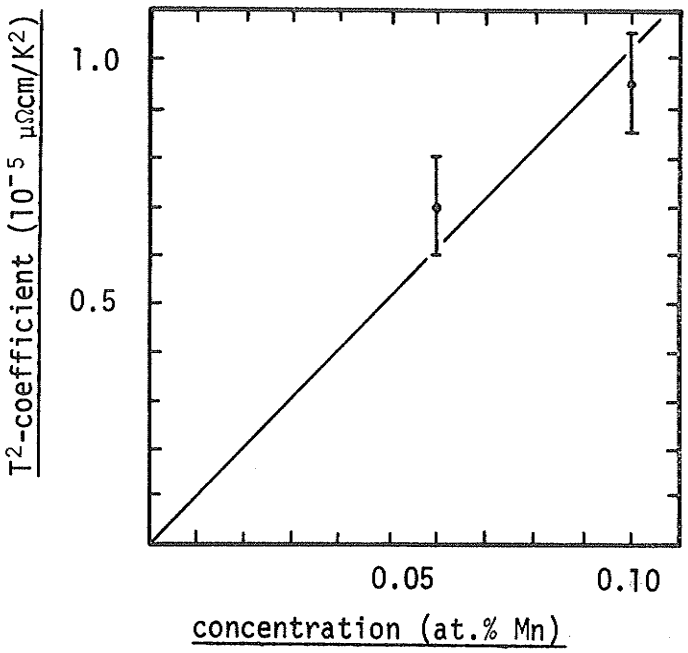

FIG. IV-5. Concentration dependence of T^2-coefficient of $\rho_{mag}(T)$

If this T^2 character continued to room temperature, then, using the coefficients in Table IV-2, the values of $\rho_{mag}(297K)$ for the two alloys would be 0.62 ± 0.09 and 0.85 ± 0.09 μΩcm, respectively. These values are approximately double the corresponding measured values (see Table IV-3), suggesting a flattening out of the temperature dependence. The lsf model (recall Equation I.25 and Figure I-12) predicts a transition from T^2 to T dependence for $T > 0.6T_s$. Assuming this model to be valid, then, the transition must occur between 130 and 300K, and the characteristic temperature T_s can be estimated to be between 500 and 1000K.

TABLE IV-3

Estimates of $\rho_{mag}(297K)$

Alloy (at.% Mn)	$\rho'(297K)$ ($\mu\Omega$cm)	$\rho_{mag}(297K)$, experimental ($\mu\Omega$cm)	$\rho_{mag}(297K)$, predicted from T^2-coefficient ($\mu\Omega$cm)
Ru1	8.05	-	-
Ru2	7.92	-	-
0.06	8.28	0.23 to 0.36	0.62 ± 0.09
0.1	8.40	0.35 to 0.48	0.85 ± 0.09

IV.5 Summary

Electrical resistivity measurements were made on two dilute RuMn alloys in the temperature range 1.45K to 130K. The resistivity was observed to be independent of temperature up to about 30K within the resolution of the present system. Above this temperature a weak anomolous resistivity was found which can be represented by

$$\rho_{mag}(T) \propto cT^2.$$

The resistivity behaviour over the range 1.45K to 130K and at room temperature can be reasonably well explained on the basis of the Kaiser-Doniach s electron-lsf scattering model with $T_s \sim$ 500K to 1000K.

References

1. G. Riblet and M. A. Jensen, Physica 55, 622 (1971).

2. K. Andres, E. Bucher, J. P. Maita and R. C. Sherwood, Phys. Rev. 178, 702 (1969).

3. Gwyn Williams and J. W. Loram, J. Phys. F 1, 434 (1971).

4. M. D. Daybell and W. A. Steyert, Rev. Mod. Phys. 40, 380 (1968).

5. B. R. Coles, S. Mozumder and R. Rusby, "Proceedings of the 12th International Conference on Low Temperature Physics", Editor: E. Kanda (Tokoyo; Keigako Publishing Co.), 737 (1970).

6. A. D. Caplin and C. Rizzuto, Phys. Rev. Letters 21, 746 (1968).

7. A. J. Heeger, Solid State Physics, Volume 23, Edited by Frederick Seitz, David Turnbull and Henry Ehrenreich, Academic Press, New York, 283 (1969).

8. M. E. Colp, F. C. C. Kao and Gwyn Williams, to be published.

9. M. J. Rice, Phys. Rev. Letters 20, 1439 (1968).

10. J. T. Schriempf and W. M. MacInnis, Phys. Letters 33A, 511 (1970).

11. J. S. Dugdale and Z. S. Basinski, Phys. Rev. 157, 552 (1967).

12. I. A. Campbell, A. D. Caplin, and C. Rizzuto, Phys. Rev. Letters 26, 239 (1971).

13. A. B. Kaiser and S. Doniach, Intern. J. Magnetism, 1, 11(1970).

APPENDIX

```
      C  APPENDIX A.1
      C
      C
      C  DILUTE ALLOY CALCULATIONS FOR TEMPERATURES ABOVE 4.2K.
      C
      C
 1          REAL  RMETAL(100),RIMP(100,5),RINC(100,5),RCONC(100,5),TEMP(100)
 2          REAL  FORM(5),CONC(5),VOLTS(6),AMPS(12),A(5)
 3          INTEGER  IPT(100)
      C
 4          READ, PO,TO,TR
      C
      C  PO  IS THE FILLING PRESSURE.
      C  TO  IS THE FILLING TEMPERATURE.
      C  TR  IS THE ROOM TEMPERATURE.
      C
 5          READ,(CONC(I),I=1,5)
 6          READ,FORMM,(FORM(I),I=1,5)
      C
      C  CONC(I)  ARE THE CONCENTRATIONS OF THE ALLOYS IN ATOMIC PERCENT.
      C  FORM'S  ARE FORM FACTORS FOR THE HOST AND THE FIVE ALLOYS.
      C
 7          READ,NPTS
      C
 8          DO 1  I=1,NPTS
 9          READ,VOLTS(1),VOLTS(2),(AMPS(L),L=1,6),VOLTS(3),VOLTS(4),
            1(AMPS(L),L=7,12),VOLTS(5),VOLTS(6),P,IPT(I)
10          TEMP(I)=THERM(P,PO,TO,TR)
11          V1=(VOLTS(1)+VOLTS(2)+VOLTS(3)+VOLTS(4))/4.0
12          V2=(VOLTS(3)+VOLTS(4)+VOLTS(5)+VOLTS(6))/4.0
13          AMP=(AMPS(1)+AMPS(2))/(2.0*0.9398)
      C
      C  0.9398  CORRECTS FOR THE ERROR IN THE "10 OHM" STANDARD RESISTOR.
      C
14          DO 2  K=1,5
15          J=2*K + 1
16    2     A(K)=(AMPS(J) + AMPS(J+1))/(2.0*0.9398)
      C
17          RMETAL(I)=FORMM*V1/AMP
18          DO 3  K=1,2
19    3     RIMP(I,K)=FORM(K)*V1/A(K)
20          DO 4  K=3,5
21    4     RIMP(I,K)=FORM(K)*V2/A(K)
22          DO 5  K=1,5
23          RINC(I,K)=RIMP(I,K) - RMETAL(I)
24          IF(FORM(K).EQ.0.0) RINC(I,K)=0.0
25    5     RCONC(I,K)=RINC(I,K)/CONC(K)
26    1     CONTINUE
      C
      C  PROCEED TO OUTPUT DATA.
      C
27          PRINT 100,PO,TO,TR
28    100   FORMAT('-','INITIAL CONDITIONS: FILLING PRESSURE ',F9.2,/,21X,
           1'FILLING TEMPERATURE',F7.2,/,21X,'ROOM TEMPERATURE',F10.2,//)
```

```
29          PRINT 101,(CONC(I),I=1,5)
30    101   FORMAT('0','THE CONCENTRATIONS IN ATOMIC PERCENT ARE: '5F6.2,//)
      C
31          PRINT 102,FORMM
32    102   FORMAT('0','FORM FACTORS ARE: FORM  = ',E14.7)
33          DO 10  L=1,5
34    10    PRINT 103,L,FORM(L)
35    103   FORMAT(' ',18X,'FORM',I1,' = ',E14.7)
      C
36          PRINT 104
37    104   FORMAT('1','***TEMPERATURE DEPENDENT SPECIMEN RESISTIVITIES***',/)
38          PRINT 105
39    105   FORMAT('0','POINT NUMBER',8X,'RMETAL',10X,'RIMP1',11X,'RIMP2',11X,
           1'RIMP3',11X,'RIMP4',11X,'RIMP5',10X,'TEMPERATURE',//)
40          PRINT 106,(IPT(I),RMETAL(I),(RIMP(I,J),J=1,5),TEMP(I),I=1,NPTS)
41    106   FORMAT((5X,I3,7X,6(2X,E14.7),F13.2))
      C
42          PRINT 200
43    200   FORMAT('1','***INCREMENTAL RESISTIVITIES OF THE ALLOYS***',//)
44          PRINT 201
45    201   FORMAT(' ','POINT NUMBER',8X,'RINC1',11X,'RINC2',11X,'RINC3',11X,
           1'RINC4',11X,'RINC5',10X,'TEMPERATURE',//)
46          PRINT 202,(IPT(I),(RINC(I,J),J=1,5),TEMP(I),I=1,NPTS)
47    202   FORMAT((5X,I3,7X,5(2X,E14.7),F13.2))
      C
48          PRINT 300
49    300   FORMAT('1','***RCONC=RINC/CONC, AND POWERS OF TEMPERATURE***',//)
50          PRINT 301
51    301   FORMAT(' ','PT.',6X,'RCONC1',10X,'RCONC2',10X,'RCONC3',10X,
           1'RCONC4',10X,'RCONC5',10X,'TEMP',5X,'TEMPSQ',5X,'TLOG',5X,
           2'T**3/2',//)
52          PRINT 302,(IPT(I),(RCONC(I,J),J=1,5),TEMP(I),TEMP(I)**2,
           1ALOG(TEMP(I)),SQRT(TEMP(I)**3),I=1,NPTS)
53    302   FORMAT((' ',I3,5(2X,E14.7),2(F9.2,F11.2)))
54          STOP;END
      C
      C
      C


56          FUNCTION THERM(P,PO,TO,TR)
      C
      C   THIS FUNCTION CONVERTS GAS THERMOMETER PRESSURES READ DIRECTLY FROM
      C   THE W&T GAUGE (IN INCHES OF WATER) TO EQUIVALENT TEMPERATURES.
      C
57          REAL  T(23),C(23)
58          DATA      T/2.6,3.0,3.5,4.0,4.5,5.,14.,16.,18.,20.,22.,30.,40.,50.,
           160.,70.,80.,90.,100.,125.,275.,300.,325./
59          DATA      C /-.0053,-.00487,-.00419,-.00361,-.00314,-.00277,
           1-.000549,-.000395,-.000276,-.00018,-.000101,.00018,.000251,.000338
           2,.000395,.000435,.000462,.00048,.000492,.000505,.000501,.000496,
           3.00049/
      C
      C   T   IS A SET OF TEMPERATURES.
      C   C   IS THE CORRESPONDING SET OF VIRIAL COEFFICIENTS.
```

```
60          DATA VB,VL1,VL,A,B/1.48,1.18,.0129,.00115,.000003/
      C
      C   VB    IS THE GAS THERMOMETER BULB VOLUME AT ROOM TEMPERATURE.
      C   VL1   IS THE ROOM TEMPERATURE TUBE VOLUME.
      C   VL    IS THE CRYOSTAT TUBE VOLUME.
      C   A     IS THE W&T GAUGE VOLUME PARAMETER.
      C   B     IS THE GAS BULB VOLUME EXPANSION COEFFICIENT.
      C
61          VL2=(TR*VL*ALOG(TR/TO))/(TR-TO)
      C
      C   VL2   IS THE EFFECTIVE ROOM TEMPERATURE CRYOSTAT TUBE VOLUME.
      C
62          AA=PO/(P*TO)
63          AB=(PO-P)*(VL1+VL2+A*(PO+P))/(P*VB*TR)
64          T1=1.0/(AA+AB)
      C
      C   T1   IS A FIRST ESTIMATE OF THE TEMPERATURE.
      C
65          VB1=VB*(1.0 + B*(T1-TO))
      C
      C   VB1   CORRECTS FOR THE EXPANSION OF THE GAS THERMOMETER BULB.
      C
66          AC=PO/(P*TO*(1.0 + B*(T1-TO)))
67          AD=AB/(1.0 + B*(T1-TO))
68          T2=1.0/(AC+AD)
      C
      C   T2 IS THE FIRST CORRECTED TEMPERATURE.
      C   NOW CORRECTION FOR THE NON-IDEAL NATURE OF THE GAS IS MADE.
      C
69          IF(T2.GT.2.6) GO TO 1111
70          VIR=C(1)
71          GO TO 1113
72    1111  DO 1  I=2,23
73          IF(T2.GT.T(I)) GO TO 1
74          VIR=C(I)-(T(I)-T2)*(C(I)-C(I-1))/(T(I)-T(I-1))
      C
      C   VIR   IS AN ESTIMATE OF THE SECOND VIRIAL COEFFICIENT.
      C
75          GO TO 1113
76    1     CONTINUE
77    1113  AK=0.1865*T2*PO*(-0.00314-VIR)/(TO*0.28)
      C
      C   0.1865   CONVERTS INCHES OF WATER TO CMS. OF MERCURY.
      C
78          THERM=T2+AK
79          RETURN;END
```

```
      C  APPENDIX A.2
      C
      C
      C  DILUTE ALLOY CALCULATIONS FOR TEMPERATURES BELOW 4.2K.
      C
      C
 1          REAL  RMETAL(100),RIMP(100,5),RINC(100,5),RCONC(100,5),TEMP(100)
 2          REAL  FORM(5),CONC(5),VOLTS(6),AMPS(12),A(5)
 3          INTEGER  IPT(100)
      C
 4          READ,(CONC(I),I=1,5)
 5          READ,FORMM,(FORM(I),I=1,5)
      C
      C  CONC(I)  ARE THE CONCENTRATIONS OF THE ALLOYS IN ATOMIC PERCENT.
      C  FORM'S  ARE FORM FACTORS FOR THE HOST AND THE FIVE ALLOYS.
      C
 6          READ,NPTS
      C
 7          DO 1  I=1,NPTS
 8          READ,VOLTS(1),VOLTS(2),(AMPS(L),L=1,6),VOLTS(3),VOLTS(4),
           1(AMPS(L),L=7,12),VOLTS(5),VOLTS(6),P,IPT(I)
 9          TEMP(I)=TEMCON(P)
10          V1=(VOLTS(1)+VOLTS(2)+VOLTS(3)+VOLTS(4))/4.0
11          V2=(VOLTS(3)+VOLTS(4)+VOLTS(5)+VOLTS(6))/4.0
12          AMP=(AMPS(1)+AMPS(2))/(2.0*0.9398)
      C
      C  0.9398  CORRECTS FOR THE ERROR IN THE "10 OHM" STANDARD RESISTOR.
      C
13          DO 2  K=1,5
14          J=2*K + 1
15     2    A(K)=(AMPS(J) + AMPS(J+1))/(2.0*0.9398)
      C
16          RMETAL(I)=FORMM*V1/AMP
17          DO 3  K=1,2
18     3    RIMP(I,K)=FORM(K)*V1/A(K)
19          DO 4  K=3,5
20     4    RIMP(I,K)=FORM(K)*V2/A(K)
21          DO 5  K=1,5
22          RINC(I,K)=RIMP(I,K) - RMETAL(I)
23          IF(FORM(K).EQ.0.0) RINC(I,K)=0.0
24     5    RCONC(I,K)=RINC(I,K)/CONC(K)
25     1    CONTINUE
```

```
      C  PROCEED TO OUTPUT DATA.
      C
26          PRINT 101,(CONC(I),I=1,5)
27    101   FORMAT('0','THE CONCENTRATIONS IN ATOMIC PERCENT ARE: '5F6.2,//)
      C
28          PRINT 102,FORMM
29    102   FORMAT('0','FORM FACTORS ARE: FORM  = ',E14.7)
30          DO 10  L=1,5
31    10    PRINT 103,L,FORM(L)
32    103   FORMAT(' ',18X,'FORM',I1,' = ',E14.7)
      C
33          PRINT 104
34    104   FORMAT('1','***TEMPERATURE DEPENDENT SPECIMEN RESISTIVITIES***',/)
35          PRINT 105
36    105   FORMAT('0','POINT NUMBER',8X,'RMETAL',10X,'RIMP1',11X,'RIMP2',11X,
           1'RIMP3',11X,'RIMP4',11X,'RIMP5',10X,'TEMPERATURE',//)
37          PRINT 106,(IPT(I),RMETAL(I),(RIMP(I,J),J=1,5),TEMP(I),I=1,NPTS)
38    106   FORMAT((5X,I3,7X,6(2X,E14.7),F13.2))
      C
39          PRINT 200
40    200   FORMAT('1','***INCREMENTAL RESISTIVITIES OF THE ALLOYS***',//)
41          PRINT 201
42    201   FORMAT(' ','POINT NUMBER',8X,'RINC1',11X,'RINC2',11X,'RINC3',11X,
           1'RINC4',11X,'RINC5',10X,'TEMPERATURE',//)
43          PRINT 202,(IPT(I),(RINC(I,J),J=1,5),TEMP(I),I=1,NPTS)
44    202   FORMAT((5X,I3,7X,5(2X,E14.7),F13.2))
      C
45          PRINT 300
46    300   FORMAT('1','***RCONC=RINC/CONC, AND POWERS OF TEMPERATURE***',//)
47          PRINT 301
48    301   FORMAT(' ','PT.',6X,'RCONC1',10X,'RCONC2',10X,'RCONC3',10X,
           1'RCONC4',10X,'RCONC5',10X,'TEMP',5X,'TEMPSQ',5X,'TLOG',5X,
           2'T**3/2',//)
49          PRINT 302,(IPT(I),(RCONC(I,J),J=1,5),TEMP(I),TEMP(I)**2,
           1ALOG(TEMP(I)),SQRT(TEMP(I)**3),I=1,NPTS)
50    302   FORMAT((' ',I3,5(2X,E14.7),2(F9.2,F11.2)))
51          STOP;END
```

```
53          FUNCTION TEMCON(P)
      C
      C  THIS PROGRAMME CONVERTS HELIUM-4 VAPOUR PRESSURES, MEASURED IN CM HG,
      C  TO THE CORRESPONDING TEMPERATURE. COMPUTATION IS MADE BE LINEAR
      C  INTERPOLATION BETWEEN KNOWN FIXED POINTS EXTRACTED FROM
      C  "EXPERIMENTAL TECHNIQUES IN LOW TEMPERATURE PHYSICS" BY G.K. WHITE.
      C
54          REAL  VP(88),THE(88)
55          DATA VP/80.,78.,76.,74.,72.,70.,68.,66.,64.,62.,60.,58.,56.,54.,
           152.,50.,48.,46.,44.,42.,40.,38.,36.,34.,32.,30.,29.,28.,27.,26.,
           225.,24.,23.,22.,21.,20.,19.,18.,17.,16.,15.,14.,13.,12.,11.,10.,
           39.,8.,7.,6.,5.,4.5,4.,3.5,3.,2.5,2.,1.8,1.6,1.4,1.2,1.,.9,.8,.7,
           4.6,.5,.4,.35,.3,.25,.2,.15,.1,.09,.08,.07,.06,.05,.04,.03,.02,
           5.01,.008,.006,.004,.002,.001/
56          DATA THE/4.265,4.238,4.21,4.182,4.153,4.124,4.094,4.064,4.033,
           14.001,3.969,3.936,3.902,3.867,3.832,3.795,3.757,3.719,3.679,3.638,
           23.595,3.551,3.506,3.459,3.41,3.358,3.332,3.305,3.277,3.248,3.219,
           33.189,3.158,3.126,3.094,3.06,3.025,2.988,2.951,2.911,2.871,2.828,
           42.783,2.735,2.685,2.632,2.575,2.514,2.447,2.373,2.29,2.244,2.194,
           52.14,2.081,2.016,1.942,1.908,1.872,1.833,1.789,1.739,1.712,1.682,
           61.649,1.613,1.571,1.522,1.495,1.464,1.428,1.387,1.336,1.27,1.254,
           71.236,1.217,1.195,1.17,1.14,1.104,1.056,.982,.96,.933,.897,.841,
           8.791/
      C
      C  VP(I)  IS A SET OF HELIUM VAPOUR PRESSURES.
      C  THE(I) IS THE CORRESPONDING SET OF TEMPERATURES.
      C  P  IS THE MEASURED MANOMETER PRESSURE IN CM HG.
      C
57          DO 2  J=2,88
58    2     IF(P.GE.VP(J)) GO TO 1
59    1     TEMCON=THE(J)+(P-VP(J))*(THE(J-1)-THE(J))/(VP(J-1)-VP(J))
60          RETURN;END
```